MODELING AND PARAMETRIC ANALYSIS

OF

MICRO THERMAL ACTUATORS

Shijie Xu

A Thesis

in

the Department

of

Mechanical and Industrial Engineering

Presented in Partial Fulfillment of the Requirements

For the Degree of Master of Applied Science at

Concordia University

Montreal, Quebec, Canada

June 2005

Canada

ABSTRACT

The greatest promise of micro electro mechanical systems (MEMS) lies in the ability to produce mechanical motion on a small scale. Such devices typically run on low power and are fast, taking advantage of such micro scale phenomena as strong electrostatic forces and rapid thermal responses. MEMS-based sensors and actuators have been widely deployed and commercialized. MEMS technologies also have potential applications in optics, transportation aerospace, robotics, chemical analysis systems, biotechnologies, medical engineering and microscopy using scanned micro probes.

Microactuators are useful tools for microsystems development. They produce displacement and useful forces to move, grasp or fine tune components of the Microsystems. Thermal actuators are simple devices with good mechanical and dynamic performances. Since integration requires that the designs of the entire system be performed on the micro chip, a good understanding of the performance of the micro thermal actuators is required. Modeling of thermal actuator is a complex task that requires multi physics formulation.

In this thesis, a multi-physics analytical model that can accurately predict the performance of a typical U-shaped micro electro thermal actuator fabricated by MUMPs technology is developed and validated through FEM analysis. Further, experiments are carried out on a benchmark micro thermal actuator. On the basis of this model, the relations between geometries of the thermal actuators and their thermal and mechanical behaviors are calculated and mapped out by simulating them in different geometric conditions. A parametric study that evaluates the performance of the devices with respect to the design geometries is carried out. The results are useful for thermal actuator designers.

ACKNOWLEDGEMENTS

CONTENTS

CHAPTER 5   SIMULATION AND PARAMETRIC STUDY

CHAPTER 6 CONCLUSIONS

LIST OF TABLES

LIST OF FIGURES

xiii

LIST OF NOMENCLATURE

A_w ---------- whole surface area of the thermal actuator

C_p ---------- specific heat capacity of polysilicon

E ------------ Young's modulus

E_g --------- input energy rate

F ---------- the equivalent force generated at the tip

I ------------ the bending moment of inertia

K ------------ thermal conductivity of polysilicon

K_{air} -------- thermal conductivity of air

K_s --------- the stiffness of the thermal actuator

MUMPs --- the Multi-User MEMS Processes

Nu_{av} ------- average Nusselt number

Pr ---------- Prandtl number

Q_R --------- heat dissipation through radiation

Q_V --------- heat dissipation through convection

Re ---------- Reynolds number

R (T) ------- electrical resistance of the whole thermal actuator

T ------------ the kinetic energy

T_{av} --------- the average temperature of the whole thermal actuator

T_f ---------- mean temperature

T_{max} --------- the maximum temperature of the thermal actuator

$\overline{T}_c$ ----------- the average temperature of the cold arm

$\overline{T}_f$ ---------- the average temperature of the flexure

$\overline{T}_h$ ---------- the average temperature of the hot arm

$T(x)$ -------- temperature distribution of the thermal actuator

U ----------- the strain energy

W_e^* --------- virtual external complementary work

W_i^* --------- virtual internal complementary work

d ------------ the deflection at the tip

f_t ----------- the thermal frequency

f_n ---------- the natural frequency

h_{av} --------- heat-transfer coefficient

l ------------- general length along contour of the structure

v ------------ velocity of the air

r_s ----------- Electrical resistivity (at 300k)

$r(T)$ -------- electrical resistivity of polysilicon

α ----------- thermal expansion

ε ----------- emissivity

ρ ----------- density of polysilicon

σ ----------- Stefan-Boltzmann constant

υ ----------- kinematic viscosity of air

λ ----------- factor coefficient of the temperature distribution

σ_b -------- the bending stress

σ_t ----------- the axial stress

η ----------- mechanical efficiency

η_B ----------- efficiency of heat energy balance

η_R ----------- efficiency of heat dissipated from radiation

η_V ---------- efficiency of heat dissipated from convection

Δ ------------ the thermal expansion of a discrete element

Δt ----------- duration for one stroke

CHAPTER 1 INTRODUCTION AND LITERATURE REVIEW

1.1 Microsystems

As the global economy moves beyond the microelectronics age, we must compete aggressively in the microsystems era. Microsystems include the devices, systems and technologies in the micro to nano-scale range. Microsystems are pervasive in nature. They are changing the way we live.

Building on the fundamental capabilities of microelectronics, a range of microsystems technologies is making possible the manufacture of ever more complex systems—which are powerful, efficient, smaller and inexpensive.

Microsystems technologies include microelectronics, photonics, micro-electro-mechanical systems (MEMS), microfluidics, and embedded software. Combining a number of heterogeneous technologies into single functional units called *Microsystems* offers new ways to overcome current microelectronics limitations and cost constraints to achieve more powerful product features, reduce power requirements, and increase productivity. Taking advantage of the complexities of microsystems involves immense changes in scientific and technological challenges, involving new skills and ideas, diverse disciplines and cross disciplinary interactions.

Over the next 30 years, microsystems technologies will have at least as much impact on our world as microelectronics has had in the past 30 years [1]. Further, the full exploitation of emerging nanotechnologies will depend on the availability of highly developed microsystem technologies. These technologies will increasingly underpin applications across a range of diverse industrial sectors in health care, energy, aerospace, environment, automotive, and security.

1.2 MEMS

MEMS (Micro Electro-Mechanical System) is a technology which runs on a field of micron to millimeter levels of mechanical designs and is related to device manufacturing, research, and implementation. It enables the miniaturization of conventional systems and extends their scope of application due to the reduction in size.

The field of micro-machined sensors and actuators has been of interest to the engineering world since the 1980's. The first impressive review of the applications of silicon as mechanical material, more than electronic material, was published by Kurt Petersen in 1982 [2]. Almost at the same time, Howe first proved the evolution of a very useful method to build micromechanical elements using technologies developed first from building microelectronic devices for the integrated circuits in seminal work done in 1982. R. T. Howe demonstrated techniques to fabricate microbeams from polycrystalline silicon films [3]. With the encouragement of this demonstration, Howe built the first prototype polysilicon MEMS, a chemical vapor sensor which was a fully integrated micromechanical and microelectronic system [4].

Research and development in MEMS have made remarkable progress since1988, when an electrostatic micromotor the size of a human hair was first operated successfully [1]. Since then, many types of microactuators utilizing various driving forces and mechanisms have been developed. Distinctive features of MEMS (miniaturization, multiplicity of components, and the integration of microelectronics) have led to promising application areas. For example, micromachines can travel freely into narrow spaces such as blood vessels. Connectors and harnesses hindering the further miniaturization of electronic equipment will be miniaturized by MEMS technology [1].

However, the mere miniaturization of macroscopic machines is not the most efficient way to understand MEMS. The same physical laws govern the microworld as the macroworld, but the relative importance of individual effects changes dramatically when the size of the machine decreases [1]. The way the machine completes tasks in the microworld may also be very different. Like a swarm of ants carrying away a large piece of food, cooperative work from many small microelements may be required to perform a large and complex task; however, one single device can only produce a small force or a very simple movement on its own [1]. Through cooperating of many elements, flexibility of motion, expandability, and immunity against failure of elements can be achieved. Multiplicity is thus one key to successful microsystems. Many actuators cannot only be fabricated in parallel but can work cooperatively to do things impossible for a single device alone. And the coordination of these elements is controlled by merging them with integrated microelectronics.
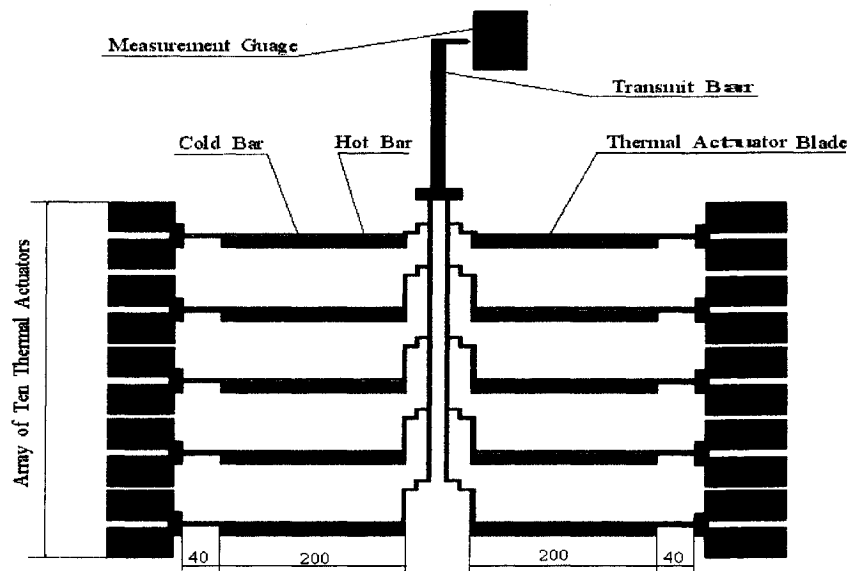
Figure 1.1: Array of ten actuators [5]

Due to its small size, unconventional mechanical manufacturing process must be used, and in fact, much of the MEMS technology is borrowed from the highly

3

matured microelectronics industry, which also deals with objects at the micro or even sub-micro level. Because MEMS uses silicon as a mechanical material, integrating devices, combining transducer elements and microelectronic circuits are facilitated. Once a process has been proved reliable, it is possible to create many structures on a wafer, resulting ultimately inexpensive production [6].

MEMS and microsensors are revolutionising the semiconductor industry. It gives us an insight into a microsystem or the so-called "system-on-a-chip", which combines microelectronic circuitry together with microsensors and microactuators (Figure 1.2 and 1.3). Many new applications can be implemented by this technology, these applications ranging from the electronic nose and intelligent ear to micro-tweezers and the very common ink-jet nozzle.
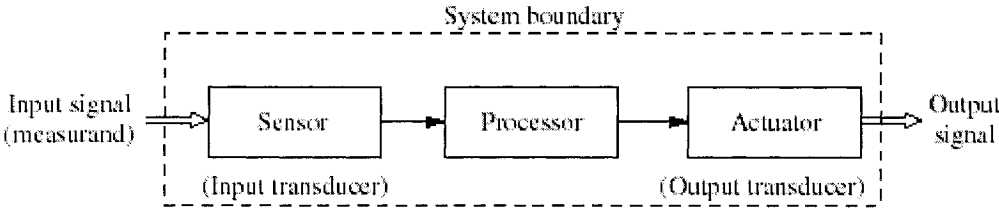
Figure 1.2: The information-processing diagram (from Gardner 1994)
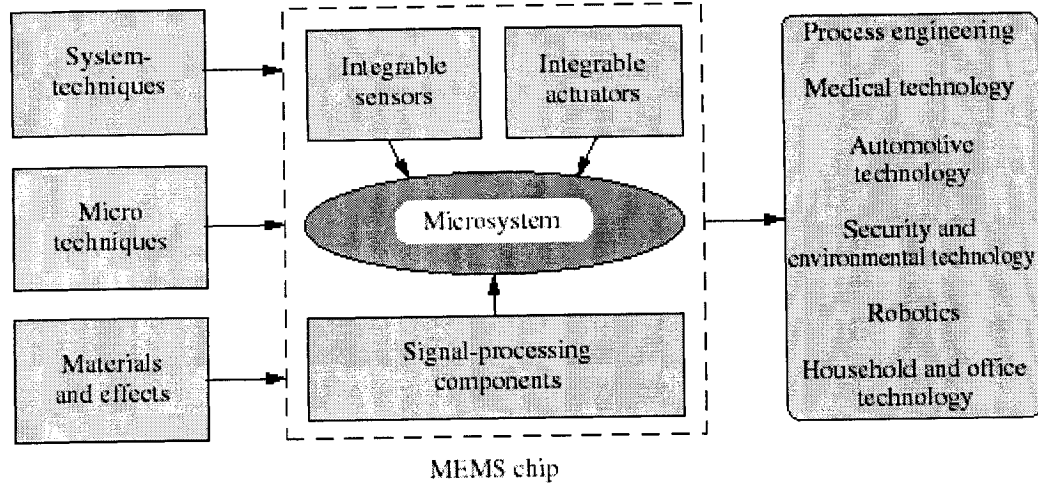
Figure 1.3: Overview of microsystems technology and the elements of a MEMS chip
(from Fatikow and Rembold 1997)

MEMS is an enabling technology, that is focusing on realization of micromechanical structures in the vicinity of the microelectronics circuits that along with the software component yield useful devices that usually work based on different physical principles than those on which the conventional mechanical systems are built on. Figure 1.4 shows the various science disciplines and industrial fields that concurs in realization of MEMS.

5
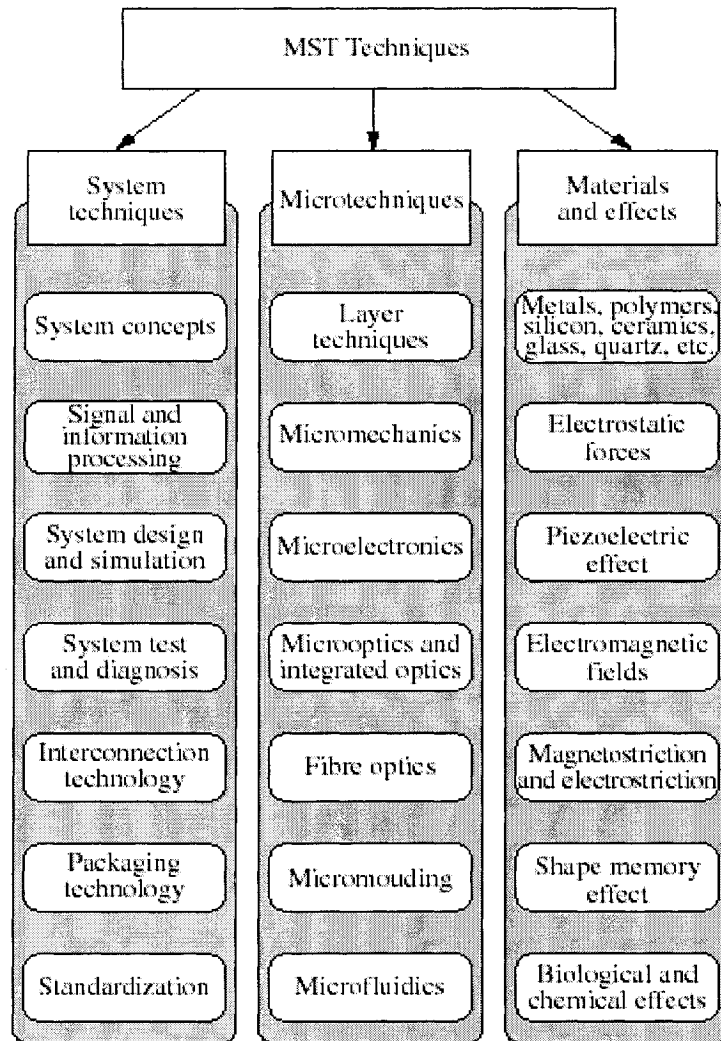
Figure 1.4: Some of the many fundamental techniques required and physical principles used to make MEMS devices (from Fatikow and Rembold 1997)

Due to its miniature size, MEMS have many characters that are within the working mechanism and design methods different from that of conventional electro-mechanical systems. In the working mechanism, the electro-magnetic force effect is not so serious, while the electro-static and dynamic force prevails. The surface capillary and thus the associated sticking forces are sometimes so strong that it is critical to release MEMS products.

1.3 Microactuators

Webster's dictionary (Merriam 1995) defines an actuator as "a mechanical device for moving or controlling something." An actuator is designed to deliver a desired motion when it is driven by a power source. Microactuators are the key devices allowing MEMS to perform physical functions. Microactuators are the key part in MEMS. Many types of microactuators have been successfully fabricated. They can be divided into two categories: one based on driving forces and the other based on mechanisms. Force can be generated in the space between stationary and moving parts using electric, magnetic, and flow fields. Materials have intrinsic actuation capabilities. Many actuation mechanisms, thermal expansion and phase transformations such as the shape-memory effect and bubble formation cause shape or volume changes.
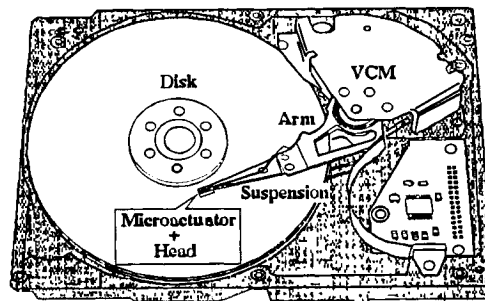
Figure 1.5: MEMS piggyback actuator for HDD head positioning [7]

Microactuators are sometimes required to drive resonators to oscillate at their resonant frequencies; they could be used to produce a required mechanical output

within a particular microsystem. They may also be used as a scanner or a switch used to actuate micropumps for microfluidic systems.

Various actuation principles have been used to design specific structures for assigned applications. Four principal means are commonly used for actuating motions of microdevices: (1) thermal forces, (2) shape memory alloys, (3) piezoelectric crystals and, (4) electrostatic forces. Although electromagnetic actuation is widely used in devices and machines at macroscales, it is rarely used in microdevices because of the unfavorable miniaturization scaling laws [6].

1.3.1 Shape-Memory-Alloy Microactuators
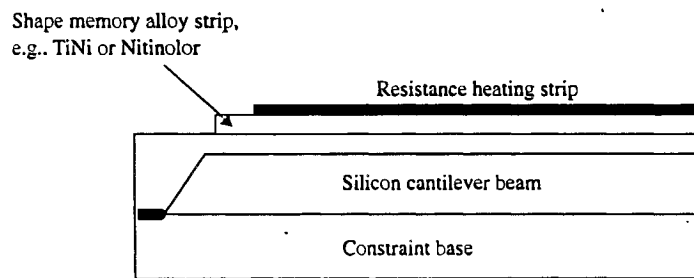
Figure 1.6: Schematic view of a shape-memory-alloy microactuator [6]

Shape memory alloys (SMA), such as Nitinolor, or TiNi alloys, can produce more accurate and effective microactuation by returning to their original shape at a preset temperature. An SMA strip, as shown in Figure 1.6, originally in a bent shape at a designed temperature T, is attached to a silicon cantilever beam. The beam is set straight at the room temperature. However, heating the beam with the attached SMA strip to the temperature T would prompt the strip's "memory" to return to its original bent shape. The deformation of the SMA strip causes the attached silicon beam to

8

deform with the strip, and microactuation of the beam is thus achieved. This type of actuation has been extensively used in micro rotary actuators, microjoints in robots, and microsprings.

1.3.2 Piezoelectric Microactuators
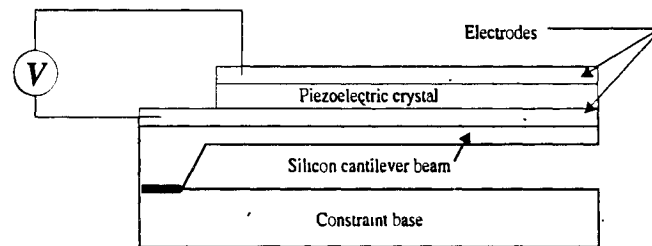
Figure 1.7: A microactuator using a piezoelectric crystal [6]

Certain crystals, such as quartz, that exist in nature, deform with the application of an electric voltage. The reverse is also valid. We may attach such a crystal to a flexible silicon beam in a microactuator, as shown in Figure 1.7. An applied voltage across the piezoelectric crystal prompts a deformation of the crystal, which can in turn bend the attached silicon cantilever beam. Piezoelectric actuation is used in a micropositioning mechanism and microclamps.

1.3.3 Electrostatic Microactuators

Electrostatic forces are used as the driving forces for electrostatic microactuators. Electrostatic force F is defined as the electrical force of repulsion or attraction induced by an electric field E. An electric field E exists in a field carrying positive and negative electric charges. Charles Augustin Coulomb (1736-1806) discovered this phenomenon and postulated the mathematical formula for determining the magnitude of the force F between two charged particles.

Length L = 1000 μm
Width W = 1000 μm
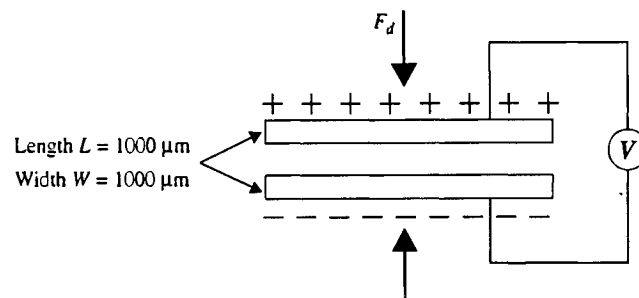
Figure 1.8: Schematic diagram of electrostatic microactuator [6]

Figure1.8 represents a simple parallel-plate style electrostatic microactuator. The electrostatic force is created by applying the voltage across the two plates, which are separated by a dielectric material (such as air).

The electrostatic microactuator is one of the most popular microactuators in MEMS applications. The well-known electrostatic microactuators include comb-drive microactuators, and wobble micromotors.

10
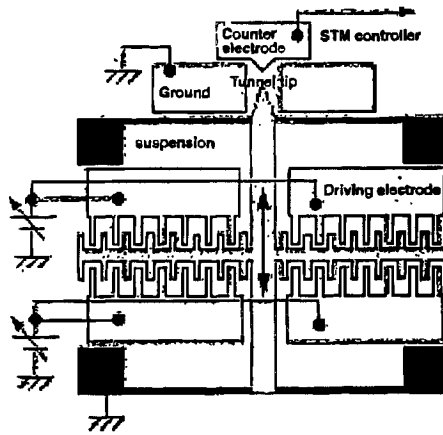
Figure 1.9: The electrostatic comb-drive actuator and tunneling tip [8]

1.3.4 Thermal Microactuators

1.3.4.1 Introduction

The literature reports an abundance of MEMS devices which utilize thermal effects. From measuring mass-flow rates with a thermal anemometer, to writing data onto a polycarbonate disk using heated cantilevers, to mimicing the way six-legged insects walk through microrobots [9], research programs are continually exploring new ways of using thermal expansion and thermally driven effects.
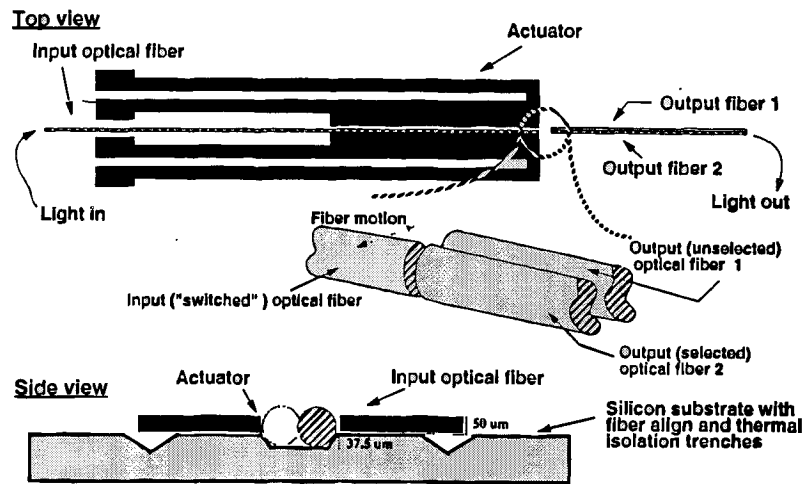
Figure 1.10: Micromechanical optical-fiber switch actuated by thermal actuators [10]

Thermal actuators have some advantages over other micro actuation methods: they provide fairly large forces in less volume (in the order of a few micro-Newton) and large displacement at CMOS compatible voltages and currents. Moreover, they are usually simpler, more reliable and easier to construct and to control. However, thermal actuators are much slower and use more power than the electrostatic devices.

Generally speaking, according to their components and actuation principles, three kinds of MEMS thermal actuators are widely used in commercial and research areas. They are thermal **bimorph** actuators, **rectilinear** thermal actuators, and **U-shaped** thermal actuators.

1.3.4.2 Thermal Bimorph Actuators

Thermal bimorph actuators are composite structures made of two or more layers of materials with different coefficients of linear thermal expansion. Their actuation is based on the so-called bimetal effect used extensively for the fabrication of temperature-controlled electrical switches. Bimorph sandwich layers act as actuators,

12

when heated, the mismatch of the thermal expansion coefficients causing the beam to bend.
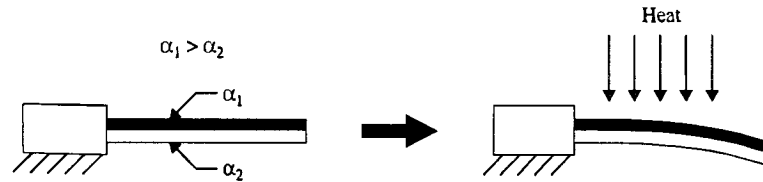
Figure 1.11: Schematic view of the "bimetal effect" for dissimilar materials in thermal actuators [6]

The silicon microactuator consists of a Si-metal sandwich layer and an integrated poly-Si heating resistor as a driving element. Due to the low heat capacity of the transducer element, a higher temperature per input power unit can be achieved. A number of different thermal bimorph integrated cantilevers have been realized. Biethmuller and Benecke [10] designed a Si-Au cantilever-type actuator, $500\,\mu m$ long and several micrometers thick, and measured a specific deflection of approximately $0.1\ \mu m/K$ at the free end. Baltes et al. [11] studied the concept of thermally excited microactuators and compared different silicon and metal bimorph materials. These thermally actuated microgrippers [12] and scanning mirrors [13] based on an aluminum-silicon double layer have been developed. Schweizer et al. [14] used organic materials as bimorph components, and designed SiO_2-metal thermally actuated optical microscanners. Mechanical scan angles greater than $90°$ have been achieved with these microscanners. Tuantranont et al. [15] designed and fabricated thermal multimorph actuators by MUMPs process. The actuator consists of a multilayer micromachined beam constructed of various combinations of polysilicon, oxide and metal layers. Embedded polysilicon wires are used to heat the multimorph to achieve tip deflection.
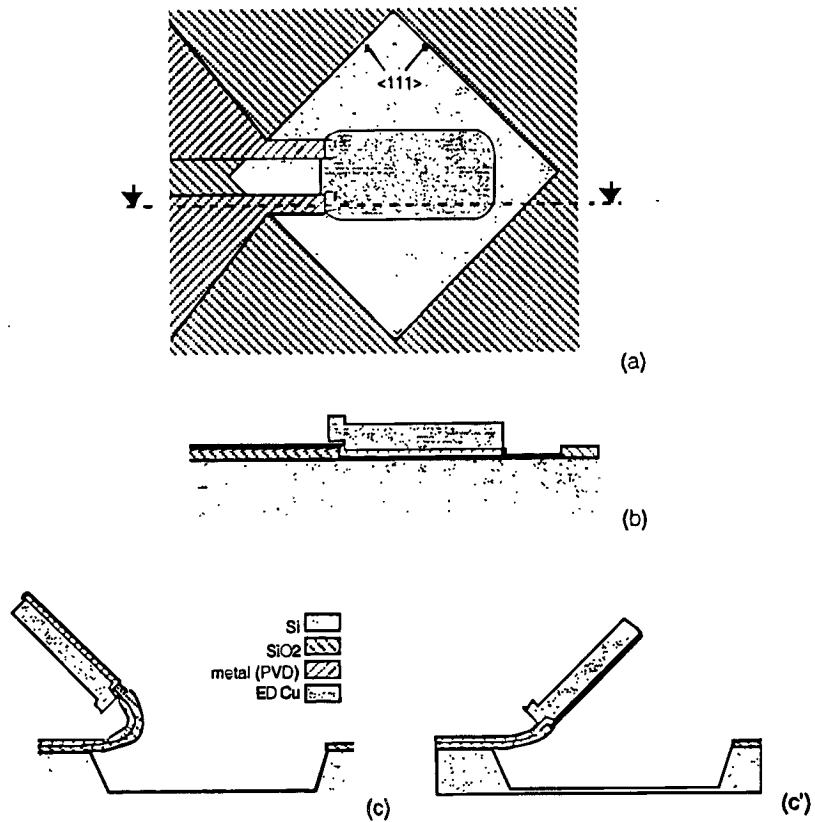
Figure 1.12: Thermally actuated optical microscanner (a) device top view (b) cross-section of device before release (c) cross-section of device after release—long beam (c') cross-section of device after release—short beam [14]

1.3.4.3 Rectilinear Thermal Actuators

The simplest use of thermal effects in MEMS is directed by thermal expansion. The rectilinear thermal actuators are based on this principle. A typical system is sketched in Figure1.13.
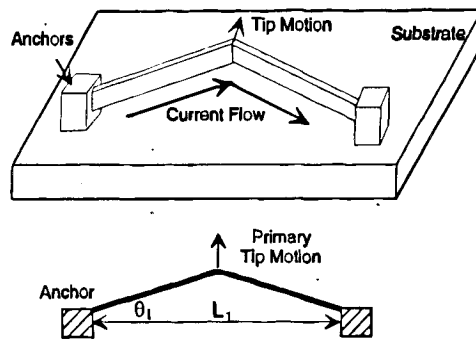
Figure1.13: Structure of a basic single bent beam rectilinear electro thermal actuator [16]

Here is a v-shaped beam anchored at two ends. When a current passes through the beam, it results in a rise in temperature due to Joule heating. The temperature increase causes thermal expansion of the beam, which pushes the knee point outward. The displacement of the tip point is a function of the beam dimensions and slope.

The rectilinear thermal actuators operate by elastic deformation via localized thermal stresses to transmit a force or displacement. They do not require structural segments with different expansions, and they are easily implemented with a single material. They also offer various other advantages: the displacements produced are rectilinear rather than curved, actuation voltages are relatively low while thermal time constants are relatively small because of the low thermal mass of these structures.

Simple and cascaded bent-beam electro thermal actuators have been used for rectilinear motion parallel to the substrate plane by Que et al. [16]. These actuators produce maximum displacements and maximum blocking forces (defined as the forces which null the displacement) in the range of $8\,\mu m$ and 2.5mN, respectively. However, in many applications a higher displacement is necessary, a smaller force is adequate, and the operating speed of the incremental mechanisms, like those of inchworms, is insufficient. Chu et al. [17] designed scalable, beam-based compliant microtransmissions that can be coupled with thermal actuators to increase the peak displacement of electrothermal actuators, from several microns to $100\,\mu m$. The

design process uses a two-stage approach: truss elements were used for the topology synthesis and beam elements were used for the dimensional optimization.
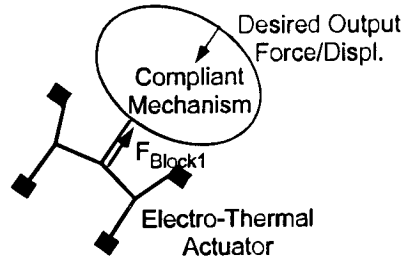
Figure 1.14: Cascaded bent beams can be used to amplify motion [17]

1.3.4.4 The U-shaped Thermal Actuators

Another kind of compliant thermal actuators are the U-shaped thermal actuators. They comprise polysilicon, an unitary material, and their operation is based on selective non-uniform Joule heating and the accompanying constrained thermal expansion.
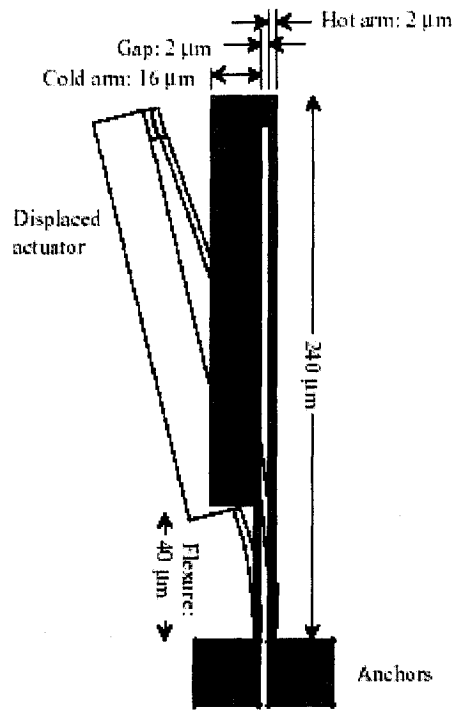
Figure 1.15: Scheme of a U-shaped micro thermal actuator

A schematic of a standard U-shaped thermal actuator is shown in Figure 1.15. This kind of actuator works on the basis of a differential thermal expansion between the thin arm and the blade. A potential difference applied across the electrical connection pads induces a current to flow through the arm and the blade. The current flow and the electrical resistance of the polysilicon results in Joule heating (I^2R) that is greater in the thin arm than in the blade. Non-homogeneous resistive heating is due to the variable cross section of the structure. This produces greater thermal strain in the thin arm than in the blade, and hence bending of the structure. Temperatures in the range of 300 -1500 K are generated. In this way, the U-shaped thermal actuator converts electrical energy to mechanical energy.

U-shaped microactuators yield a high output force (1mN) at a significantly lower drive voltage (5-10V) than electrostatic actuators of comparable size, which have output forces of (1 μ N) at drive voltages of 100V. However, the power consumption of the thermal actuators is significantly higher than that of the electrostatic actuator. U-shaped microactuators are also easy to fabricate because of their unitized construction and because they are compatible both with the manufacturing processes as well as with the voltage-current operation regime of CMOS microelectronics. These microactuators have therefore attracted a lot of attention in recent years.

Comtois et al [18] have characterized the steady-state and dynamic performance of the microactuator and proposed guidelines for its design. Lerch et al [19] have reported on a finite element (FE) analysis of a gripper based on the microactuator for a maximum temperature in the device of approximately 800K. The FE simulations yielded a temperature distribution that agreed to within 10% of the temperature distribution obtained from IR photo-thermometry. Lin and Chiao [20] have used FE simulations to study the electrothermal response of lineshape microstructures. Jonsmann et al [21] have introduced FE simulation-based topology optimization as a tool for systematic design of planar U-shaped microactuators. Moulton and Ananthasuresh [22] have used FE simulations to demonstrate a building-block approach to the synthesis of general U-shaped microactuator devices.

Lin and Chiao [20] have used numerical simulations to obtain an empirical shape factor that accounted for the modes of heat transfer in wide enough plate-like microstructures suspended over substrate by thin 2 μ m air film. The analytical model of the thermal actuator presented by Qing-An Huang and Neville Ka Shek Lee [23], simplified the thermal analysis of the horizontal U-shaped thermal actuator as a one dimensional problem, and used force method and virtual work method to solve thermal mechanical problems, built a model based on an understanding of conductive heat transfer via an air gap between structure and substrate as the main means for the

heat dissipation, and used force and virtual work method to calculate the deflection at the tip. Surface heat transfer by convection and radiation at high operation temperatures (above 500K) are important. A comprehensive thermal model, considering thermo physical properties temperature dependant, was proposed by Nilesh D. Mankame and G. K. Ananthasuresh [24]. This model which considers convective and radiative heat transfer as the main cause of heat loss, was built and solved by finite element analysis, and then validated experimentally. The SiCN ceramic thermal actuators, which can be used in ultra-high temperature (exceeding $1500\,^{\circ}C$) and corrosive environments, were developed by Liew, et al. [25].

Each of the above models has its useful characteristics, but they all focused on the model's thermal structure and for the mechanical part, they obtained displacement only at the tip. As a dynamic structure, many properties are of importance to the users, and to those who intend to optimize the actuators of importance are : the force generated at the tip, the first natural frequency of the structure, the frequency caused by thermal effect, the stiffness of the structure, the stress in the structure, the efficiency. Indeed some questions perpetually confuse designers and users, for example: how do geometries influence the dynamic performances? What is the way to make effective trade-offs between dimensions to meet different requirements? How to evaluate the safety of designs before they are put into manufacture? The objective of this thesis is to study the dynamic characterizations of U-shaped micro thermal electro actuators in order to find some relations between geometries and their dynamic behaviors.

1.3.5 Comparison among Actuation Principles

Each actuation principle has its advantages and disadvantages. The choice and the optimization of an approach should be made according to the requirements of a particular application. Generally speaking, the electrostatic actuators are more suitable for performing tasks that can be completed within a chip (e.g., positioning of devices/heads/probes, sensors with servo feedback for selftest or readout, light deflection and modulation) since it is easily integrated on a chip, easily controlled, and consumes little power. In contrast, the other types of actuators are more robust, more capable of producing larger forces, and more suitable for performing external tasks (propulsion, manipulation of objects).

Ideally, actuators would have low power consumption, high force per unit volume, simple construction, reliable and repeatable operation, design flexibility, simple drive and control circuitry, and be compatible with the fabrication process.

1.4 Thesis Objectives Overview

The main objectives of this thesis are: (1) to carry out modeling and to perform theoretical analysis of a standard U-shaped micro thermal actuator in detail, in order to find its thermal and dynamic behaviors in relation to the geometry of the device. (2) to perform experimental validation of the model. (3) to conduct simulation by FEM, and extrapolation for different geometric conditions based on the model developed in the first part.

In Chapter 2, using preliminary assumptions, a thermal model is built and the electrical and thermal analyses are presented according to both the theory of Joule heating. The thermal equation of the one-dimensional energy balance under steady state conditions is proposed. The model is solved numerically using Matlab.

In Chapter 3, on the basis of the temperature distribution results obtained from Chapter 2, the dynamic performances of this thermal actuator are analyzed as it follows:

- The maximum stroke at the tip
- The mechanical natural frequency of the structure
- The stiffness of the structure
- The force generated at the tip
- The stress analysis
- The frequency caused by thermal effect
- The efficiency

In Chapter 4, the fabrication process is described and experimental studies on U-shaped micro thermal actuators, processes, phenomena, and results are reported.

In Chapter 5, a Finite Element model is used to simulate the structure:

- Temperature distribution on the beam
- Displacement

Comparisons among theoretical analysis, FEM and experimental results are shown in figures. Simulations with different geometric designs are explained and accompanied by figures. From these simulations, thermal and mechanical behaviors changing with geometry can be seen obviously, and safety range can be determined for each design.

Conclusions and future work proposal conclude the work. The key findings are highlighted and recommendations for future work in this area are briefly detailed.

CHAPTER 2 ELECTRICAL AND THERMAL ANALYSES

2.1 Introduction

In this chapter, a generic U-shaped micro thermal actuator, as shown in Figure 2.1, is chosen, and electrical and thermal analyses are carried out. Micro thermal actuators could be fabricated in most of the available multi-user technologies. MUMPs built U-shaped thermal actuators will be considered throughout this thesis. The analyses consider the interaction (coupling) between thermal and electrical performance.
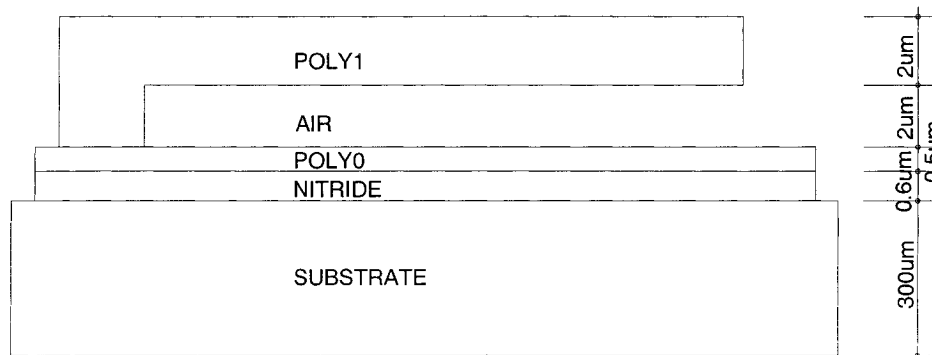
Figure 2.1: The diagram of the U-shaped micro thermal actuator's cross-section in MUMPs process [26]

22
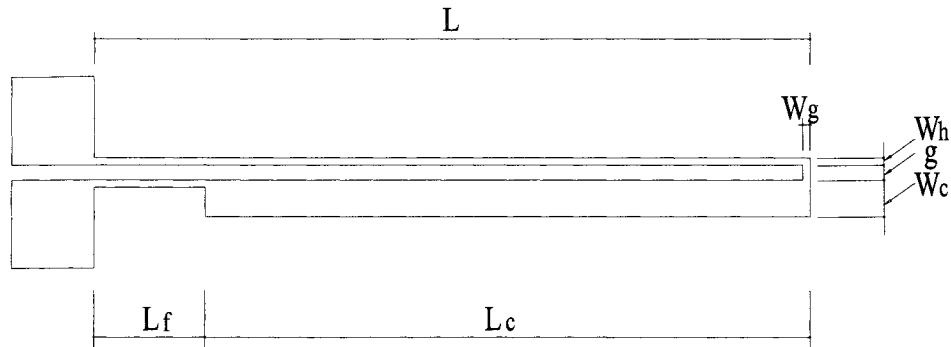
Figure 2.2: U-shaped micro thermal actuator

The configuration of the thermal actuator is as illustrated in Figure 2.1. Since such thermal actuators have been fabricated in MUMPs technology, the validation and the generic size of the actuator is assumed as for the physical realization. The geometric dimensions of the physically available thermal actuators that are used for experimental validation, are given in Table 2.1.

Table 2.1 Geometric dimensions of the benchmark thermal actuator

L	$970 \mu m$
L_c	$820 \mu m$
L_f	$150 \mu m$
g	$7 \mu m$
W_h	$3 \mu m$
W_c	$50 \mu m$
W_f	$3 \mu m$
W_g	$3 \mu m$
h	$2 \mu m$

The electrical input is provided by a voltage source. Since it has been experimentally determined that the thermal actuator is destroyed when voltage higher than 25V are applied between the two contact pads, the applied voltage range is taken from 0 to 20V.

The environment temperature is assumed to be 300K. The mechanical, electrical and thermal properties of the polysilicon are MUMPs service supplied, and are provided in Table 2.2.

Table 2.2 Material properties of the polysilicon in MUMPs technology

Material Properties (at 300K)	Quantity and Units
Young's modulus E	190GPa
Electrical resistivity r_s	$1.1 \times 10^{-5} \Omega \cdot m$
Thermal conductivity of polysilicon K	$200 W/m \cdot K$
Thermal expansion α	$2.6 \times 10^{-6} m/m \cdot K$
Emissivity ε	0.7
Density of polysilicon ρ	$2330 Kg/m^3$
Stefan-Boltzmann constant σ	$5.667 \times 10^{-9} W/m^2 \cdot K^4$
Specific heat capacity of polysilicon C_p	$678 J/Kg \cdot K$
Thermal conductivity of air K_{air}	$3.9107 \times 10^{-2} W/m \cdot K$
Prandtl number Pr	0.681
Kinematic viscosity of air υ	$3.5319 \times 10^{-5} m^2/s$

The electrical resistivity of polysilicon r changes with temperature and it can be described by the temperature coefficient c, and the electrical resistivity r_s, at the 300K:

$$r(T) = r_s [1 + c(T - T_s)] \quad (\Omega \cdot m) \tag{2.1}$$

where

$$c = 1.6 \times 10^{-3} K^{-1}$$

$$r_s = 1.1 \times 10^{-5} \Omega \cdot m$$

$$T_s = 300K$$

2.2 Electrical Analysis

The resistance of the actuator can be determined by assuming the resistance of the segments of the thermal actuator between the two contact pads as follows:

$$R(T) = (\frac{L}{W_h \cdot h} + \frac{L - L_f}{W_c \cdot h} + \frac{L_f}{W_f \cdot h} + \frac{g}{W_g \cdot h}) r(T) \quad (\Omega) \tag{2.2}$$

where the geometric parameters are as those illustrated in Figure 2.1 and 2.2

$R(T)$ - the total resistance,

L - the length of the hot arm,

L_f - the length of the recess in cold arm,

g - the length of the gap between hot and cold arms,

h - the actuators thickness,

25

W_h - the width of the hot arm,

W_c - the width of the cold arm,

W_f - the width of the flexure,

W_g - the width of the gap,

$r(T)$- the resistivity of polysilicon as the relation (2.1)

The Joule heating generated by the thermal actuator is:

$$E_g = I^2 R(T) = \frac{U^2}{R(T)} \quad (\text{W})$$ (2.3)

here, I is the current, and U is the voltage.

In the relation (2.3), U is assumed constant while R changes with the temperature.

2.3 Thermal Analysis

Figure 2.3 illustrates the layout of a U-shaped micro thermal actuator, fabricated by surface micromachining. The size of the cross section of the actuator is much smaller than its length. Therefore, the whole actuator could be regarded as a beam, which means that the temperature gradient occurs just along the length of the structure, and at each cross-section the temperatures is the same. As a result, the eletrothermal analysis of the U-shaped actuator is simplified to a one dimensional problem.

26
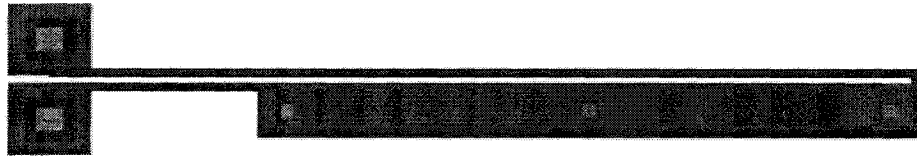
Figure 2.3: U-shaped micro thermal actuator in MUMPs technology

Therefore, the electric-thermal analysis for the structure is carried out by deriving the differential equation of heat conduction for a stationary, homogeneous, isotropic solid with heat generation within the body while convective and radiative heat dissipate to the ambient.

Heat is transferred from a hot to colder ambient through conduction, convention, and radiation. Conductive heat transfer is the transport of heat energy from high temperature to low temperature region. Convective heat transfer happens between a surface and a fluid, as a result of a temperature difference. The radiative heat transfer is the energy emitted in the form of electromagnetic waves from a body due to its temperature.

The dominance of the heat transfer mechanisms will modify according to the specific thermal condition under which the heated system and the ambient interact. Therefore, before the system is at the steady state, the temperature gradient on the structure occurs because of conductive heat transfer. While the temperature difference between the structure and environment is increasing, convective heat transfer and radiative heat transfer occur, and heat energy is dissipated to ambient. When the whole system reaches equilibrium, the input electrical energy is balanced by the dissipated energy through conduction, convection, and radiation. The conduction occurs though the entire thermal actuator structure and the heat is taken

27

by the contact pads through the mass of the chip structure that is assumed as ambient and therefore a heat sink.

The convection is carried through the air surrounding the thermal actuator and the amount of transferred heat will be dependent on the temperature gradient. Further, the entire thermal actuator will radiate heat in different amount according to the temperature of the zone that radiates.

2.3.1 Assumptions and Simplifications

♦To evaluate the heat dissipation, one needs the temperature gradient through the structure as well as the boundary conditions.

♦To find temperature gradient, conduction mechanism would yield a distribution of temperature that would help to identify the convective and radiative dissipation effects.

♦However, to evaluate the conductive dissipation, information about the convective and radiative dissipation is needed.

Certain assumptions will be made to evaluate the amplitudes that occur with the three dissipative phenomena. Here, the electrical resistivity of polysilicon r is changing with the temperature and is determined by the averaged temperature of the whole structure T_{av}. Properties such as convective and radiative heat dissipations as well as the mechanical behaviors are all under the averaged temperature of the whole structure T_{av} too.

Two assumptions are made. First one is that the substrate is considered large enough compared with the thermal actuator, so that the temperature of two electrical pads as well as the substrate are assumed to be at the same temperature as that of the

environment which is at 300K. Further the heat flux flows from one point on the hot arm, which is at the highest temperature of the beam, to the two electrical connection pads, in two opposite directions. The second assumption is for the cold arm. Because it generates relatively small energy of 4.2%, the temperature in cold arm changes little.

2.3.2 The Energy Equilibrium Equation

The one-dimensional energy balance equation is derived by examining a differential volume element of the micro beam under steady state conditions, which means the system is up to balance, and energy is not changing with time, ($\frac{dT}{dt} = 0$).
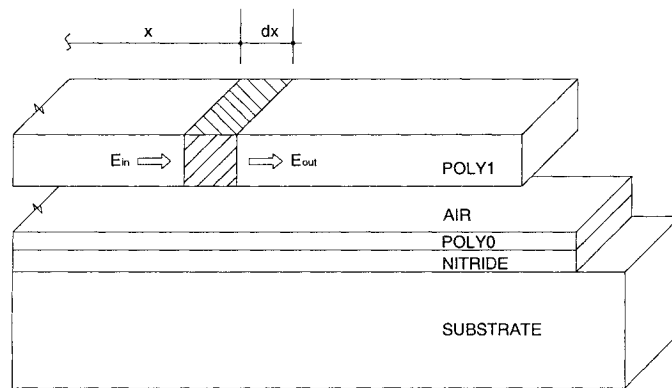
Figure 2.4: The schematic cross section of the U-shaped micro thermal actuator for thermal analysis

For the elemental volume δV of thickness dx, as shown in Figure2.4, the energy balance equation is stated as:

[Rate of heat entering the δV (W)] + [Rate of energy generation in δV (W)]

= [Rate of heat out of δV (W)] + [Rate of heat dissipating to ambient (W)]

$$E_{in} + E_{generate} = E_{out} + E_{dissipate}$$

$$A(x)q_x + E_g\frac{dx}{l} = A(x)q_x + \frac{\partial}{\partial x}[A(x)q_x]dx + (Q_V + Q_R)\frac{dx}{l}$$

Substituting the Fourier's Law: $\qquad q_x = -K\frac{\partial T}{\partial x}\left(W\!\!\big/_{m^2}\right)$

we get: $\qquad\qquad\qquad\qquad Kl\frac{\partial}{\partial x}\left[A(x)\frac{\partial T}{\partial x}\right] = -E_g + Q_V + Q_R$

Here, $A(x)$ represents the area of cross-section. The heat flux vector $q(x,t)$, represents heat flow per unit time, per unit area of the isothermal surface in the direction of the decreasing temperature. Heat flux controls the rate of heat flow in the structure. E_g is the input energy rate (as from 2.3); Q_V is the dissipated heat rate through convection (as from 2.6); Q_R is the dissipated heat rate through radiation (as from 2.7); and l is the general length along the contour of the structure.

Under the assumptions in 2.3.1 the heat energy equilibrium equation is changed to:

$$KV\frac{\partial^2 T}{\partial x^2} = -E_g + Q_V + Q_R \qquad\qquad (2.4)$$

V is the volume of the whole structure.

Boundary conditions:

30

x=0, T=300K

x=L+L_f+g, T=300K

The temperature distributions on the hot arm and flexure is a parabola, as shown in Figure 2.5, with the peak temperature at x=$(L+L_f+g)/2$.
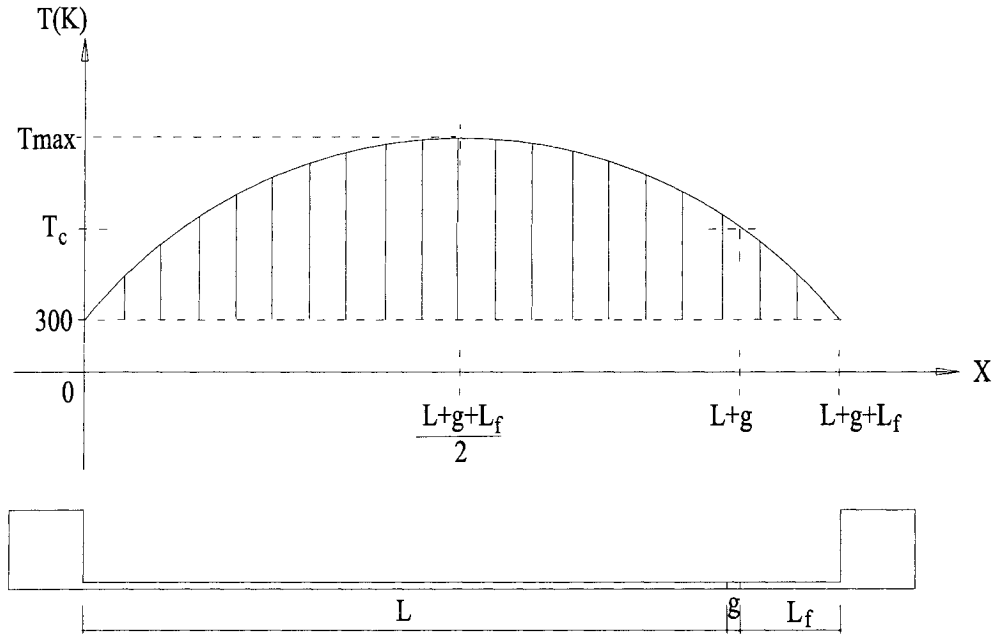
Figure 2.5: The temperature distributions on the thermal actuator

2.3.3 Heat Dissipation

Convective heat transfer to the surrounding air

In small structures, like MEMS, free convention occurring under buoyancy forces due to temperature difference is usually not important [27], and hence the convective heat transfer for micro thermal actuators belong to forced-convection heat transfer, caused by fluid motion forced externally, in the case of boundary-layer

31

flows over flat plates. For most of the applications in MEMS, flow speeds and sensor sizes are quite small and laminar flow can be assumed. Therefore, the situation of the thermal actuators in this thesis is similar to a boundary-layer flow is along a flat, hot plate parallel to the oncoming flow. The average Nusselt number Nu_{av} (averaged over the entire surface) for a plate of length L are given as following expressions:

$$Nu_{av} = h_{av} \frac{L}{K_{air}} = 0.664 \, Pr^{\frac{1}{3}} \, Re^{\frac{1}{2}} \qquad (2.5)$$

$$T_f = \frac{T_s + T_{av}}{2}$$

$$Re = \frac{Lv}{\upsilon}$$

Hence, the heat dissipation through convection:

$$Q_V = A_w h_{av} (T_{av} - T_s) \qquad (W) \qquad (2.6)$$

where: Nu_{av} --- average Nusselt number

h_{av} --- heat-transfer coefficient

T_f --- mean temperature, assumed at $T_f = 480K \, (T_{av} = 660K)$

Re   --- Reynolds number

Pr   --- Prandtl number

A_w --- whole surface area of the structure

v --- velocity of the air, assumed $v = 3 \frac{m}{s}$

Heat radiation to ambient

The Stefan-Boltzmann law of thermal radiation states that the power emitted to surroundings by a gray or black body is equal to:

$$Q_R = \varepsilon \sigma A_w (T_{av}^4 - T_s^4) \quad (W) \tag{2.7}$$

where: ε --- emissivity, for MEMS structure, we choose 0.7 [27]

σ --- Stefan-Boltzmann constant

A_w --- whole surface area of the structure

$$A_w = (L \cdot W_h + L_c \cdot W_c + L_f \cdot W_f + g \cdot W_g) \times 2 + ((L + L_c + L_f + g + W_c - W_g) \times 2 - W_f) \cdot h \tag{2.8}$$

2.3.4 Temperature Distribution on the Beam

Substituting (2.1), (2.2), (2.3), (2.6), (2.7) into (2.4), the heat energy equilibrium equation

$$KV \frac{\partial^2 T}{\partial x^2} = -E_g + Q_V + Q_R$$

is changed to:

$$K \cdot V \frac{\partial^2 T}{\partial x^2} = -\frac{U^2}{G \cdot r_s [1 + c(T_{av} - T_s)]} + A_w \cdot h_{av} \cdot (T_{av} - T_s) + \varepsilon \cdot \sigma \cdot A_w \cdot (T_{av}^4 - T_{av}^4) \tag{2.9}$$

Here, $G = \dfrac{L}{W_h \cdot h} + \dfrac{L - L_f}{W_c \cdot h} + \dfrac{L_f}{W_f \cdot h} + \dfrac{g}{W_g \cdot h}$

33

The exact solution of the differential equation (2.9) requires prior knowledge of the average temperature in the thermal actuator T_{av}. This prior knowledge requires experimental work that could eventually provide the expected value of the temperature achieved in each segment of the actuator. Unfortunately, the reducing size of the actuator complicates even more problems. The literature presents strategies in evaluating the temperature based on assumptions such as ignoring the radiative heat dissipation [23].

Below, trial and error calculations are applied:

In the temperature distribution calculations, an average temperature $T_{av}^{'}$ is assumed at the beginning to determine the resistivity and to obtain generated energy E_g, and then heat dissipation, Q_V, Q_R is calculated under assumed average temperature $T_{av}^{'}$. After we get the temperature distribution, we can obtain a result T_{av}.

From (2.4):

$$KV\frac{\partial^2 T}{\partial x^2} = -E_g + Q_V + Q_R$$

$$\frac{\partial^2 T}{\partial x^2} = \frac{1}{VK}(-E_g + Q_V + Q_R) = -\lambda \tag{2.10}$$

$$\frac{\partial T}{\partial x} = -\lambda x + B$$

$$T = -\frac{1}{2}\lambda x^2 + Bx + C$$

Here we determine λ as the *factor coefficient* of the temperature distribution.

Since the temperature gradient is only on the hot arm and the flexure, as from Figure 2.5, from the boundary conditions, C and B can be obtained:

The boundary conditions are:

$$x = 0 \quad , \quad T = T_s = 300K$$

So, $\quad\quad\quad\quad C = T_s = 300K$ (2.11)

and from: $\quad x = L + L_f + g \quad , \quad T = T_s = 300K$

$$T = -\frac{1}{2}\lambda x^2 + Bx + T_s$$

$$T_s = -\frac{1}{2}\lambda(L + L_f + g)^2 + B(L + L_f + g) + T_s$$

We get $\quad\quad B = \frac{\lambda}{2}(L + L_f + g)$ (2.12)

Therefore, the *temperature distribution* is given by the relation:

$$T(x) = \frac{\lambda}{2}x(L + L_f + g - x) + T_s \quad\quad \text{(K)} \quad \left(0 \le x \le (L + L_f + g)\right)$$ (2.13)

The *peak temperature* value $T = T_{max}$, will occur when $\dfrac{\partial T}{\partial x} = 0$

$$\frac{\partial T}{\partial x} = -\lambda x + \frac{(L + L_f + g)}{2}\lambda = 0$$

will occur at: $$x = \frac{L + L_f + g}{2}$$

$$T_{max} = -\frac{1}{2}\lambda\left(\frac{L + L_f + g}{2}\right)^2 + \left(\frac{L + L_f + g}{2}\right)^2 \lambda + T_s \quad (K) \qquad (2.14)$$

$$= \frac{\lambda}{2}\left(\frac{L + L_f + g}{2}\right)^2 + T_s$$

The *average temperature*:

For the hot arm:

$$\overline{T}_h = \frac{\int_0^{L+g} T(x)dx}{L + g} = \frac{\int_0^{L+g}[-\frac{\lambda}{2}x^2 + \frac{(L + L_f + g)}{2}\lambda x + T_s]dx}{L + g}$$

$$= -\frac{\lambda}{6}(L + g)^2 + \frac{(L + L_f + g)(L + g)}{4}\lambda + T_s \qquad (2.15)$$

For the flexure:

$$\overline{T}_f = \frac{\int_0^{L_f} T(x)dx}{L_f} = \frac{\int_0^{L_f}[-\frac{\lambda}{2}x^2 + \frac{(L + L_f + g)}{2}\lambda x + T_s]dx}{L_f}$$

$$= -\frac{L_f^2}{6}\lambda + \frac{(L + L_f + g)L_f}{4}\lambda + T_s \qquad (2.16)$$

36

The *temperature of the cold arm* $\overline{T_c}$, can be found from the temperature distribution equation at $x = L_f$:

$$\overline{T_c} = -\frac{1}{2}\lambda \cdot L_f \cdot (L + L_f + g - L_f) + T_s$$

$$= -\frac{1}{2}\lambda \cdot L_f \cdot (L + g) + T_s \qquad (K) \qquad (2.17)$$

Therefore, the *average temperature for the whole structure* T_{av} is:

$$T_{av} = \frac{\overline{T_h}(L \cdot W_h + g \cdot W_g) + \overline{T_f} \cdot L_f \cdot W_f + \overline{T_c} \cdot L_c \cdot W_c}{L \cdot W_h + g \cdot W_g + L_c \cdot W_c + L_f \cdot W_f} \qquad (K) \qquad (2.18)$$

Using computer program, the results show that the differences between the assumed average temperatures T_{av}' with the result average temperatures T_{av} converge gradually. The closest one is the final result.

2.4 The Result of the Joule Effect on the Temperature of the Micro Thermal Actuators

For the geometries of the thermal actuators used in the experiments are as Table 2.1, using Matlab, the results of the calculations performed under 5V, 10V, 15V, 20V, are listed below:

Table 2.3 Results of temperatures and energies

Voltage(V)	5	10	15	20	Relation number
$\left\|T'_{av} - T_{av}\right\|_{min} (K)$	2.9	4.2	1.1	3.5	
λ	5.7e8	1.9e9	3.7e9	5.6e9	(2.10)
$T_{max}(K)$	389.9	605.6	889.1	1193.8	(2.14)
$\overline{T}_h(K)$	365.8	523.6	731.1	954.1	(2.15)
$\overline{T}_f(K)$	321.8	374.1	442.9	516.8	(2.16)
$\overline{T}_c(K)$	341.5	441.1	571.9	712.5	(2.17)
$T_{av}(K)$	342.9	445.8	581.1	726.5	(2.18)
$Q_V(W)$	8.27e-4	0.0031	0.0058	0.0089	(2.6)
$Q_R(W)$	2e-5	1.3e-4	4e-4	1.1e-3	(2.7)
$E_g(W)$	0.0109	0.0374	0.0721	0.1099	(2.3)
$T^*_{max}(K)$ FEM(ANSYS)	377.579	584.764	874.053	1210.071	

The simulation result is shown in Table 2.3 and Figure 2.6. Obviously, the close agreement between the FEM results of the temperature distribution and those from theoretical analysis in this chapter prove that the assumptions in 2.3.1 are quite reasonable. Figure 2.6 shows that the maximum temperature appears at the middle part of the hot arm, and temperature reduces gradually to the two ends which are at the same temperature as the environment and in the cold arm the temperature does not change a lot. *Si* softens at about 350°C. One would expect in practice the yield of the structure and after cycling and some creep flow. However, this phenomenon has not been observed during the experimental work.
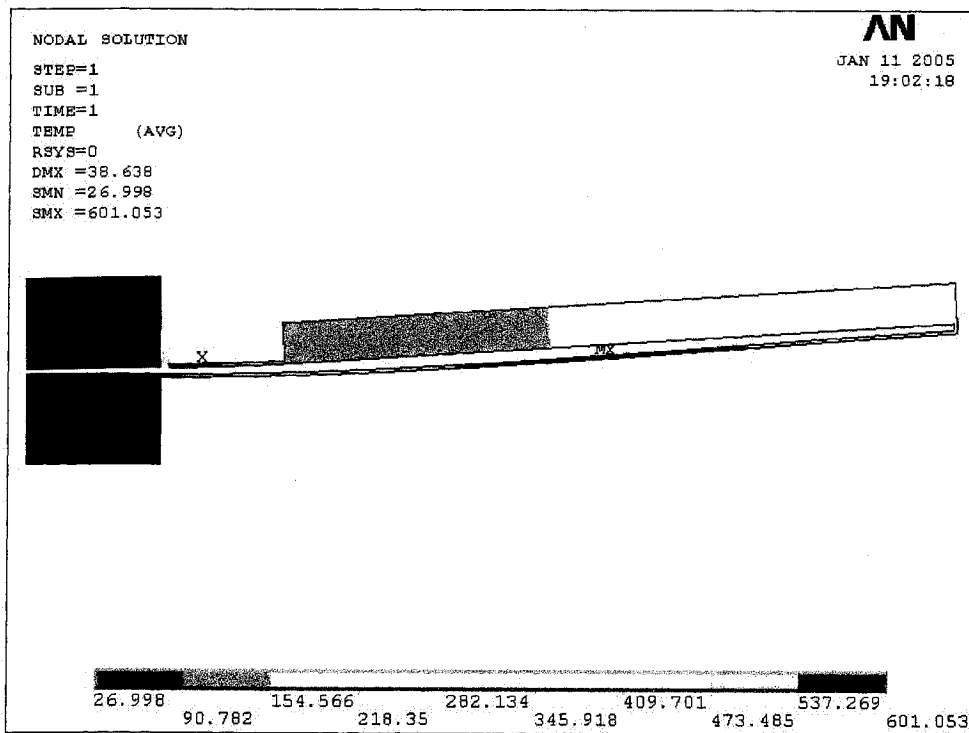
Figure 2.6: FEM result of temperature distribution along the structure ($^\circ C$) (under 15V)

CHAPTER 3 DYNAMIC CHARACTERIZATION ANALYSIS

Microactuators are intended for performing at small scale. The expected forces and displacement at micrometer level are scaled down through the reduced geometry of the structures. However, certain performances are required to satisfy the actuation needs.

Users are mainly interested to achieve motions for specific applications. The majority of microactuators perform oscillatory motions in rectilinear or angular path. The expected forces range from pN to mN while the stroke often not exceeding few micrometers. The frequency is another important feature of an actuator. Microactuators usually perform at high frequencies. Finally, the control and the efficiency of the microactuators will carry weight during their selection process.

The microactuators are on-chip devices. They are not off the shelf available items and the decision on the configuration of the microactuator is the designer's responsibility. Therefore, a good group on the performance of microactuators in conjunction with the specific geometry is required. Moreover, a prior knowledge of the performance of the microactuators is highly desired.

In the following chapter, analytical means to evaluate the performance of microactuators based on the geometric size of the design will be discussed.

The micro thermal actuator is studied as a continuous system, and energy methods (virtual work, and the Rayleigh-Ritz method) are used to analyze the deflection, force generated at the tip, and the natural frequency of the structure. Further, the stress and strain distributions are calculated along with the evaluation of the thermal resonant

40

frequency induced by the thermal cycle. This last quantity is instrumental in the evaluation of the maximum frequency at which the thermal actuator could function.

3.1 Deflection Analysis

3.1.1 Beam Expansion Method

The deflection analysis is carried out to evaluate the peak deflection of the tip of the actuator while an input step voltage is applied across the two pads. Chapter 2 relates the temperature gradient and average in the constituent segments of the actuator with the applied voltage. The basic model of the thermal actuator is assumed as being formed by two parallel beams. Pure bending is assumed in both beams with plane cross sections remaining plane (shear is negligible), as shown in Figure 3.1
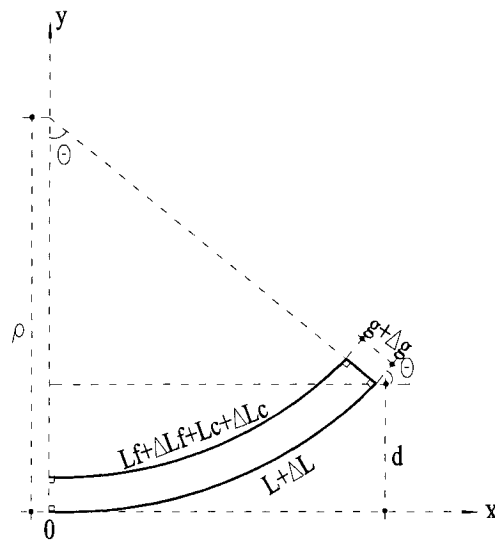
Figure 3.1 Schematic of the beams of a thermal actuator to a pure bending when heated

Since the deflection in beams is generally small, the following geometric relations are assumed to hold for a single beam:

$$\theta = \frac{dy}{dx}$$

$$\frac{d\theta}{dx} = \frac{d^2 y}{dx^2} = \frac{1}{\rho}$$

$$\frac{dy}{dx} = \frac{1}{\rho} x + C_1$$

$$y = \frac{1}{2\rho} x^2 + C_1 x + C_2$$

From the boundary conditions:

(1) at $x=0$, $y=0$, $\Rightarrow$ $C_2 = 0$;

(2) at $x=0$, $\frac{dy}{dx} = 0$, $\Rightarrow$ $C_1 = 0$.

$$y = \frac{1}{2\rho} x^2$$

At $x = L + \Delta L$

$$d = \frac{(L + \Delta L)^2}{2\rho}$$

As illustrated in Figure 3.1, the short beam is made from two constituent segments: the flexure and the cold arm. As the thermal expansion in each segment has been evaluated at the average temperature, the different thermal expansion in the three arms will yield the deflection d at the tip of the thermal actuator.

From geometry relations, as shown in Figure 3.1:

$$\rho\theta = L + \Delta L$$

$$(\rho - (g + \Delta g))\theta = (L_f + \Delta L_f) + (L_c + \Delta L_c)$$

ρ can be obtained by:

$$\frac{\rho\theta}{(\rho - (g + \Delta g))\theta} = \frac{(L + \Delta L)}{(L_c + \Delta L_c) + (L_f + \Delta L_f)}$$

$$\Rightarrow \rho = \frac{(L + \Delta L)(g + \Delta g)}{(L + \Delta L) - (L_c + \Delta L_c) - (L_f + \Delta L_f)}$$

When a beam is heated, it will expand. (law of expansion)
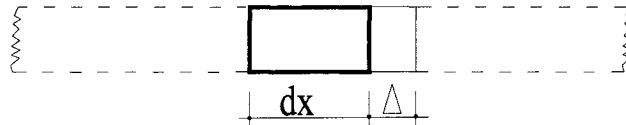
Figure 3.2: Schematic of the beam expand when heated

$$\Delta = \alpha(\Delta T)dx$$

where Δ represents the expansion of a discrete element; α is the linear thermal expansion coefficient of the specific material; ΔT is the variation of temperature. Further, results are obtained through assuming uniform temperature in each segment, and overall thermal expansion of each beam is calculated as an averaged temperature over the entire beam. (as from Table 2.3)

$$\Delta L_h = \alpha \cdot L \cdot (\overline{T_h} - T_s)$$

$$\Delta L_c = \alpha \cdot L_c \cdot (\overline{T_c} - T_s)$$

$$\Delta L_f = \alpha \cdot L_f \cdot \left(\overline{T_f} - T_s \right)$$

$$\Delta g = \alpha \cdot g \cdot \left(\overline{T_c} - T_s \right)$$

The results of deflections as the maximum stroke at the tip of the thermal actuator measured for the benchmark thermal actuator are shown in Table 3.1:

Table 3.1 Comparison between results from beam expansion method and the experimental results in deflection of the benchmark thermal actuator

U (V)	Beam expansion method(μm)	Experimental deflection (μm)	Difference (%)
5	3.3	Not observed	---
10	11.37	23	50.6
15	21.93	40	45.2
20	33.28	55	39.5

It is noticed that the simple beam deflection approach yields results that are about 50 % lower from those from the experimental test. A more accurate model of the deflection for the constituent beams of the thermal actuator that takes into consideration the elongation due to the thermal gradient in the beam does not yield much enhanced results.

Since the accuracy of the model considered is not satisfactory a more accurate analytical model with more detailed analysis of each segment of the actuator is proposed. From [23], the virtual work method in conjunction with the flexibility is used to evaluate the deflection caused by thermal expansion at the tip of micro thermal actuator. In this method, the bending moment of inertia I is also considered in an attempt to achieve more accurate results.

44

3.1.2 Virtual Work Method

The principle of virtual work was developed by Johann Bernoulli in 1717, and it forms the foundation for other energy principles and theorems. This method is widely used in the situations where displacement is required at any points where no external forces are applied, or along a different direction than the line of action of the applied loads, where it is not possible to apply the method of real work.

Complementary energy or work:
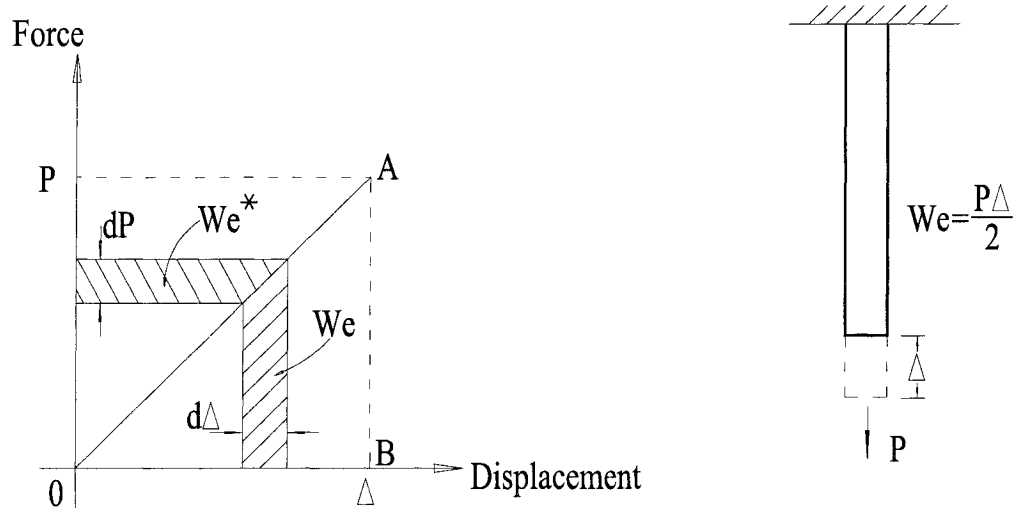
Figure 3.3: Linear elastic body subjected to a force P

Referring to the relationship between the force P and the displacement Δ in its line of action (as shown in Figure 3.3), the shaded area above the curve OA can be expressed as

$$dW_e^* = (\Delta)dp$$

Thus the total area above the curve OA is

$$W_e^* = \int_0^P (\Delta) dp$$

W_e^* is denoted as the external complementary work performed on the body; it should be mentioned that unlike the external work W_e, the complementary work W_e^* or energy has no physical meaning. Correspondingly, the expression for the internal complementary work, can be written as

$$W_i^* = \int_o^P (e) dP$$

where e is the extension in the member and P is the internal force in the member.

The external work W_e might strain or move the body on which it is applied. Therefore, the effect of the external work is transmitted as a potential internal energy denoted by W_i and a kinetic energy T:

$$W_e = W_i + T$$

For static condition, $T=0$, and

$$W_e = W_i$$

For nonlinear elastic structures, $W_i^* \neq W_i$ and $W_e^* \neq W_e$. However, for linear elastic structures, $W_i^* = W_i$ and $W_e^* = W_e$, as can be observed from Figure 3.3. In the absence of gross distortion (as is the case in real structures) it can be shown from the law of conservation of complementary work (or energy) that the external complementary work is equal to the internal complementary work.

$$W_e^* = W_i^*$$

Virtual work on an elastic body:

The word "Virtual" signifies that the displacement is independent of the forces, or the force independent of the displacements, and the virtual work is the product of real forces with virtual displacements or virtual forces with real displacements.

If an elastic body is in equilibrium and remains in equilibrium while it is subjected to a virtual distortion compatible with the geometrical constraints, the virtual work done by the external P forces is equal to the virtual work done by the P-induced internal stresses.

$$W_e = W_i$$

Real -force$\times$ Virtual -displacement= Real -internal-force$\times$ Virtual -internal-displacements

An analogous judgment can be carried out for the principle of *virtual complementary work on an elastic body* showing that:

$$W_e^* = W_i^* \qquad (3.1)$$

Here W_e^* is the virtual external complementary work and W_i^* is the virtual internal complementary work.

$$W_e^* = \sum_{i=1}^{n} (\delta P)_i D_i \qquad (3.2)$$

Here δP is a small virtual force applied to the elastic body, and it causes a real deformation pattern D along the direction of the virtual force.

47
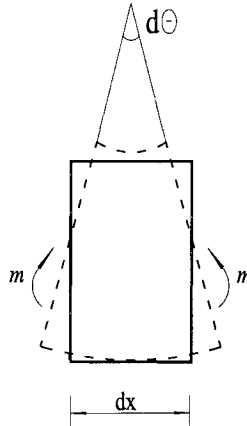
Figure 3.4: Form of the element of beam in bending under virtual internal
complementary work on the beam due to virtual moment m

Figure 3.4 shows a virtual moment m acting on the element dx with a real
displacement $d\theta$ caused by the applied external real moment M; the virtual work
performed by m on the element dx is

$$dW_i^* = m \cdot d\theta$$

The real displacement $d\theta$ is given by

$$d\theta = \frac{M}{EI} dx$$

Therefore

$$dW_i^* = m \frac{M}{EI} dx$$

For the entire beam, the internal virtual work becomes:

$$W_i^* = \int_0^L m \left(\frac{M}{EI} dx \right) \qquad (3.3)$$

48

Here the term m represents the internal virtual forces in a bent member while $(M\ dx/EI)$ represents the internal real displacement (rotation) in a bent member, M is an applied external real moment.

Virtual-force × Real-displacement = Virtual-internal-force × Real-internal-displacements

---

To determine the real displacements in a structure by the virtual work method, from (3.2), one finds that if a displacement D at only one point in a bent structure is required, a unit value for the external virtual force δP could be used and hence (3.2) reduces to

$$W_e^* = 1 \cdot D \tag{3.4}$$

Based on (3.1) and (3.3) one could find:

$$1 \cdot D = \int m \frac{M}{EI} dx \tag{3.5}$$

In this case the internal virtual moment m in the structure is the one due to a unit external virtual force applied to the structure at the point where the displacement is required; and M is the moment due to the external loads.

In the same way, the rotational displacement due by a unit virtual moment becomes:

$$1 \cdot \theta = \int_0^L m \frac{M}{EI} dx \tag{3.6}$$

49

3.1.3 Force (or flexibility) Method of Consistent Deformations

In analyzing an indeterminate structure, such as the double-clamped structure of the thermal actuators, we must arrive at a solution that satisfies the requirements of both equilibrium and compatibility. To meet these requirements two general approaches may be followed. In the first approach, a statically determinate solution is first assumed satisfying the equilibrium requirements; the geometrical errors incurred by such an assumption are then corrected without disturbing the equilibrium conditions by using compatibility equations—hence the name *compatibility approach*. Furthermore, the relations between forces and deformations are expressed such that deformations are in terms of forces and hence forces become the independent variables or unknowns to be determined. This is why such a method of analysis is referred to also as the *force (or flexibility) method* in which the relations between the forces and deformations are expressed through *flexibility coefficients*; the methods of three-moment equation, of consistent deformation, and of least work are classified as force methods. In the second approach, a solution is assumed satisfying the geometrical requirements; the resulting errors in static equilibrium are then corrected using equilibrium equations without disturbing the geometrical conditions—hence the name *equilibrium approach*. Here forces are expressed in terms of deformations by means of *stiffness coefficients* and the deformations become the independent variables or unknowns in the problem. This method of analysis is also denoted as the *displacement (or stiffness) approach*; the methods of slope deflection and moment distribution are classified as displacement methods.

In the further work, the force (or flexibility) method of consistent deformation is used to evaluate the deflection of the micro thermal actuators when heated up. In applying this method, the degree of indeterminacy of the structure or the number of redundants, which are the forces more than the minimum necessary for the static

equilibrium of the structure, must be recognized. The outline of the method is as follows:

1. Reduce the structure to a condition of determinacy and stability by removing the redundants. The resulting structure is called the primary structure (Figure 3.5a and b, where R_2 is removed).

2. Determine the resulting errors in geometry incurred by subjecting the primary structure to loads on the original indeterminate structure (Figure 3.5c, the displacement Δ_2 is the error in geometry).

3. Apply the redundants to the primary structure and determine their effects on the displacements where the geometry has to be corrected (R_2 is the redundant applied as shown in Figure 3.5e).

4. Determine the redundants to eliminate the original errors in geometry (by equating Δ_2 to $R_2\delta_2$, Figure 3.5c and e).

5. Obtain the final forces by adding the redundant forces to the corresponding forces of the primary structure.
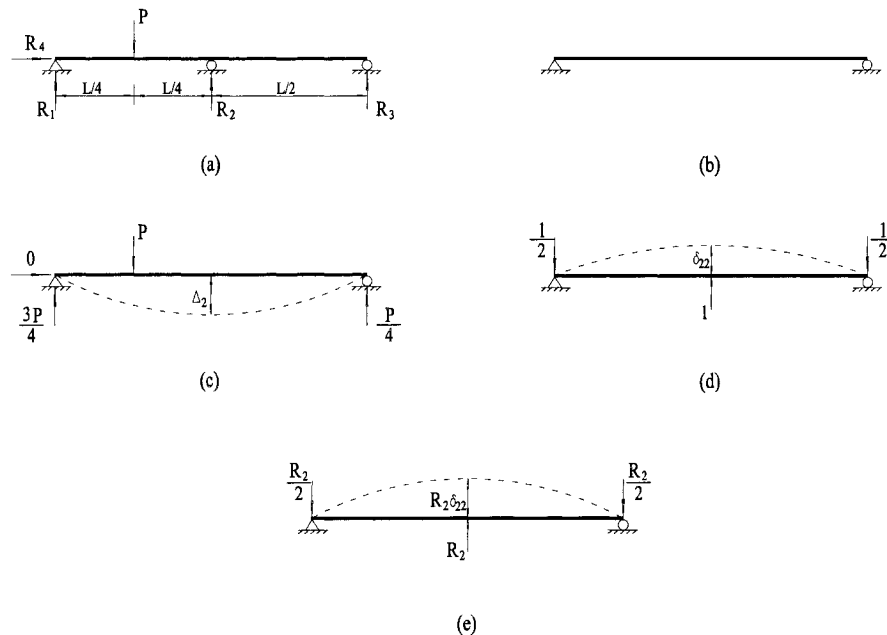
Figure 3.5 Determination of a redundant reaction by the method of consistent deformation

51

This method can be used to analyze any indeterminate structure by solving a set of simultaneous equations of the type:

$$
\begin{aligned}
f_{11}x_1 + f_{12}x_2 + \cdots + f_{1n}x_n &= \Delta_1 \\
f_{21}x_1 + f_{22}x_2 + \cdots + f_{2n}x_n &= \Delta_2 \\
&\;\;\vdots \\
f_{n1}x_1 + f_{n2}x_2 + \cdots + f_{nn}x_n &= \Delta_n
\end{aligned}
\tag{3.7}
$$

Or in matrix expression:

$$
\begin{bmatrix}
f_{11} & f_{12} & \cdots & f_{1n} \\
f_{21} & f_{22} & \cdots & f_{2n} \\
\vdots & \vdots & \cdots & \vdots \\
f_{n1} & f_{n2} & \cdots & f_{nn}
\end{bmatrix}
\begin{Bmatrix}
x_1 \\
x_2 \\
\vdots \\
x_n
\end{Bmatrix}
=
\begin{Bmatrix}
\Delta_1 \\
\Delta_2 \\
\vdots \\
\Delta_n
\end{Bmatrix}
\tag{3.8}
$$

Here, f_{ij} represent flexibility coefficients (i.e., displacements due to unit force or rotations due to unit moment); x_i represents the required correction force or moment; Δ_i represent the errors in geometry (i.e., either displacements or rotations), $i=1,2, \ldots,$ n.

3.1.4 Deflection of the Thermal Actuators
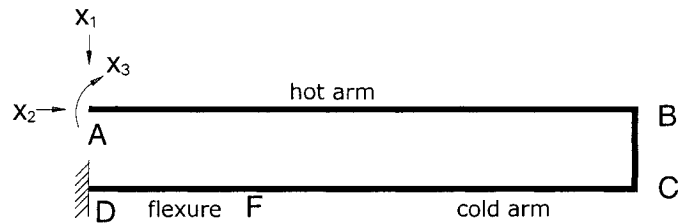
Figure 3.6: The simplified thermal actuator with three redundant force or moment as a rigid frame

The U-shaped thermal actuators studied in this work are similar to a plane rigid frame with two fixed ends as the ones encountered in structural engineering. The force method for the structural engineering is first used here to analyze the bending moment of the actuator structure due to the three redundant force or moment x_1, x_2, x_3, as shown in Figure 3.6. The integration is performed along the middle axis of the hot arm and the flexure along the contour of the frame. The analyses follow the steps as:

1. Reduce the structure to a condition of determinacy by removing the redundants at point A.

2. Determine the resulting errors in the structure incurred by asymmetric thermal expansion. As the redundants are removed, the frame will be free to move along any of the three directions of x_1, x_2, x_3. However, due to the freedom of the end A, the thermal expansion will occur along the x_2 direction because of the difference of thermal expansion between the hot arm, the cold arm and the flexure, and along the x_1 direction because of the thermal expansion of the gap as described by:

53

$$\begin{Bmatrix} \Delta_1 \\ \Delta_2 \\ \Delta_3 \end{Bmatrix} = \begin{Bmatrix} \Delta g \\ \Delta L_h - \Delta L_c - \Delta L_f \\ 0 \end{Bmatrix}$$

where $\Delta_1, \Delta_2, \Delta_3$ represent the resulting errors at A along x_1, x_2, x_3 directions, and $\Delta L_h, \Delta L_c, \Delta L_f$, and Δg are the thermal expansion of the hot arm, the cold arm, the flexure and the gap, respectively.

3. Apply the redundants to the structure. Individual unit forces/moments are applied along the directions of redundants. This assumption evaluates the compliance of the structure due to unit forces/moments acting independently.

4. Determine the redundant force or moment by eliminating the displacement errors. Since A is fixed in original, the equation (3.8) becomes:

$$\begin{bmatrix} f_{11} & f_{12} & f_{13} \\ f_{21} & f_{22} & f_{23} \\ f_{31} & f_{32} & f_{33} \end{bmatrix} \begin{Bmatrix} x_1 \\ x_2 \\ x_3 \end{Bmatrix} = \begin{Bmatrix} \Delta g \\ \Delta L_h - \Delta L_c - \Delta L_f \\ 0 \end{Bmatrix} \tag{3.9}$$

To find the flexibility coefficients matrix, caused by unit forces at each position, the virtual-work expression $\int\limits_{frame} \dfrac{Mm}{EI} dx$ (3.5, 3.6) can be applied as:

$$\int\limits_{frame} \frac{Mm}{EI} dx = \int\limits_{A}^{B} \frac{Mm}{EI} dx + \int\limits_{B}^{C} \frac{Mm}{EI} dx + \int\limits_{C}^{D} \frac{Mm}{EI} dx \tag{3.10}$$

where m represents the internal virtual member due to a unit external virtual force applied to the structure at the point where the displacement is required, and $(M \, dx/EI)$ represents the internal real displacement (rotation) in a bent member due to the external real moment M. Here x is along the contour of the structure.
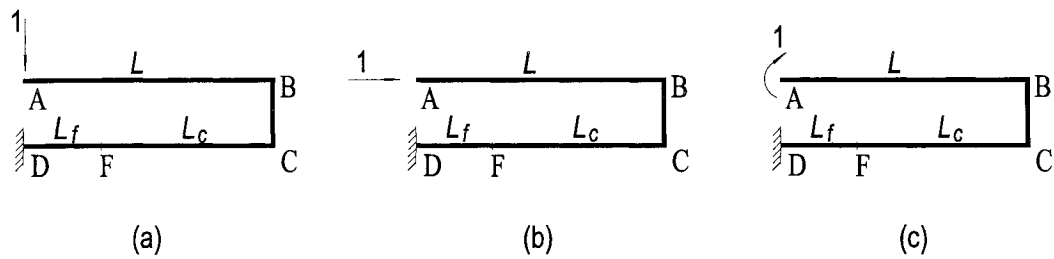
Figure 3.7: The micro thermal actuator (in Figure 3.6) under unit forces and unit

moment

Table 3.2 shows the expressions for m_1, m_2, m_3, where m_1 from (3.10) denotes the moment due to a unit force along x_1 direction at A (Figure 3.7a), m_2 that due to a unit force along x_2 direction at A (Figure 3.7b), and m_3 that due to a unit moment along x_3 direction at A (Figure 3.7c) respectively. L, L_c, L_f represent the length of the hot arm, the cold arm, and the flexure respectively. Here the bending moment in the clockwise direction is considered positive.

Table 3.2 Moments on each beam under unit forces and moment

Member	Origin	Limits	m_1	m_2	m_3
AB	A	$0 - L$	$-x$	0	1
BC	B	$0 - g$	$-L$	x	1
CF	C	$0 - L_c$	$x - L$	g	1
FD	C	$L_c - L$	$x - L$	g	1

f_{11}, f_{21}, f_{31} are the flexibility coefficients which are the displacements in x_1, x_2, x_3 directions caused by unit force along x_1 direction. Therefore $M = m_1$ in this case.

$$f_{11} = \int\limits_{frame} \frac{(m_1)^2}{EI} dx \qquad f_{21} = \int\limits_{frame} \frac{m_1 m_2}{EI} dx \qquad f_{31} = \int\limits_{frame} \frac{m_1 m_3}{EI} dx$$

Similarly, for $f_{12}, f_{22}, f_{32} \quad M = m_2$:

$$f_{12} = \int\limits_{frame} \frac{m_1 m_2}{EI} dx \qquad f_{22} = \int\limits_{frame} \frac{(m_2)^2}{EI} dx \qquad f_{32} = \int\limits_{frame} \frac{m_2 m_3}{EI} dx$$

Also, for $f_{13}, f_{23}, f_{33}, M = m_3$:

$$f_{13} = \int\limits_{frame} \frac{m_1 m_3}{EI} dx \qquad f_{23} = \int\limits_{frame} \frac{m_2 m_3}{EI} dx \qquad f_{33} = \int\limits_{frame} \frac{(m_3)^2}{EI} dx$$

Here, m_1, m_2, m_3, are different in different segments. Using (3.10) and the results in Table 3.2, the flexibility coefficients are expressed as:

$$f_{11} = \int\limits_A^B \frac{(m_1)^2}{EI_h} dx + \int\limits_B^C \frac{(m_1)^2}{EI_g} dx + \int\limits_C^F \frac{(m_1)^2}{EI_c} dx + \int\limits_F^D \frac{(m_1)^2}{EI_f} dx$$

$$= \int\limits_0^L \frac{x^2}{EI_h} dx + \int\limits_0^g \frac{L^2}{EI_g} dx + \int\limits_0^{L_c} \frac{(x-L)^2}{EI_c} dx + \int\limits_{L_c}^L \frac{(x-L)^2}{EI_f} dx \qquad (3.11)$$

$$= \frac{L^3}{3EI_h} + \frac{L^2 g}{EI_g} + \frac{1}{EI_c}\left(\frac{L_c^3}{3} - L_c^2 L + L^2 L_c\right) + \frac{1}{EI_f}\left(\frac{L^3}{3} - \frac{L_c^3}{3} + L_c^2 L - L^2 L_c\right)$$

$$f_{12} = f_{21} = \int_A^B \frac{m_1 m_2}{EI_h} dx + \int_B^C \frac{m_1 m_2}{EI_g} dx + \int_C^F \frac{m_1 m_2}{EI_c} dx + \int_F^D \frac{m_1 m_2}{EI_f} dx$$

$$= \int_0^L \frac{0}{EI_h} dx + \int_0^g \frac{-Lx}{EI_g} dx + \int_0^{L_c} \frac{(x-L)g}{EI_c} dx + \int_{L_c}^L \frac{(x-L)g}{EI_f} dx \qquad (3.12)$$

$$= \frac{1}{EI_g}\left(-\frac{Lg^2}{2}\right) + \frac{1}{EI_c}\left(\frac{L_c^2 g}{2} - LgL_c\right) + \frac{1}{EI_f}\left(-\frac{L^2 g}{2} - \frac{L_c^2 g}{2} + LL_c g\right)$$

$$f_{13} = f_{31} = \int_A^B \frac{m_1 m_3}{EI_h} dx + \int_B^C \frac{m_1 m_3}{EI_g} dx + \int_C^F \frac{m_1 m_3}{EI_c} dx + \int_F^D \frac{m_1 m_3}{EI_f} dx$$

$$= \int_0^L \frac{-x}{EI_h} dx + \int_0^g \frac{-L}{EI_g} dx + \int_0^{L_c} \frac{x-L}{EI_c} dx + \int_{L_c}^L \frac{x-L}{EI_f} \qquad (3.13)$$

$$= \frac{1}{EI_h}\left(-\frac{L^2}{2}\right) + \frac{1}{EI_c}\left(\frac{L_c^2}{2} - LL_c\right) + \frac{1}{EI_g}(-gL) + \frac{1}{EI_f}\left(-\frac{L^2}{2} - \frac{L_c^2}{2} + LL_c\right)$$

$$f_{22} = \int_A^B \frac{(m_2)^2}{EI_h} dx + \int_B^C \frac{(m_2)^2}{EI_g} dx + \int_C^F \frac{(m_2)^2}{EI_c} dx + \int_F^D \frac{(m_2)^2}{EI_f}$$

$$= \int_0^L \frac{0}{EI_h} dx + \int_0^g \frac{x^2}{EI_g} dx + \int_0^{L_c} \frac{g^2}{EI_c} dx + \int_{L_c}^L \frac{g^2}{EI_f} dx \qquad (3.14)$$

$$= \frac{g^3}{3EI_g} + \frac{g^2 L_c}{EI_c} + \frac{g^2(L-L_c)}{EI_f}$$

$$f_{23} = f_{32} = \int_A^B \frac{m_2 m_3}{EI_h} + \int_B^C \frac{m_2 m_3}{EI_g} dx + \int_C^F \frac{m_2 m_3}{EI_c} dx + \int_F^D \frac{m_2 m_3}{EI_f} dx$$

$$= \int_0^L \frac{0}{EI_h} dx + \int_0^g \frac{x}{EI_g} dx + \int_0^{L_c} \frac{g}{EI_c} dx + \int_{L_c}^L \frac{g}{EI_f} dx \qquad (3.15)$$

$$= \frac{1}{EI_g}\left(\frac{g^2}{2}\right) + \frac{1}{EI_c}(gL_c) + \frac{1}{EI_f}(gL - gL_c)$$

$$f_{33} = \int_A^B \frac{(m_3)^2}{EI_h} dx + \int_B^C \frac{(m_3)^2}{EI_g} dx + \int_C^F \frac{(m_3)^2}{EI_c} dx + \int_F^D \frac{(m_3)^2}{EI_f} dx$$

$$= \int_0^L \frac{1}{EI_h} dx + \int_0^g \frac{1}{EI_g} dx + \int_0^{L_c} \frac{1}{EI_c} dx + \int_{L_c}^L \frac{1}{EI_f} dx \qquad (3.16)$$

$$= \frac{L}{EI_h} + \frac{L_c}{EI_c} + \frac{g}{EI_g} + \frac{L - L_c}{EI_f}$$

where E is the Young's modulus of elasticity for polysilicon, and I is the bending moment of inertia for each individual section.

$$I_h = h \cdot W_h^3 / 12$$

$$I_f = h \cdot W_f^3 / 12$$

$$I_c = h \cdot W_c^3 / 12$$

$$I_g = h \cdot W_g^3 / 12$$

The expansions of each section assuming in average temperature on each segment are given by:

$$\Delta L_h = \alpha \cdot L \cdot (\overline{T_h} - T_s)$$

$$\Delta L_c = \alpha \cdot L_c \cdot (\overline{T_c} - T_s)$$

$$\Delta L_f = \alpha \cdot L_f \cdot (\overline{T_f} - T_s)$$

$$\Delta g = \alpha \cdot g \cdot (\overline{T_c} - T_s)$$

58

The three redundant force or moment x_1, x_2, x_3, can be further obtained by solving the simultaneous equations of (3.9). The numeric relation for the benchmark actuator are presented in Table 3.5. The units for x_1, x_2, x_3 are N, N, Nm respectively. Here, positive means that the direction is the same as it has been assumed.

Now, analyze the hot arm separately. The three redundants that represent the forces/moments developed in the clamping point A will apply the hot beam and create a moment distribution as the one illustrated in Figure 3.8(a), which represents the loading due to the thermal load. In order to obtain the deflection at the tip, assuming a virtual force P* of unit amplitude, the bending moment diagram in the hot beam will look as illustrated in Figure 3.8(b).

(a)

(b)
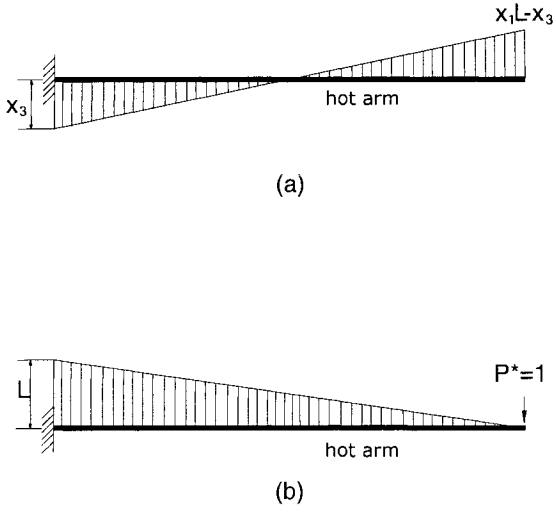
Figure 3.8: (a) the bending moment of the hot arm due to the thermal expansion of the structure (b) the bending moment of the hot arm due to the virtual force

Further, if applying the method of virtual work, the maximum deflection at the free end of the actuator can be expressed by (3.5) as:

$$d = \frac{\int \overline{M} M}{EI_h} dx$$

Here M is the bending moment due to the thermal expansion, $\overline{M}$ represents the bending moment due to the unit virtual force.

$$M = x_1 x - x_3$$

$$\overline{M} = L - x$$

Therefore, we obtain:

$$d = \int \frac{\overline{M} M}{EI_h} dx = \int_0^L \frac{(L-x)(x_1 x - x_3)}{EI_h} dx = \frac{L^2}{6EI_h}(x_1 L - 3x_3) \qquad (3.17)$$

Table 3.3 Deflections from beam expansion method, virtual work method, FEM (ANSYS), and experimental results

U (V)	Exp. deflection (μm)	Beam expansion method (μm)	Difference compared with exp. result (%)	Virtual work method (μm)	Difference compared with exp. result (%)	FEM (ANSYS) (μm)
5	Not observed	3.3	---	5.9	---	5.13
10	23	11.37	50.6	20	13	18.991
15	40	21.93	45.2	38.8	3	38.599
20	55	33.28	39.5	58.9	7	61.596

The numerical results for various voltages applied at the pads of the actuator are presented in Table 3.3. It has been proved that the virtual work method yield significantly more accurate results versus the experimental measurement in comparison with the beam expansion method.

Compared with the beam expansion method, which yields results within about 50% difference from the experimental results, the virtual work and force (or flexibility) method of consistent deformation offer a more accurate way to evaluate the deflection of the micro thermal actuator, the difference from the experimental results less than 13%. Moreover the Finite Element Method is in good agreement with the results from the virtual work method.
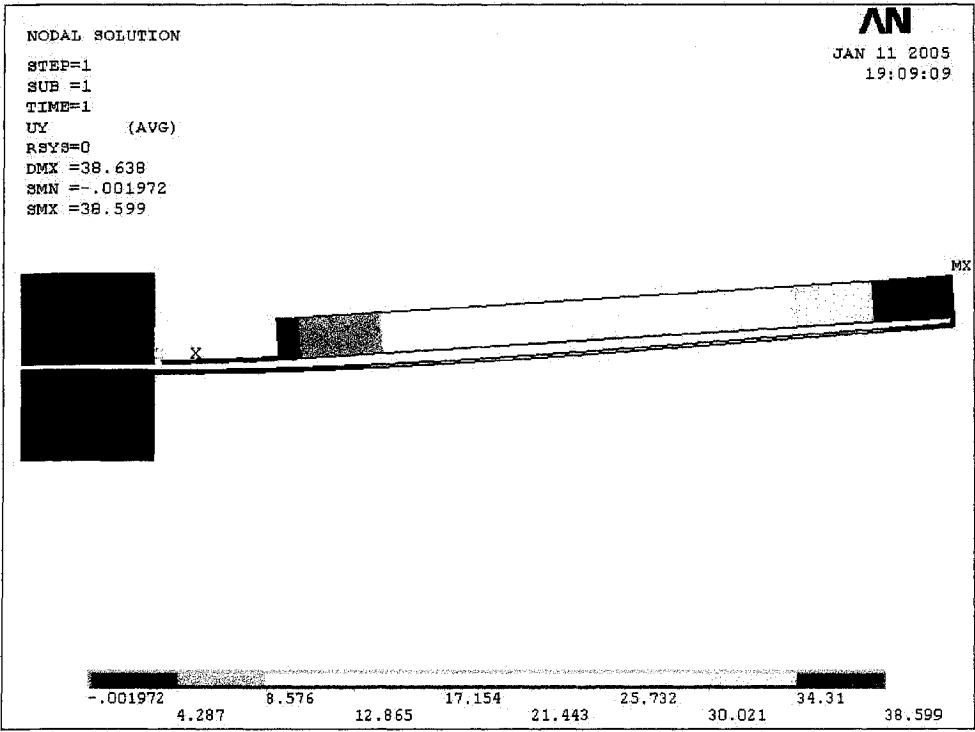
Figure 3.9: FEM result of displacement along the structure (μm) (under 15V)

3.2 Natural Frequency Analysis

3.2.1 Rayleigh's Method

The fundamental frequency of microactuators is of great interest due to the great potential deformation at the natural frequency. The Rayleigh's method, which is an energy method, can yield a good estimate of the fundamental frequency of systems that consist of flexible elements such as springs and beams.

The Rayleigh' principle states that energy remains constant in a conservative system. For a system which is undergoing harmonic motion, the kinetic energy changes into potential energy and back continuously, so that under steady state conditions:

$$T_{max} = U_{max}$$

$$\text{or} \quad \omega^2 T_{max}^* = U_{max}$$

This leads directly to the natural frequency.

$$f = \frac{1}{2\pi} \sqrt{\frac{U_{max}}{T_{max}^*}}$$

Under harmonic excitation, the movement of the arms of the thermal actuator can be considered as harmonic.

The potential energy is determined as the work done under the static loading in the assumed deformation. This work is, stored in the flexible member as strain energy. For beams, the elastic strain energy can be calculated in terms of its flexural rigidity

EI. By letting M be the bending moment and θ the slope of the elastic curve, the strain energy stored in an infinitesimal beam element is:

$$dU = \frac{1}{2} M d\theta$$

Because the deflection in beams is generally small, geometric relations are assumed (as shown in Figure 3.1) as:

$$\frac{d\theta}{dx} = \frac{d^2 y}{dx^2} = \frac{1}{\rho}$$

where ρ is the radius of curvature. In addition, from the theory of beams, the flexure equation is:

$$\frac{1}{\rho} = \frac{M}{EI}$$

By substituting for $d\theta$ and $1/\rho$, for beams, the elastic strain energy can be calculated by:

$$U_{max} = \frac{1}{2} \int \frac{M^2}{EI} dx = \frac{1}{2} \int EI \left(\frac{d^2 y}{dx^2} \right)^2 dx \qquad (3.18)$$

where the integration is carried out over the entire beam.

The kinetic energy:

$$T_{max} = \frac{1}{2} \int \dot{y}^2 dm = \frac{1}{2} \omega_n^2 \int m(x) y^2 dx \qquad (3.19)$$

where y is the assumed deflection curve, $m = mass/length$ --mass per unit of length, and the integration is carried out over the entire beam.

Thus the fundamental frequency of the beam is expressed as:

$$\omega_n^2 = \frac{\int EI\left(\frac{d^2y}{dx^2}\right)^2 dx}{\int y^2 m(x)dx}$$

(3.20)

3.2.2 Rayleigh-Ritz Method

3.2.2.1 General

W. Ritz developed a method that is an extension of Rayleigh's method. It not only provides a means of obtaining a more accurate value for the fundamental frequency, but it also gives approximations to the higher frequencies and mode shapes.

The Ritz method is essentially the Rayleigh method based on the conservation of energy in undamped structures undergoing vibration, however, the single shape function is replaced by a series of shape functions Φ_i multiplied by constant coefficients C_i. The coefficients are adjusted by minimizing the frequency with respect to each of the coefficients which results in n algebraic equations in ω^2. The solution of these equations then gives the natural frequencies and mode shapes of the system.

$$W(x) = \sum_{i=1}^{N} C_i \Phi_i(x)$$

(3.21)

where $\Phi_i(x)$ are any admissible functions satisfying at least the geometric boundary conditions and C_i are arbitrary constant coefficients. For a conservative system, the maximum kinetic energy in the system undergoing vibration is equal to the maximum

strain energy. However since the assumed shape is not exact, the kinetic energy T_{max} will not be equal to strain energy U_{max}, and hence the error can be taken as

$$F(C_i,\omega) = U_{max} - T_{max}$$

The coefficients C_i must be chosen so as to minimize the error and hence

$$\frac{dF}{dC_i} = \frac{d}{dC_i}(U_{max} - T_{max}) = 0$$

$$\frac{\partial U_{max}}{\partial C_i} - \left(\omega^2 \frac{\partial T^*_{max}}{\partial C_i} + T^*_{max} \frac{\partial \omega^2}{\partial C_i} \right) = 0$$

where

$$T_{max} = \omega^2 T^*_{max}$$

Since ω^2 must be stationary with respect to C_i, we have $\dfrac{\partial \omega^2}{\partial C_i} = 0$, which gives

$$\frac{\partial U_{max}(C_i)}{\partial C_i} - \omega^2 \frac{\partial T^*_{max}(C_i)}{\partial C_i} = 0$$

and it can also be written as:

$$[K]\{C_i\} - \omega^2[M]\{C_i\} = 0 \qquad\qquad (3.22)$$

where
$$[M] = \frac{\partial T^*_{max}}{\partial C_i} = \text{Mass Matrix}$$

$$[K] = \frac{\partial U_{max}}{\partial C_i} = \text{Stiffness Matrix} \qquad i=1,2,\ldots,n$$

This is a standard eigenvalue problem and the solution yields the natural frequencies and the corresponding coefficients can be used to obtain the approximate mode shapes.

3.2.2.2 Generation of Single Variable Orthogonal Polynomial

The Rayleigh-Ritz method requires using shape functions satisfying at least the geometrical boundary conditions. These shape functions when substituted in kinetic and potential terms might produce cross terms in the mass and stiffness matrices. The matrices become ill conditioned and pose numerical problem in solving for eigenvalues when more number of these terms are considered.

To overcome this problem, a set of orthogonal polynomials by using Gram-Schmidt process was proposed by Bhat [28, 29] in Rayleigh-Ritz method as admissible function for dynamic and static problems of beams, rectangular plates with classical boundary condition. Rinaldi et al [30] investigated the dynamic and static behaviors of the MEMS cantilever beams by the Rayleigh-Ritz energy method using boundary characteristic orthogonal polynomials under non-classical conditions.

Given the polynomial of the lowest order satisfying at least the geometrical boundary conditions of the beam, $\Phi_0(x)$, an orthogonal set of polynomials in the interval $0 \leq x \leq 1$ can be generated using the Gram-Schmidt process as follows:

$$\Phi_1(x) = (x - B_1)\Phi_0(x) \tag{3.23}$$

$$\Phi_k(x) = (x - B_k)\Phi_{k-1}(x) - C_k\Phi_{k-2}(x) \tag{3.24}$$

where

$$B_k = \frac{\int_0^1 x\rho(x)\Phi_{k-1}^2(x)dx}{\int_0^1 \rho(x)\Phi_{k-1}^2(x)dx} \tag{3.25}$$

$$C_k = \frac{\int_0^1 x\rho(x)\Phi_{k-1}(x)\Phi_{k-2}(x)dx}{\int_0^1 \rho(x)\Phi_{k-2}^2(x)dx} \qquad (3.26)$$

where $\rho(x)$ is a weighting function and is taken as unity for a uniform beam. The interval is from 0 to 1 and the coefficients are chosen in such a way as to make the polynomials orthonormal,

$$\int_0^1 \Phi_k(x)\Phi_l(x)dx = 0 \qquad \text{if } k{\neq}l \qquad (3.27)$$

$$=1 \qquad \text{if } k{=}l$$

Even though $\Phi_0(x)$ satisfies all the boundary conditions, the other members of the orthogonal set satisfy only the geometrical boundary conditions, which can be seen from Equations (3.23) and (3.24).

Here, the whole thermal actuator is considered as a beam, with one end clamped. The actual co-ordinate ξ is non-dimensionalized as $x = \xi/l$, and consequently, the boundary conditions are:

$$W(0) = W'(0) = W''(1) = W'''(1) = 0 \qquad (3.28)$$

along x directions from the clamped edge to the free edge. Hence, the first member of the polynomial set, $\Phi_0(x)$, must satisfy all the above boundary conditions. Assuming the beam deflection function as the simplest forth power polynomial:

$$W(x) = a_0 + a_1 x + a_2 x^2 + a_3 x^3 + a_4 x^4 \qquad (3.29)$$

67

Imposing the boundary conditions to Equation (3.29), one obtains the deflection shape function as

$$W(x) = a_4 \left(6x^2 - 4x^3 + x^4\right) \tag{3.30}$$

where a_4 is an arbitrary constant. The normalized mode function can be expressed as

$$\Phi_0(x) = \frac{\left(6x^2 - 4x^3 + x^4\right)}{\left(\int_0^1 \left(6x^2 - 4x^3 + x^4\right)^2 dx\right)^{1/2}} \tag{3.31}$$

For the beam, the kinetic energy and the strain energy in (3.18, 3.19) are:

$$T_{max} = \frac{\omega^2 l}{2} \int_0^1 m(x) W^2(x) dx$$

$$U_{max} = \frac{E}{2l^3} \int_0^1 I(x) \left(\frac{d^2 W(x)}{dx^2}\right)^2 dx$$

For the equation (3.22), the m_{ij} in Mass Matrix $[M]$ and the k_{ij} in Stiffness Matrix $[K]$ for the thermal actuator in the above configuration is (show in Figure 2.2):

$$m_{ij} = m_h L \int_0^1 \Phi_i(x) \Phi_j(x) dx + m_f L \int_0^{L_f/L} \Phi_i(x) \Phi_j(x) dx + m_c L \int_{L_f/L}^1 \Phi_i(x) \Phi_j(x) dx \tag{3.32}$$

where, the mass per length in the hot arm beam, the cold arm beam and the flexure arm beam are

$$m_h = \frac{\rho V_h}{L} \qquad m_f = \frac{\rho V_f}{L_f} \qquad m_c = \frac{\rho V_c}{L_c}$$
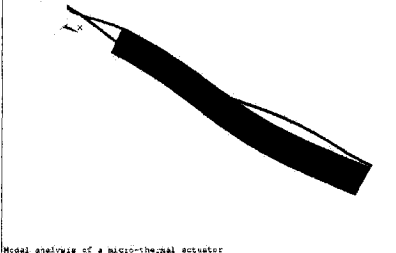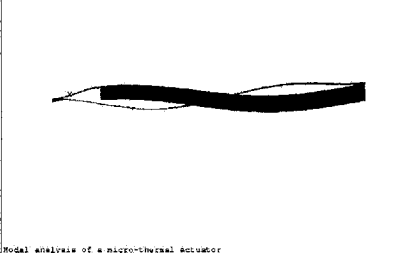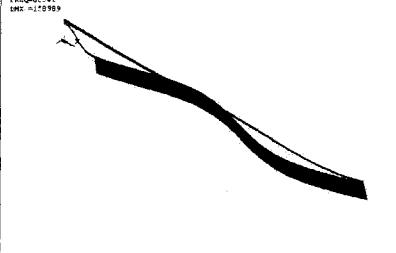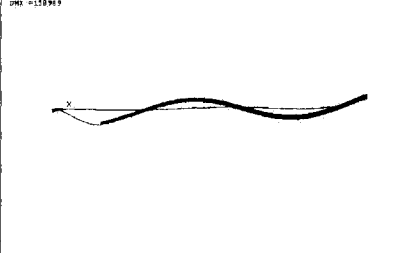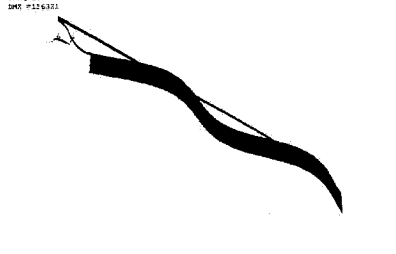
68
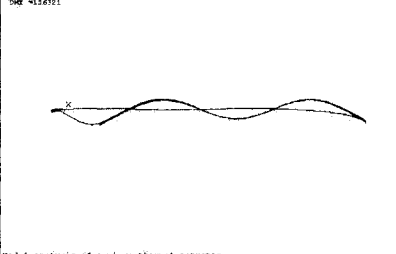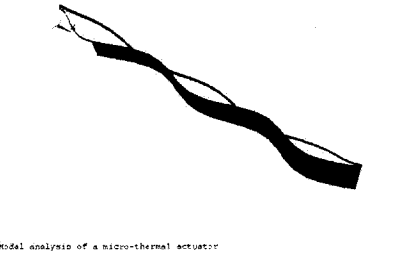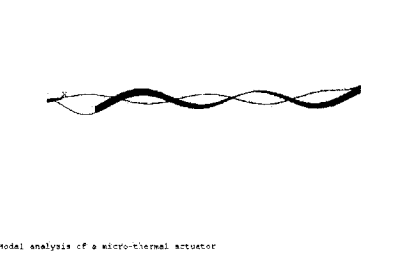
$$k_{ij} = \frac{EI_1}{L^3} \int\limits_{0}^{L_f/L} \frac{d^2\Phi_i(x)}{dx^2} \frac{d^2\Phi_j(x)}{dx^2} dx + \frac{EI_2}{L^3} \int\limits_{L_f/L}^{1} \frac{d^2\Phi_i(x)}{dx^2} \frac{d^2\Phi_j(x)}{dx^2} dx \qquad (3.33)$$

where the cross section moment of inertia I_1 and I_2 are expressed for the range of flexure with part of the hot arm (from 0 to L_f), and the range of cold arm with part of the hot arm (from L_f to L) respectively. Since the lower frequency will be in a direction along the thickness h of the sensor, we have

$$I_1 = \frac{(W_h + g + W_f)h^3}{12} \qquad\qquad I_2 = \frac{(W_h + g + W_c)h^3}{12}$$

Table 3.4 Natural frequencies by Rayleigh–Ritz method and by FEM (ANSYS) simulation

Mode	Rayleigh –Ritz (KHz)	FEM (ANSYS) (KHz)	Pictures	
			Isometric view	**Top view**
1	1.454	1.432		
2	15.729	14.377		

3	47.533	46.784		
4	96.097	88.546		
5	164.846	157.60		
6	256.126	252.31		

Results show that the analytical evaluation of the natural frequency and the first five harmonics are is in good agreement with the FEM simulation.

3.3 The Stiffness of the Structure:

If the whole thermal actuator is looked as one elastic beam, as shown in Figure 3.1, the stiffness K_s can be described as:

$$K_s = \frac{3EI}{L^3} \tag{3.34}$$

From the experiments, one can see that the hot arm and the flexure are significantly bent during the stroke, while the cold arm looks almost rigid. Therefore, here, the moment of inertia I of the whole structure could be calculated according to the cross section at the flexure zone, only while the length of the structure will be given by the length of the hot arm.

So
$$I = \frac{h\left(W_h + g + W_f\right)^3}{12} - \frac{hg^3}{12} \tag{3.35}$$

3.4 The Force Generated at the Tip

The force generated at the tip is an important feature of the thermal actuators, especially for those that are used to push or drive other parts in a micro system. As a voltage is applied to the pads of the thermal actuator, a deflection will appear at its free end. The grasp force at the tip will be equal to zero every instant the motion will be unconstrained. Force could be generated by the thermal actuator only if the free motion of the tip is constrained. The maximum force would be achieved then if the tip

is fully constrained at the equilibrium position, while the applied voltage is the maximum.

To calculate the force generated at the tip, Hooke' law is generally used as the structure of the U-shaped thermal actuator is an elastic system. Here, it is assumed that the vertical deflection at the tip, which is only the result of a force applied at tip, has the same effect as that caused by asymmetric thermal expansion.

The forces generated at the tip can be expressed as:

$$F = K_s(d - y) \tag{3.36}$$

where, y is the deflection at the tip. When the thermal actuator is activated and bends up to the largest deflection, the force turns to zero, and the maximum force generated when the structure just begins to move is:

$$F_{max} = K_s \cdot d \tag{3.37}$$

where d can be obtained from (3.17).

To verify the results from (3.37), using FEM model (ANSYS), the forces F_{max} are applied on the tip of the benchmark thermal actuator model. The deflections d' at the tip are in good agreement with the deflections resulting from the virtual work method d (3.17), the results from FEM (ANSYS) under thermal-electrical effect $d*$, and those measured in experiment d_e (as from Chapter 4).

Table 3.5 The equivalent force generated at the tip

Voltage(V)	5	10	15	20
$d(m)$ (3.17) (virtual work method)	5.92e-6	20e-6	38.8e-6	58.9e-6
$K_s(N/m)$ (3.34)	0.193			
$F_{max}(N)$	1.14e-6	3.89e-6	7.49e-6	1.14e-5
$d'(m)$ (FEM) (force effect)	6.16e-6	21.8e-6	42.2 e-6	63.8e-6
$d*(m)$ (FEM) (thermal-electrical effect)	5.13e-6	18.991e-6	38.599e-6	61.596e-6
$d_e(m)$ (experimental)	0	23e-6	40e-6	55e-6


```
NODAL SOLUTION                                    AN
STEP=1                                    APR 21 2005
SUB =1                                       14:48:20
TIME=1
UY
RSYS=0
DMX =21.791
SMN =-.002972
SMX =21.761
```

```
 -.002972      4.834       9.67       14.506       19.343
        2.415       7.252      12.088       16.925      21.761
```
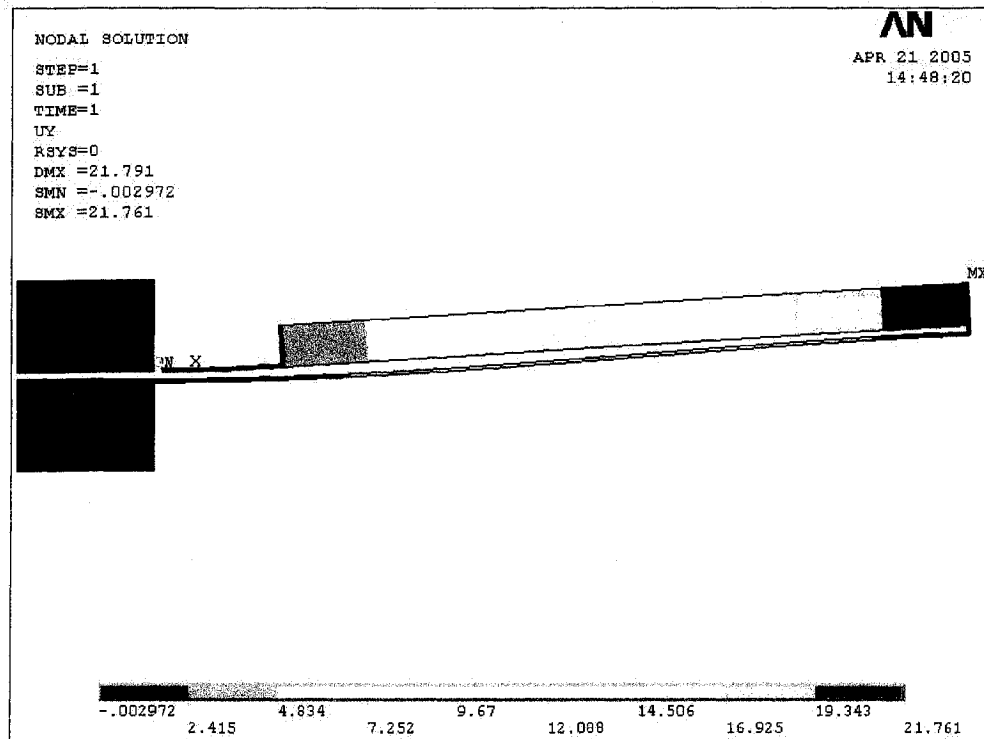
Figure 3.10: Applying F_{max}=3.89e-6N at the tip of the structure, the deflection d'=21.761μm

73

3.5 Stress Analysis

Stress analysis is performed to ensure the structure's integrity under static loading. Here, we consider that there are two kinds of stress on thermal actuators, the first one is bending stress caused by bending moment on beams, and the second is due to the axial tension or compression caused by the axial forces.

The *bending stress* σ_b can be calculated as:

$$\sigma_b = \frac{M(x)}{\frac{1}{6}hW^2}$$

The *axial stress* σ_t can be calculated as:

$$\sigma_t = \frac{P}{Wh}$$

where P is axial force.

The equivalent bending moment and axial forces on each beam of the thermal actuator can be obtained from 3.1.4 as the forces and the moment x_1, x_2, x_3 applied at point A. The bending moment diagram is shown in Figure 3.11:

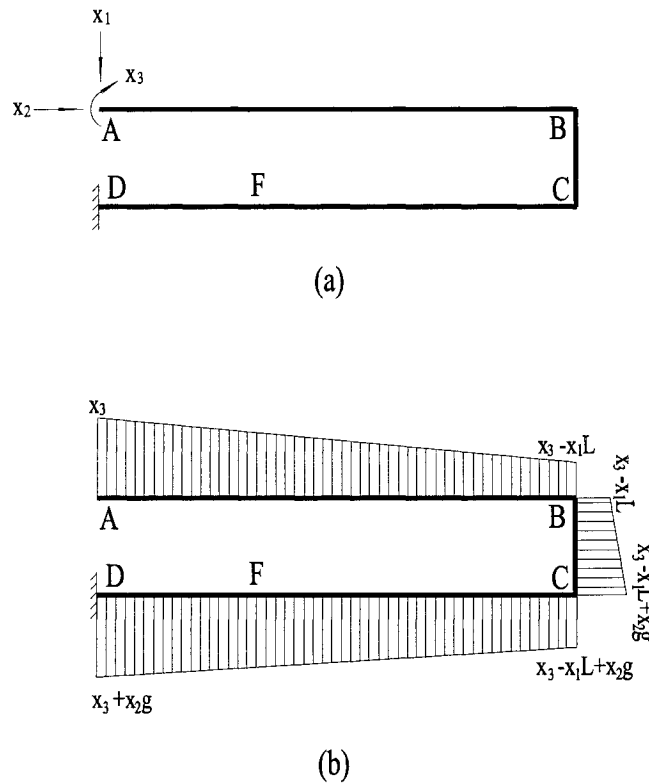Figure 3.11: (a) the equivalent forces and moment applied on the thermal actuator

(b) diagram of the bending moments on the beams

For bending stress, the inner fibers are in compression and the outer fibers are in tension; and for axial stress, they are in tension or compression. Therefore, the possible maximum combined stresses, considering the bending stress and the axial stress together, can be expressed as:

From A to B:

$$M = x_3 - x_1 x \quad (0 \le x \le L)$$

$$P = x_2$$

$$\sigma_{AB} = \left| \frac{6M}{hW_h^2} \right| + \left| \frac{x_2}{hW_h} \right| \qquad (3.38)$$

From B to C:

$$M = x_2 x + x_3 - x_1 L \quad (0 \le x \le g)$$

$$P = x_1$$

$$\sigma_{BC} = \left| \frac{6M}{hW_g^2} \right| + \left| \frac{x_1}{hW_g} \right| \qquad (3.39)$$

From C to F:

$$M = x_1 x + x_3 - x_1 L + x_2 g \quad (0 \le x \le L_c)$$

$$P = x_2$$

$$\sigma_{CF} = \left| \frac{6M}{hW_c^2} \right| + \left| \frac{x_2}{hW_c} \right| \qquad (3.40)$$

From F to D:

$$M = x_1 x + x_3 - x_1 L + x_2 g \quad (L_c \le x \le L)$$

$$P = x_2$$

$$\sigma_{FD} = \left| \frac{6M}{hW_f^2} \right| + \left| \frac{x_2}{hW_f} \right| \qquad (3.41)$$

Here, the stresses at the two edges of each beam are calculated. For the thermal actuators the same geometries are used as those in Table2.1. The results of stresses analysis under 5V, 10V, 15V, 20V, are listed respectively in Table 3.7:

Table 3.6 Stress analysis

beam	edge	5V(Pa)	10V(Pa)	15V(Pa)	20V(Pa)
$x_1(N)$		-2.82e-8	-9.58e-8	-1.85e-7	-2.8e-7
$x_2(N)$		5.55e-6	1.89e-5	3.64e-5	5.52e-5
$x_3(Nm)$		-1.99e-11	-6.76e-11	-1.3e-10	-1.98e-10
hot arm	A	7.55e6	2.57e7	4.95e7	7.51e7
	B	3.41e6	1.16e7	2.23e7	3.39e7
gap arm	B	2.49e6	0.846e7	1.63e7	2.47e7
	C	**15.44e6**	**5.25e7**	**10.11e7**	**15.35e7**
cold arm	C	0.11e6	0.04e7	0.07e7	0.11e7
	F	0.08e6	0.03e7	0.05e7	0.08e7
flexure	F	8.66e6	2.95e7	5.68e7	8.61e7
	D	7.25e6	2.47e7	4.76e7	7.21e7

From the results, some conclusions are drawn. The most important is that the all stresses on the structure are much lower than the yield strength of polysilicon, $S_Y = 7 \times 10^9 Pa$, so the structure is safe when it moves back and forth. The second one is that, the maximum stress is at the point C on the gap arm, where the cold arm connected.

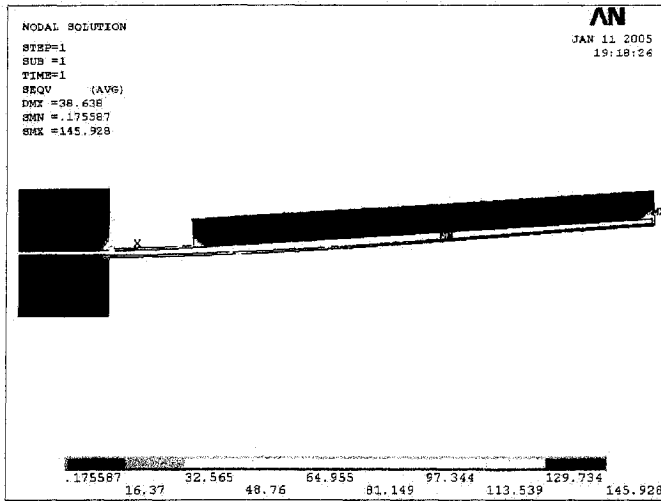Table 3.7 The maximum stress from FEM simulation under two kinds of effect

Voltage	(V)	5	10	15	20
The maximum stress (thermal-electrical effect)	(Pa)	15.9e6	6.01e7	12.22e7	19.5e7
Applied force	(N)	1.14e-6	3.89e-6	7.49e-6	1.14e-5
The maximum stress (force effect)	(Pa)	70.1e6	24.8e7	48e7	72.6e7

The Finite Element Model that solves the stress problem in the thermal actuator could be formulated in multiple ways. Two such formulations have been considered and the results of the analysis are shown in Table 3.8.
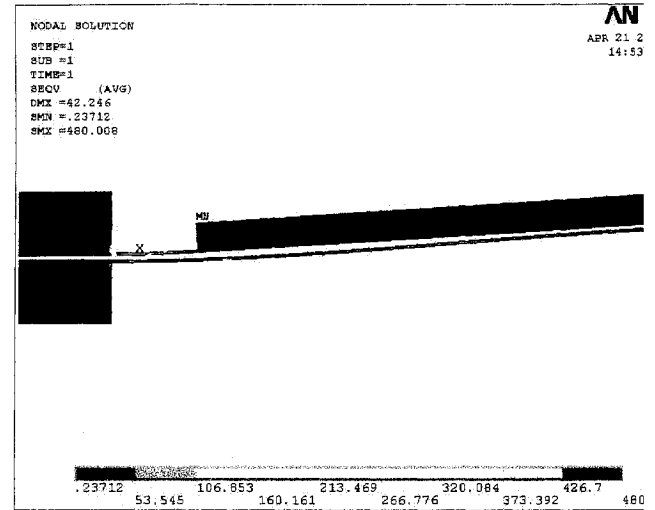
The multi-physics formulation uses the voltage as an input so that the thermal expansion is counted for. The stress distribution in the structure is more reasonable and close to the classical stress calculation.

The force effect formulation assumes that a concentrated force is applied at the free end of the thermal actuator in the direction of motion. The applied force corresponds to the value calculated for 5, 10, 15, and 20V applied input and shown in Table 3.6.

The results of this assumption are much higher than the one resulting from the multi-physics formulation. The discrepancy may be due to the fact that the thermal expansion may release the built up stress. If no expansion is assumed, at the same deflection the structural, stress yields as being overestimated. A direct conclusion is that structures subjected to multi-physics phenomenon should be modeled taking into consideration as many as possible effects or influence.

NODAL SOLUTION		AN

NODAL SOLUTION
STEP=1
SUB =1
TIME=1
SEQV   (AVG)
DMX =38.638
SMN =.175587
SMX =145.928

JAN 11 2005
19:18:26

NODAL SOLUTION
STEP=1
SUB =1
TIME=1
SEQV   (AVG)
DMX =42.246
SMN =.23712
SMX =480.008

APR 21 2
14:53

.175587   32.565   64.955   97.344   129.734
      16.37   48.76   81.149   113.539   145.928

.23712   106.853   213.469   320.084   426.7
      53.545   160.161   266.776   373.392   480

(a)   (b)

Figure 3.12: (a) stress distribution under 15V though coupled–field multiphysics

analysis (thermal-electrical effect)

(b) stress distribution under equivalent force (force effect)

3.6 The Thermal Frequency

The maximum frequency of operation of an actuator is a fundamental performance measure. If the movement at the tip is considered as a half cycle of a harmonic vibration, after it is heated up, one can calculate the thermal frequency as follows:

From the conservation of energy, the duration of the motion is:

$$\Delta t\left[E_g - (Q_V + Q_R)\right] = C_p \cdot M \cdot \Delta T$$

$$\Delta t = \frac{C_p \cdot M \cdot \Delta T}{\left[E_g - Q_V - Q_R\right]} \tag{3.42}$$

where, $\Delta T = T_{av} - 300$ and M is the mass of the structure:

$$M = \rho \cdot V$$

Substituting (2.10) and (2.18) into (3.42), Δt can be expressed as:

$$\Delta t = \frac{(\overline{T_h} - T_s)(L \cdot W_h + g \cdot W_g) + (\overline{T_f} - T_s) \cdot L_f \cdot W_f + (\overline{T_c} - T_s) \cdot L_c \cdot W_c}{\lambda \cdot V \cdot K} \tag{3.43}$$

Replacing $\overline{T_h}, \overline{T_f}, \overline{T_c}$ by (2.15), (2.16), (2.17), λ, which is dependent on voltage, is canceled, and Δt can be expressed as:

$$\Delta t = \frac{[-\dfrac{(L+g)^2}{6} + \dfrac{(L+L_f+g)(L+g)}{4}](L \cdot W_h + g \cdot W_g) + [-\dfrac{L_f^2}{6} + \dfrac{(L+L_f+g)L_f}{4}] \cdot L_f \cdot W_f - \dfrac{L_f \cdot (L+g) \cdot L_c \cdot}{2}}{(L \cdot W_h + L_c \cdot W_c + L_f \cdot W_f + g \cdot W_g)^2 \cdot h \cdot K}$$

(3.44)

The thermal frequency is a function of the geometry of the structure and the thermal conductivity of the material; and is not dependant by the applied voltage. And the thermal frequency of the thermal actuator is:

$$f_t = \frac{1}{2\Delta t} \tag{3.45}$$

$$\omega_t = 2\pi f_t \tag{3.46}$$

For the benchmark actuator, the thermal frequency is calculated as 835.6Hz.

3.7 The Efficiency

The energy applied on this thermal actuator as electric energy is transformed into other kinds of energy. The main effect is Joule heating. Portion of this energy transfers in the structure's deflection, part is dissipated into the environment and the substrate through heat conduction, heat convection, and radiation. At the steady state, no more energy is banked into the structure since no thermal modification occurs.

The efficiency of this thermal actuator can be calculated as follows:

$$\eta = \frac{output\_effective\_energy}{input\_energy} = \frac{\frac{1}{2}K_s \cdot d^2}{\frac{U^2}{R}\Delta t} \tag{3.47}$$

The efficiency considers only the strain energy effect since thermal actuators are mainly used in low speed applications. The kinetic energy term is ignored under the above assumption.

Dissipated heat:

 from convective heat dissipation:

$$\eta_V = \frac{Q_V}{E_g} \tag{3.48}$$

from radiative heat dissipation:

$$\eta_R = \frac{Q_R}{E_g} \tag{3.49}$$

 the balance of heat energy:

$$\eta_B = 1 - \eta - \eta_V - \eta_R \tag{3.50}$$

Under a certain potential, the thermal actuator begins to bend till its free end reaches the maximum deflection and then stops. This duration represents half cycle of the thermal frequency. After the potential is cut, the part of the remaining energy, releases to substrate, and the temperature gradient reduces, hence the deflection caused by asymmetrical heat expansion is lost, and the structure returns to the initial shape. The efficiency of the return motion is same as that of the one when the potential is applied after the thermal gradient becomes uniform; the efficiency drops again to zero. The maximum effectiveness of the actuator could be reached when the actuation is performed at thermal frequency rate.

For the thermal actuators of geometries as in Table 2.1, the results for the benchmark thermal actuator the efficiency of the mechanical actuation and the efficiency of the heat transfer mechanisms are given in Table 3.9 under 5V, 10V, 15V, 20V:

Table 3.8 Efficiencies and thermal frequency of the bench mark thermal actuator

Voltage(V)	5	10	15	20
$f_n(Hz)$ (first mode)	1454			
$f_t(Hz)$	835.6			
$\Delta t(s)$	5.98e-4			
η (mechanical)	5.19e-7	1.75e-6	3.37e-6	5.09e-6
η_V (convection)	0.0759	0.0829	0.0804	0.0809
η_R (radiation)	0.0019	0.0034	0.0056	0.0096
η_B (balance)	0.9222	0.9137	0.9140	0.9094

CHAPTER 4 FABRICATION PROCESS AND EXPERIMENT VALIDATION

4.1 Fabrication

In this thesis, the design of the thermal actuators was accomplished with the L-Edit software program, and the chips were fabricated through CMC (Canadian Microelectronics Corporation) following MUMPs technology by MEMsCAP.

4.1.1 Introduction

For mechanical engineers, a major effort in manufacturing a product is the proper selection and application of fabrication techniques such as machining, drilling, milling, forging, welding, casting, molding, stamping, or peening. Moreover, the basic technology for micromachining MEMS devices is similar as for the integrated circuits: microfabrication allows miniaturization and paralleling processing which leads to inexpensive fabrication in large quantities. None of the traditional fabrication techniques can be used in manufacturing low cost products, large batches, integrated systems and devices.

Generally speaking, there are three distinct micromachining techniques used by current industry to realize micro system. They are (1) bulk micromanufacturing, (2) surface micromachining, and (3) the LIGA process. The term LIGA is an acronym for the German term for lithography, electroforming, and plastic molding.

Bulk micromachining involves removal of significant regions of the substrate (e.g., etching cavities in a silicon substrate) and can thus be thought of as a subtractive process. Surface micromachining involves building up and patterning thin-film

layers to realize the desired structures on the surface of the wafer (an additive and patterning process).

Both micromanufacturing techniques, bulk manufacturing and surface micromachining, involve microfabrication processes evolved from microelectronics technology. Consequently, much of the developed knowledge and experience as well as equipment used for the production of microelectronics and integrated circuits can be adapted for MEMS and Microsystems manufacturing with little process modifications. Unfortunately, these inherited advantages are overshadowed by two major drawbacks: (1) the low geometric aspect ratio, and (2) the use of silicon-based materials. The LIGA process for manufacturing MEMS and Microsystems is radically different from these two manufacturing techniques. This process offers a great potential for manufacturing non-silicon-based microstructures, and the most important feature of this process is that it can produce "thick" microstructures that have extremely flat and parallel surfaces. However, LIGA enables the fabrication of micro-mechanical system only.

4.1.2 MUMPs

The MUMPs (Multi-User MEMS Processes) is a commercial program that provides the international industrial, governmental and academic communities with cost-effective, proof-of-concept surface micromachining fabrication. The U-shaped micro thermal actuators studied in this thesis were designed and fabricated according to this technology.

MUMPs is a three-layer polysilicon surface micromachining process derived from work performed at the Berkeley Sensors and Actuators Center (BSAC) at the

University of California in the late 80's and early 90's. This process has the general features of a standard surface micromachining process:

1. Polysilicon is used as the structural material

2. Deposited oxide (PSG) is used as the sacrificial layer

3. Silicon nitride is used as electrical isolation between the polysilicon and the substrate

4. Metal (usually gold) is the top layer of the device and is used as a conductive layer.
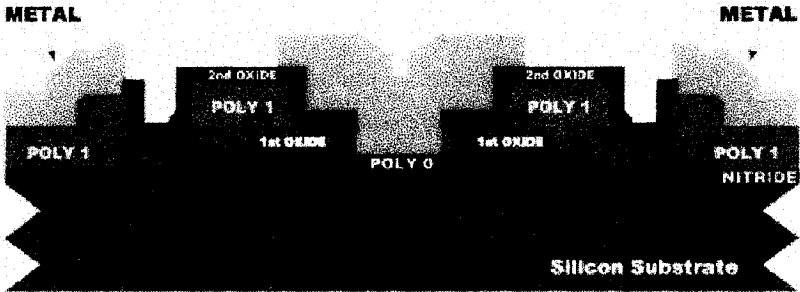
Figure 4.1: Cross section of MEMS device fabricated by MUMPs [26]
(structural layers and sacrificial layers before releasing process)
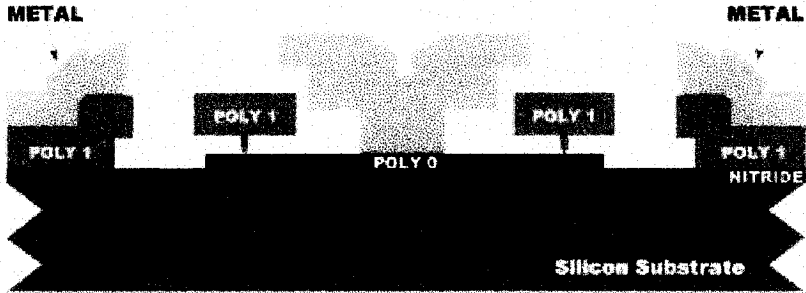
Figure 4.2: Cross section of MEMS device fabricated by MUMPs [26]
(structural layers and sacrificial layers before releasing process)

In order to make the process as general as possible, MUMPs process defines the thicknesses and the functions all the layers. All MEMS designers have to follow these definitions and design rules.

Table 4.1 Layer names, thickness and lithography levels. (MUMPs Handbook, 2002)

Material Layer	Thickness (μm)	Lithography Level Name
Nitride	0.6	-
Poly 0	0.5	POLY0 (HOLE0)
First Oxide	2.0	DIMPLE ANCHOR1
Poly 1	2.0	POLY1 (HOLE1)
Second Oxide	0.75	POLY1_POLY2_VIA ANCHOR2
Poly 2	1.5	POLY2 (HOLE2)
Metal	0.5	METAL (HOLEM)

Hole levels are printed on the same line as their corresponding polysilicon or metal levels.

4.1.3 Layout Design Description

The layout design and fabrication of thermal actuators in this thesis all follow the MUMPs rules.

4.1.4 The Layout of the Thermal Actuator Design

Figure 4.3 is the scheme of a standard U-shaped thermal actuator layout design. When the current flows through the arms of the actuator, the hot arm extends more than the cold arm. This causes the beam to bend towards the cold arm. The displacement of the tip can be read via the scale in microscope.
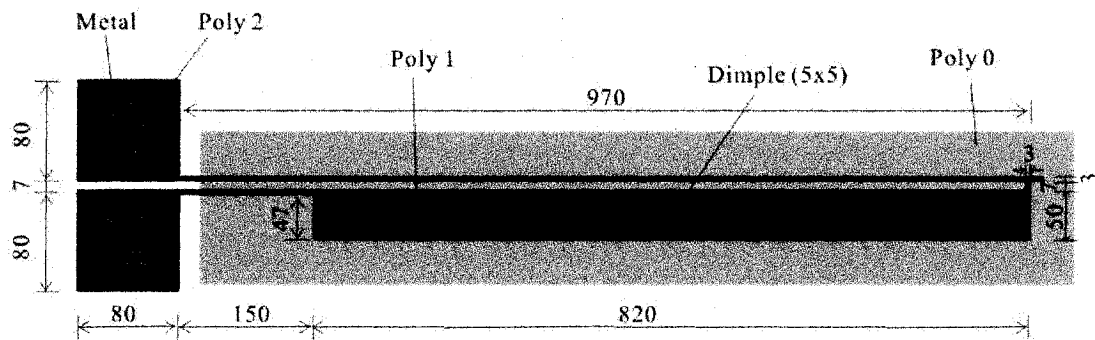
Figure 4.3: The benchmark U-shaped thermal actuator layout

The arms of the thermal actuator are all in the Poly1 layer. Two electrical connection pads are made of Poly0, Poly1, Poly2 and metal layers. There are three dimples that support the beam in order to overcome gravity and the adhesive force and keep a gap between moving arms and the base (Poly0 layer). Anchors fix both the thermal actuator and the scale.

4.2 Experimental Setup

4.2.1 Aims of the Experiment

An experiment was carried out in the laboratory. The objectives of the experiment were:

• to measure the deflection at the tip of the thermal actuators.

• to measure the input conditions (potential and current) which are applied on the test thermal actuator.

• to observe the conditions when the structures begin to move.

• to observe the conditions when plastic deformation occurs on the hot arm. (destructive)

• to observe the highest temperature point on the hot arm after it burned. (destructive)

4.2.2 The Experimental Equipment

The experimental work is carried out in the laboratory in order to validate the analytical results. A simple set of equipment was used, which is listed below:

1. Clean room
2. Microscope
3. Precision DC power supply
4. Multimeter
5. Socket of chips
6. Digital microscope camera
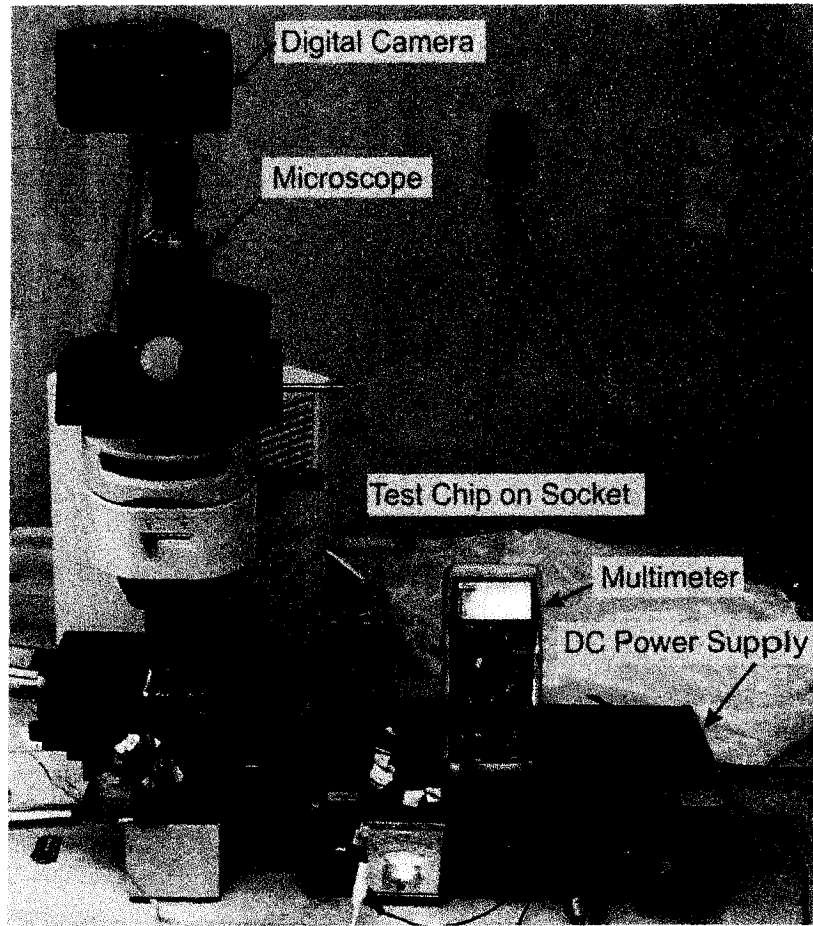
Figure 4.4: Experiment equipment installation
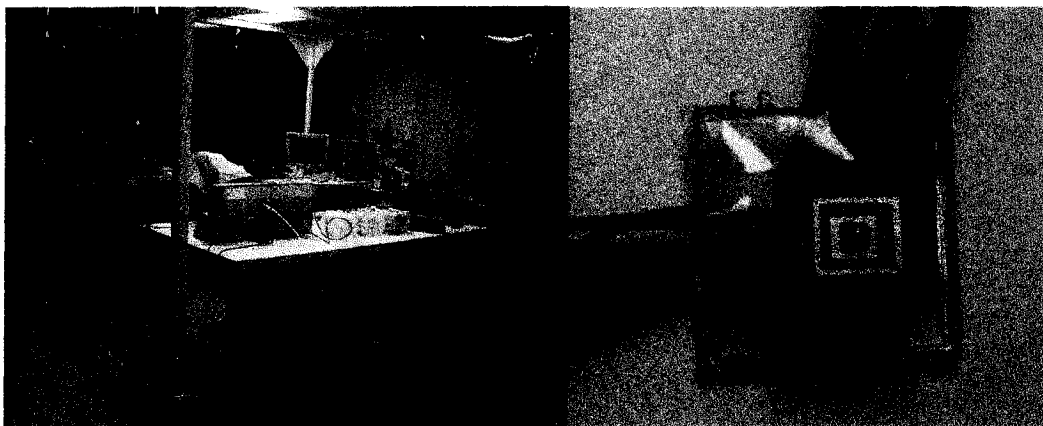
(a)   (b)

Figure 4.5: (a) clean room   (b) the test chip on a socket connected with wires

89

4.2.3 Schematics of the Test Circuit

The chip was mounted in a support from which the electrical terminals were made available. The electric contacts to the pads holding the thermal actuator to be tested were connected in a circuit at the points A and B as shown in the Figure 4.6.
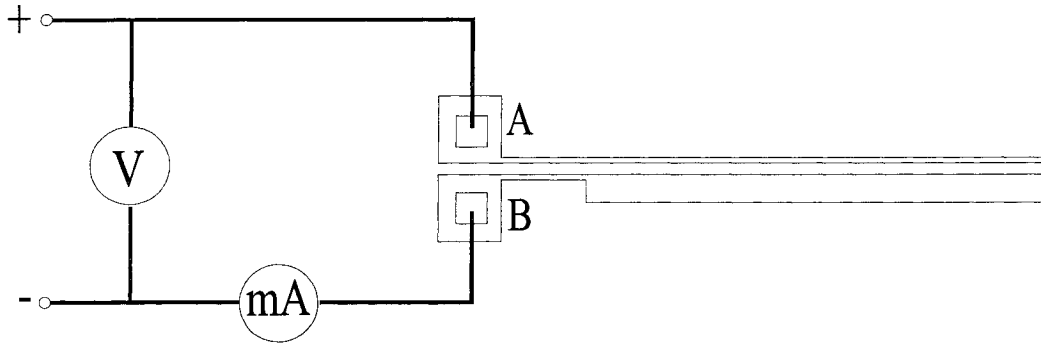
Figure 4.6: The schematics of the measurement

4.2.4 The Results of the Tests

For the thermal actuators the same geometries as Table2.2, the test results are listed in Table 4.2:

Table 4.2 Test results

U (V)	I (mA)	R (KΩ)	P (mW)	Deflection (μm)	Photo
5	2.08	2.40	10.2	Not observed	(a)
10	3.67	2.73	36.7	23	(b)
15	4.74	3.17	71.1	40	(c)
20	5.54	3.61	110.8	55	(d)
25	5.99	4.17	149.75	58	

(a)

(b)

(c)

(d)
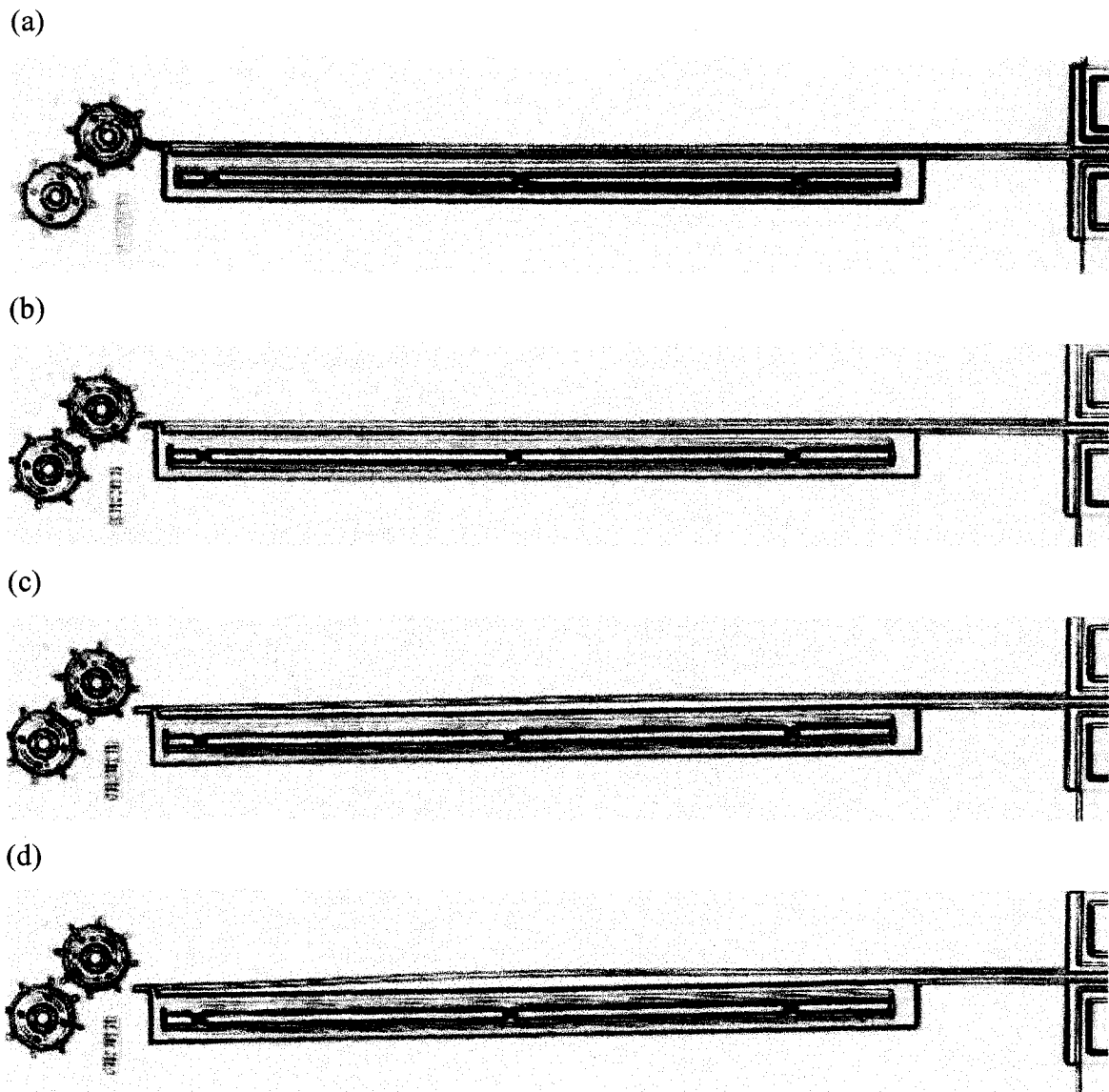
Figure 4.7:   Photos of the thermal actuator's whole image in test

(a) photo of the thermal actuator under a potential of 5V

(b) photo of the thermal actuator under a potential of 10V

(c) photo of the thermal actuator under a potential of 15V

(d) photo of the thermal actuator under a potential of 20V

(a)
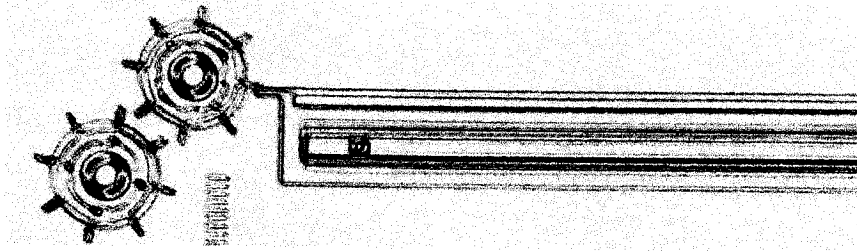
(b)
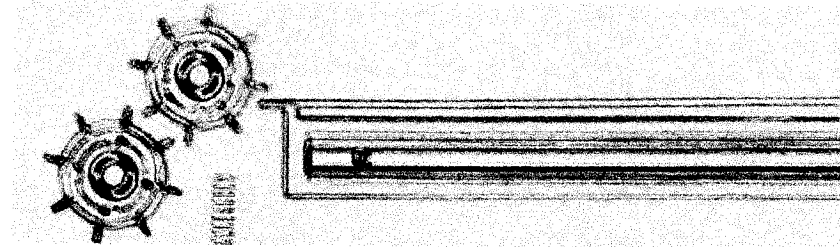
(c)
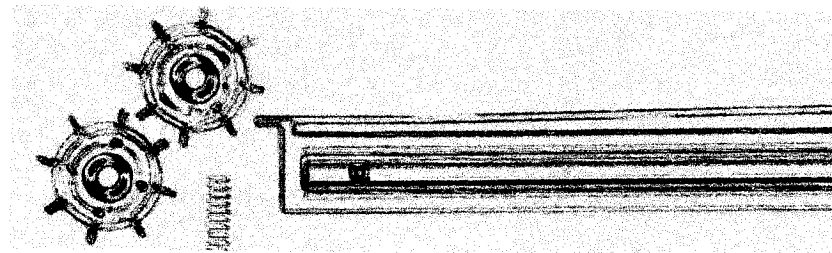
(d)
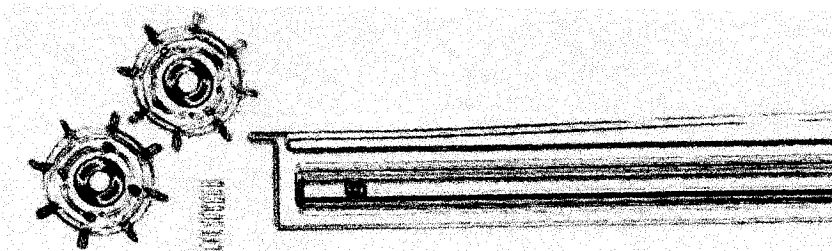
Figure 4.8:   Photos of the enlarged image at the tip of the thermal actuator in test

(a) photo of the thermal actuator under a potential of 5V

(b) photo of the thermal actuator under a potential of 10V

(c) photo of the thermal actuator under a potential of 15V

(d) photo of the thermal actuator under a potential of 20V
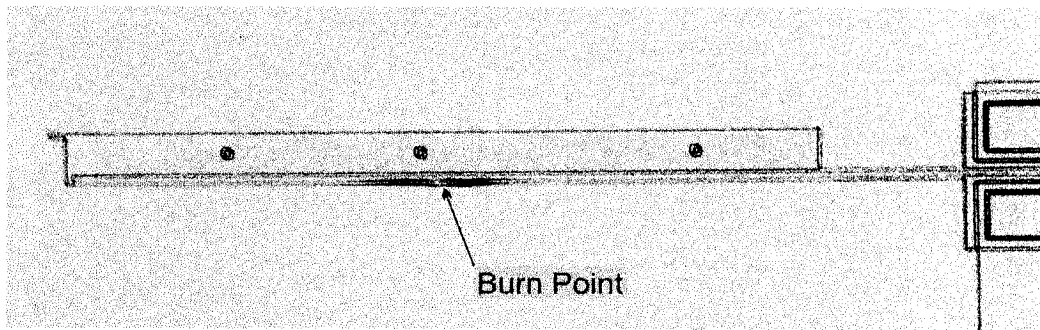
Figure 4.9: Photo of the burn point on the thermal actuator

4.2.5 Experimental Results Expression and Discussion

The experiment was carried out in a clean room. The test chip was mounted on a socket connected with wires. A DC power supply with 0-40V tuning range provided the actuating voltage. A multimeter was installed in the circuit to measure the current as illustrated in Figure 4.6. In order to record the thermal actuator's motion, a digital camera was installed on the top of the microscope to record pictures and movie clips.

When a current is passed through the circuit as well as through the test thermal actuator, the hot arm begins to expand and bend. However there is no perceivable deflection at the tip of the structure, until the potential reaches about 10V. After the actuator starts to move, the deflection at the tip increases as a direct ratio with the potential increasing, till the potential reaches around 20V. When the applied potential is higher than 20V, the hot arm would expand but the deflection at the tip would change very little. This may be due to the plastic deformation of the hot arm. Any additional power input over this level does not lead to additional deflection under the above conditions.

93

Figure 4.9 illustrates the thermal actuator when the applied potential is above 25V. The hot arm burns out at the middle, when the temperature reaches its peak. Few destructive tests were carried out. Although the burn out has occurred at different applied voltage, all were roughly around 30V. Applied voltages in the vicinity of 30V would not modify the position of the tip recorded at 25V. The picture comes in support of the finding in (2.13) in which the peak temperature will occur at a point on the middle part of the hot arm. This finding is in good agreement with the assumption made in temperature distribution in Chapter 2.

Current and deflection measurements were taken for voltage increments of 5V:
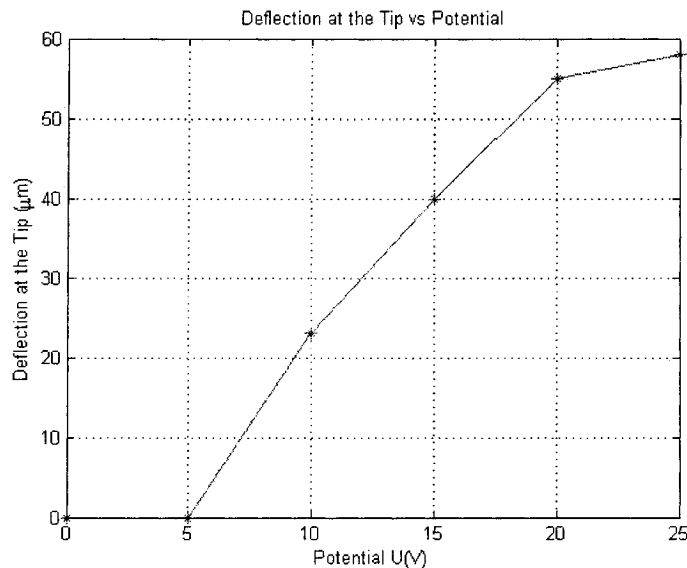
Figure 4.10:   Experimental result: the deflections at the tip of the benchmark thermal actuator under from 0 to 25V

Figure 4.10 shows that the deflection at the tip of the thermal actuator which increases almost linearly, for applied voltages ranging from 5 to 20V.
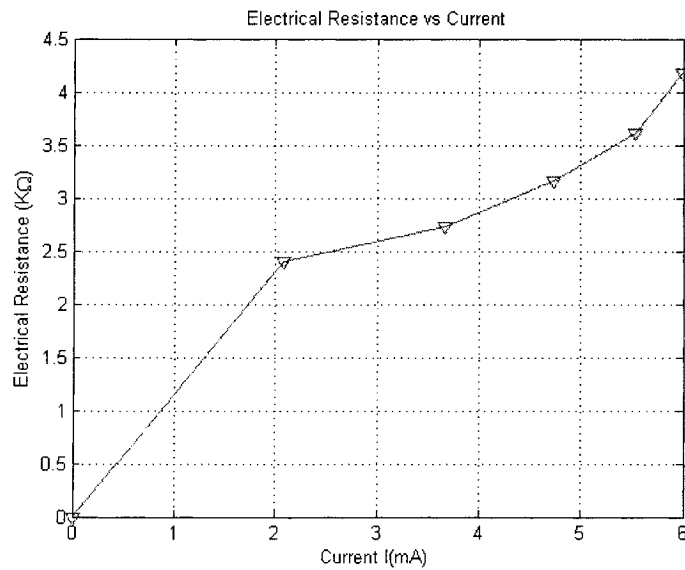
94
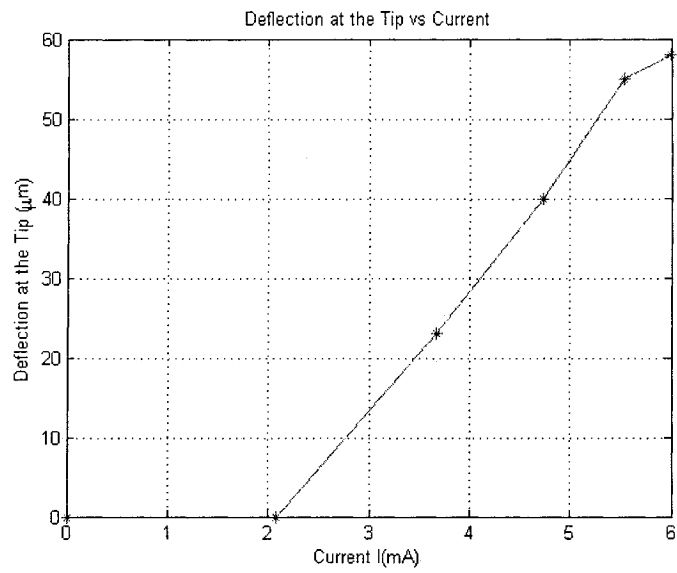
Figure 4.11: Experimental result: the deflections at the tip of the benchmark thermal actuator under from 0 to 5.99mA
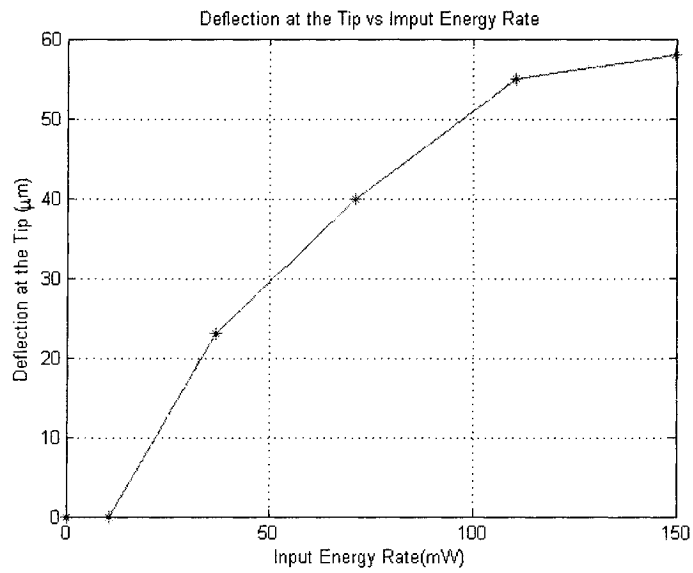
Figure 4.12: Experimental result: the deflections at the tip of the benchmark thermal actuator under from 0 to 149.75mW

Figure 4.11 shows that the deflection at the tip of the thermal actuator increases almost linearly, from the moment it started to move to 5.54mA, when 20V is applied. From Figure 4.11, 4.12, one can see that the second result point, which is under 5V potential with no deflection observed, is at very low current and hence has very low input energy. Hence, when 5V is applied, there is not enough energy to overcome the adhesive friction force between dimples and POLY0 lay, and then to initiate the movement.
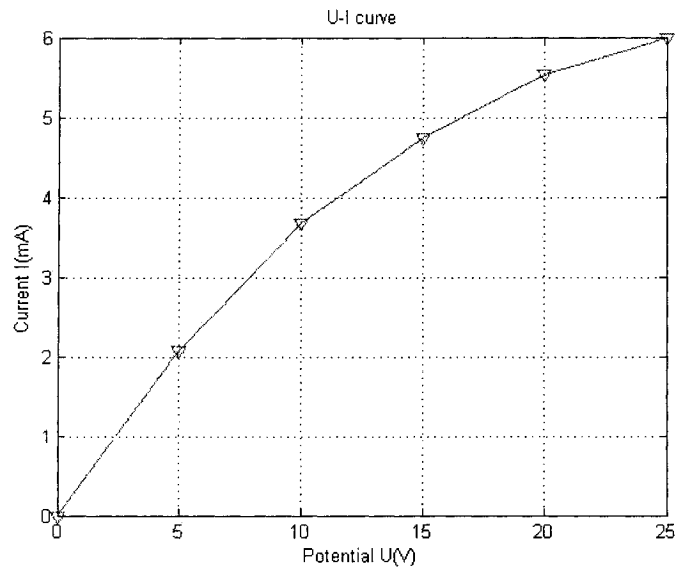
Figure 4.13: Experimental result: U-I curve

Figure 4.13 U-I curve shows that the current does not increase linearly with the potential. That is the result of the temperature dependency of the silicon electrical resistance.
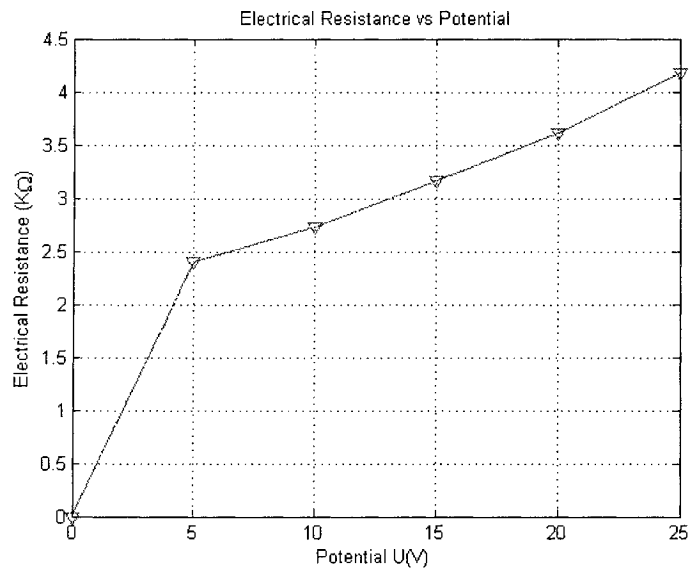
Figure 4.14: Experimental result: the electrical resistance of the benchmark
thermal actuator under from 0 to 25V

Figure 4.15: Experimental result: the electrical resistance of the benchmark
thermal actuator under from 0 to 5.99mA
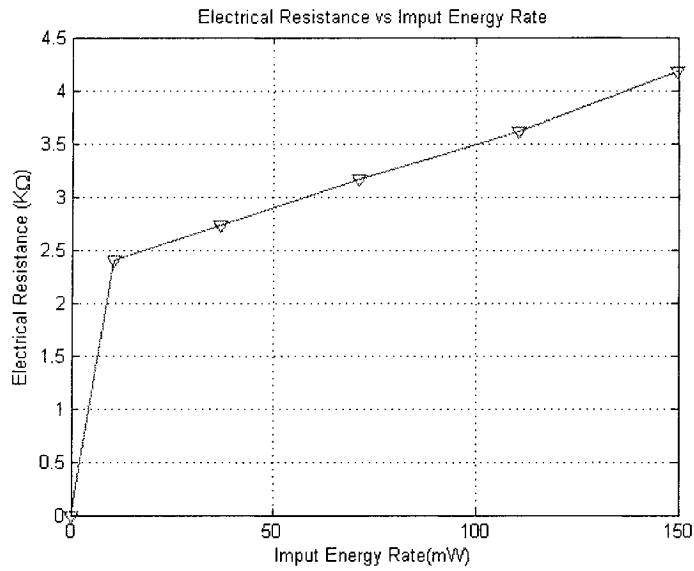
Figure 4.16: Experimental result: the electrical resistance of the benchmark
thermal actuator under from 0 to 149.75mW

Figure 4.14, 4.15, and 4.16 show that when the applied voltage increases, the
applied current increases, or as the input energy increases, the electrical resistance
of the thermal actuator increases. These phenomena conclude that the electrical
resistance of silicon increases with the temperature.

4.2.6 Experiment Summary

Multiple tests have been performed on the benchmark thermal actuator. Some of the
structures have not moved at all while some other structures burnt under 20 to 25 V
excitation input. Other geometries have also been tested but other thermal actuator
type did not move. This may be due to the stiction or to the incomplete release of
the structures. The recorded results on the five different thermal actuators have been
averaged and these results are presented in Table 4.2. The results of the stroke
measurement were quite consistent within a variation of + 3μm for the specific
readings.

CHAPTER 5 SIMULATION AND PARAMETRIC STUDY

5.1 Introduction

The design of micro thermal actuators has proved to be a complex task. Starting with the thermal analysis, the dissipated energy balance requires a good evaluation of the thermal gradient through the micro thermal actuator while the temperature distribution estimation needs a good estimate of the energy dissipation. Further, the electro-mechanical properties of the thermal micro-actuator which are of the most interest to the design will be significantly influenced by the thermal management. Since the above task of fine-tuning the geometric parameter of the micro thermal actuator is complex and laborious, a parametric study based on simulation of multi physics interaction at the micro thermal actuator is carried out. To understand the sensitivity of the geometric feature into the performance of the micro thermal actuator, all geometric features are varied, one at a time, with respect to the benchmark thermal actuator. Geometries are given in Table 5.2 and the physical quantities to be evaluated are listed in Table 5.1.

Table 5.1 Physical quantities to be evaluated by simulations

Physical quantity	Symbol	Relation	FEM	Experimental
Electrical resistance	R	(2.2)		X
Input energy rate	E_g	(2.3)		X
Factor coefficient	λ	(2.10)		
Average temperature	$\overline{T}_{av}$	(2.18)		
Maximum temperature	T_{max}	(2.14)	X	
Deflection at the tip	d	(3.17)	X	X

Stiffness	K_s	(3.34)		
Force generated at the tip	F	(3.36)		
Natural frequency (first mode)	f_n	Chapter 3.2.2		
Thermal frequency	f_t	(3.45)		
Duration for one stroke	Δt	(3.44)		
Efficiency	η	(3.47)		
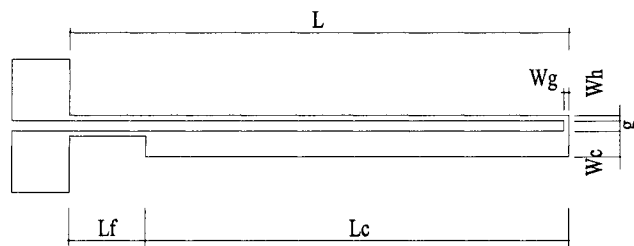
Table 5.2 Geometries variation range with respect to benchmark dimensions

Geometric feature	Variation	Relationship
L	-20% ~ +20%	L_f=constant, L_c=L-L_f
L_f	-66.7% ~ +200%	L= constant, L_c=L-L_f
g	-57.1% ~ +200%	
W_h=W_f	-66.7% ~ +66.7%	
W_c	-60% ~ +60%	
h (thickness)	-50% ~ +50%	

Geometric dimensions which are not described in Table 5.2 are the same as those of benchmark thermal actuator in Table 2.1. Simulations on the physical quantities in Table 5.1 are divided into six groups according to six geometric variations given in Table 5.2.

5.2 Simulation by Finite Element Method:

This simulation is using the commercial FEA, multi-physics package of ANSYS. The coupled-field multi-physics model is built, which takes into account the interaction between thermal, electric and mechanical disciplines of engineering. The results from one analysis become input for the next analysis.

Using SOLID98, which is a 10-node tetrahedral element with TEMP and VOLT degrees of freedom apart from displacements and rotation, the model is volume meshed into 2334 nodes by choosing 30µm as the maximum element edge length.

The boundary conditions are represented by the potential difference applied at the pads of thermal actuator. The thermal analysis imposed the temperature of the environment at the two pads. The boundary conditions in the mechanical analysis assume all degrees of freedom at the pads as zero.

The simulation results for the thermal and mechanical strain are illustrated in Figure 5.1, and 5.2. Meanwhile, analytical derivations have been used to simulate the performance of the micro thermal actuators. The deflection at the tip at specific voltages was measured in the experiments.
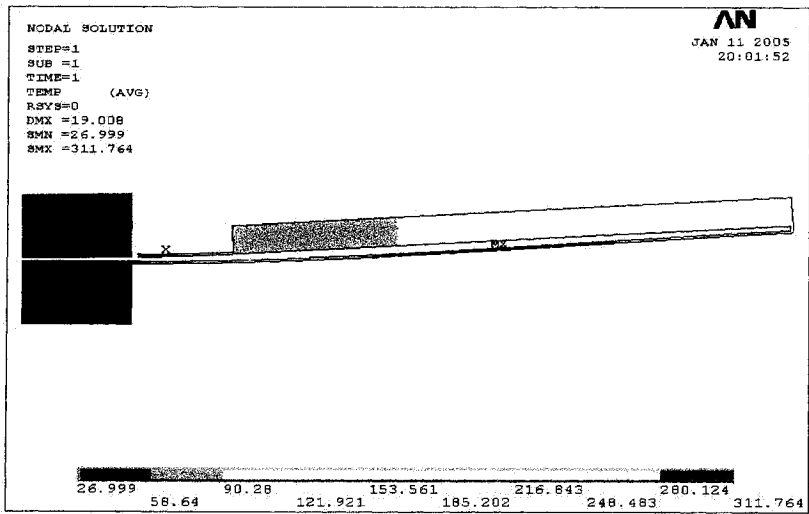
Figure 5.1: FEM result of temperature distribution along the structure ($^\circ C$) (under 10V)
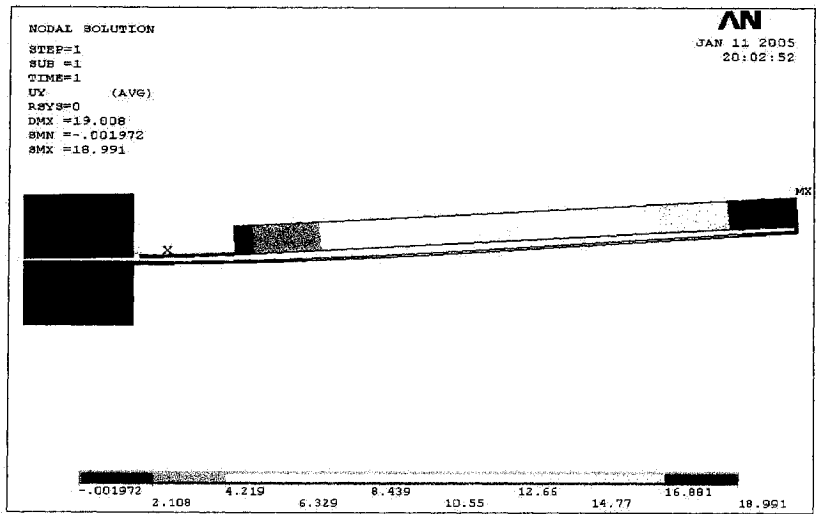
Figure 5.2: FEM result of displacement along the structure (μm) (under 10V)
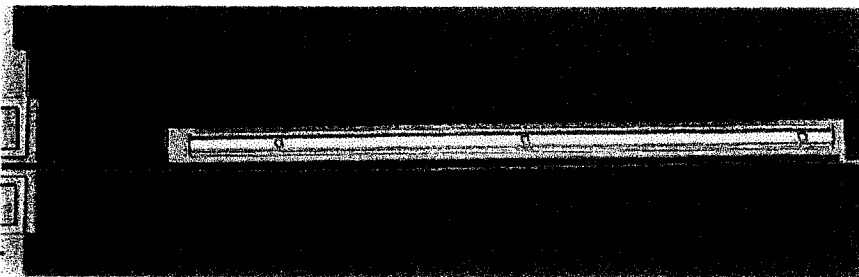
Figure 5.3: Experimental result of displacement along the structure (μm) (under 10V)

102

5.3 Comparison of the Results from Experiments, FEM Simulation and Theoretical Analysis
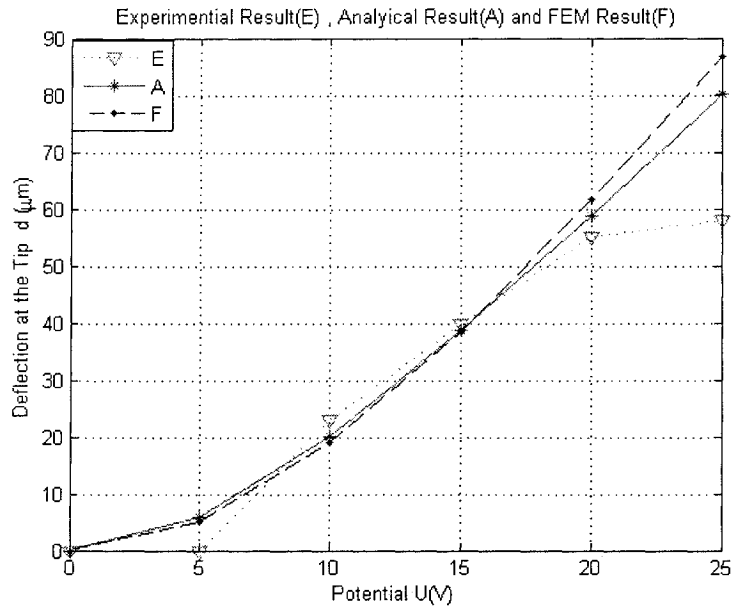
Figure 5.4: Deflection at tip under different potential applied

The deflection at the tip of the benchmark thermal actuator was measured, analytically calculated and determined by FEM. The three results match reasonably well for voltage from 10 to 20V, with 8% error (as from Figure 5.4).

The current through the thermal actuator and the leading circuit was measured and calculated. The two results are in very good agreement within 5% error (as from Figure 5.5).
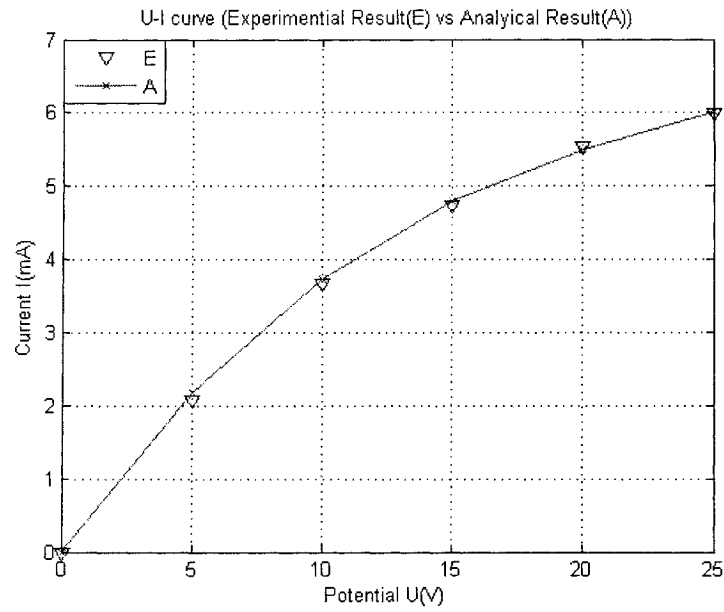
Figure 5.5: U-I curve (experimental result vs analytical result)
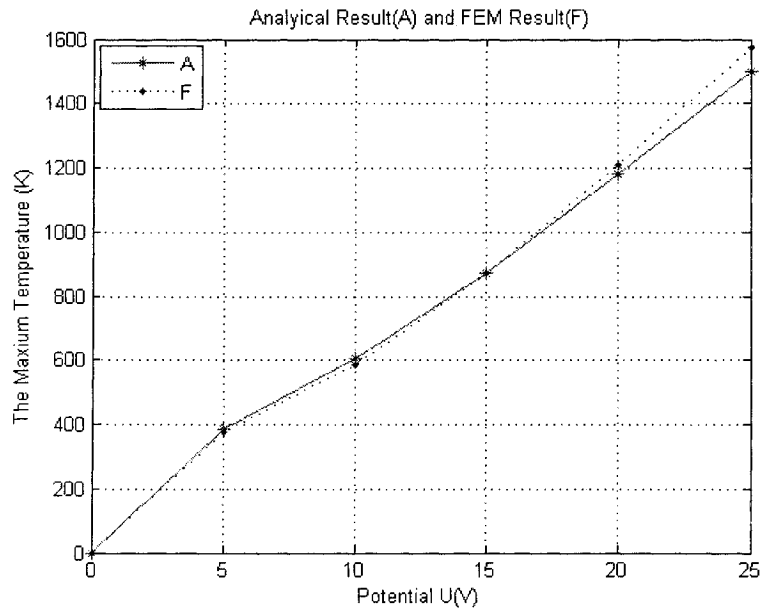
Figure 5.6: The maximum temperature under different potential applied

The peak temperature in the thermal actuator was found analytically and also evaluated by FEM. The accuracy over the 0 to 25V is within 5% error (Figure 5.6).

5.4 The Geometric Influence on the Thermal and Mechanical Properties of Micro Thermal Actuators

Process variance due to geometry variations will influence the thermal and mechanical properties of the micro thermal actuators in several ways. For example, when geometry of the structure changes, the electrical resistance changes (as from 2.2), with corresponding increase in the input energy changes (as from 2.3), and the thermal mass changes which influences the temperature distribution, average temperature, and thermal expansion of the structure. Secondly, some properties, such as natural frequency and stiffness will not be strongly affected by the input energy and temperature. Therefore, they are significantly influenced by geometry changes. Sometimes, two specific changes will influence one property in two conflicting directions which will make prediction of the properties more difficult and uncertain.

The following simulation is carried out on the basis of the analytical formulations as indicated in Table 5.1. The physical quantities in Table 5.1.are evaluated under the assumption that the geometry features in Table 5.2 change one at a time while the others remain unchanged at the benchmark values.

5.5 The Results of the Parametric Study

5.5.1 The Length of the Hot Arm L is Variable while the Length of the Flexure L_f is Constant – Table 5.2 Line 1

105
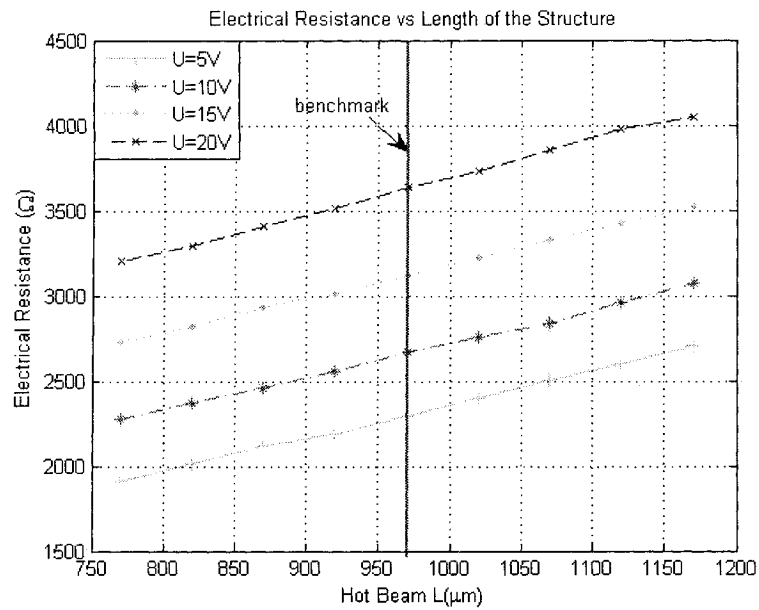
Figure 5.7: Electrical resistance vs length of the structure
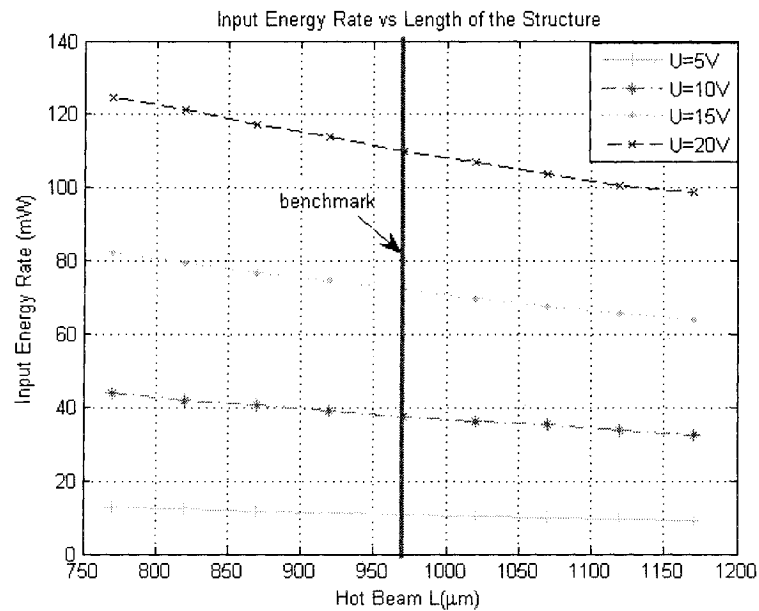
Figure 5.8: Input energy vs length of the structure

106
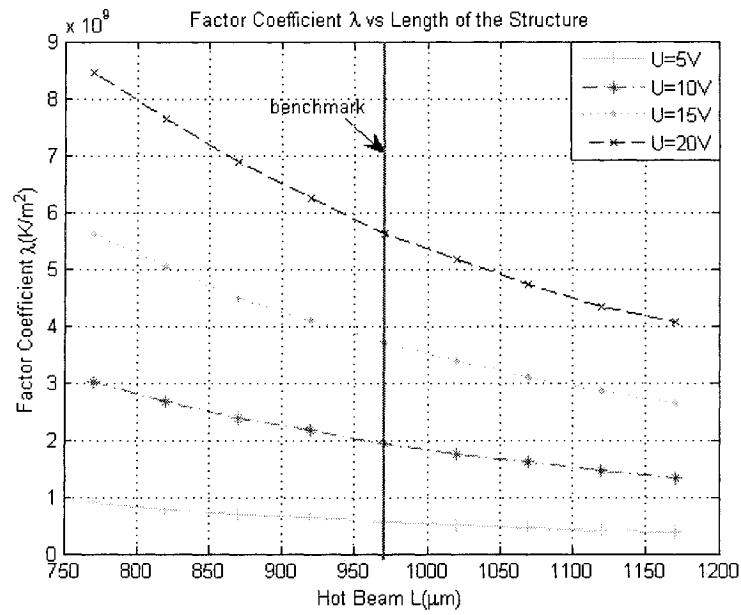
Figure 5.9: Factor coefficient λ vs length of the structure
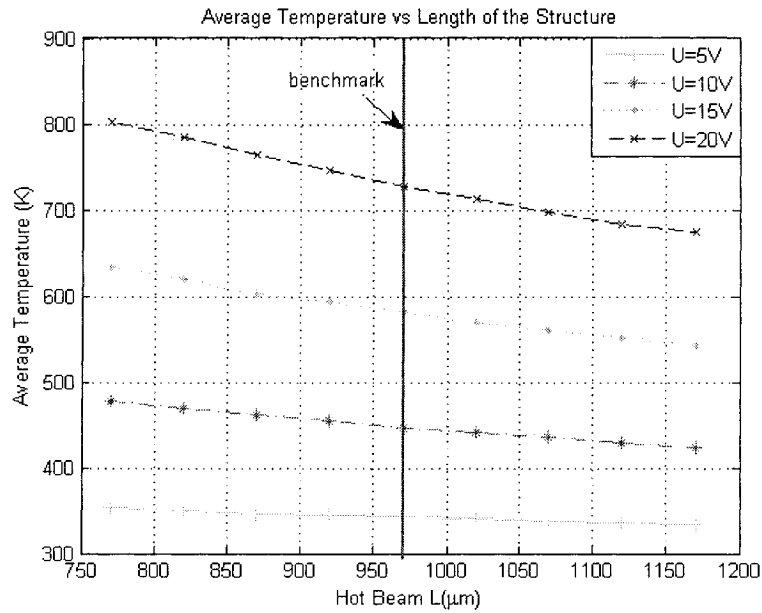
Figure 5.10: Average temperature vs length of the structure

107
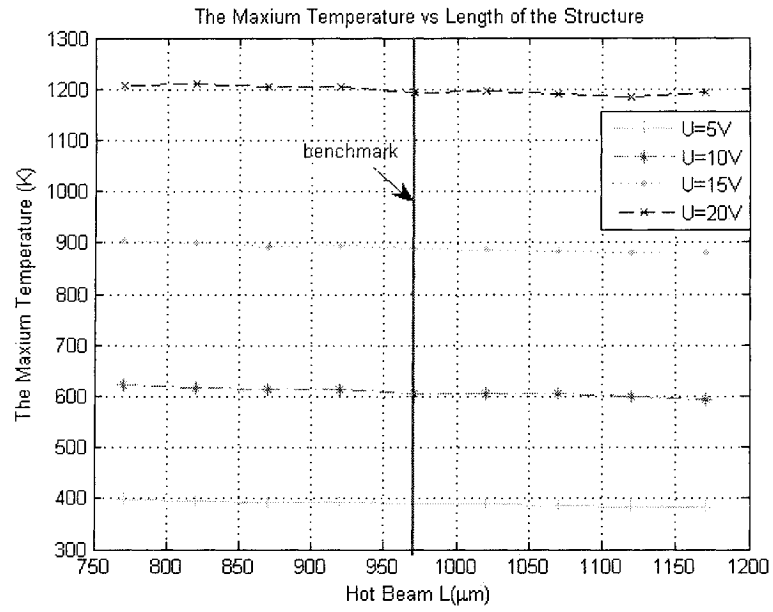
Figure 5.11: The maximum temperature vs length of the structure
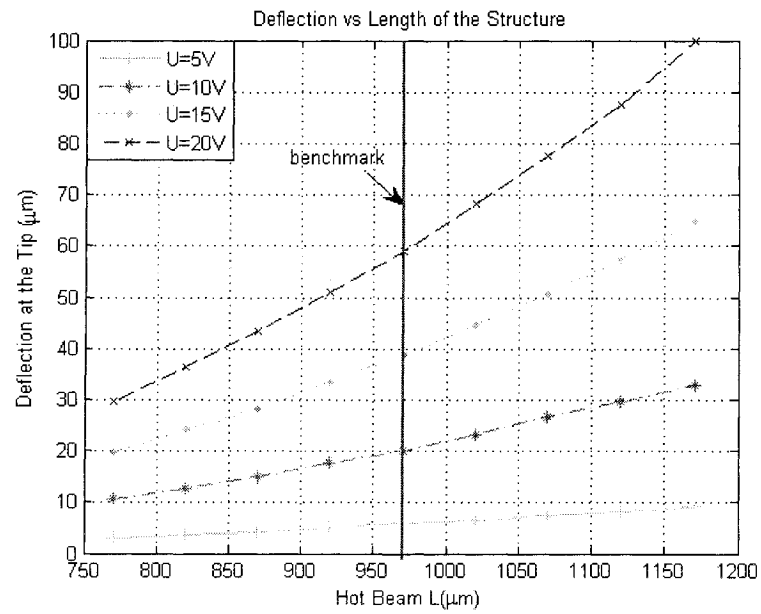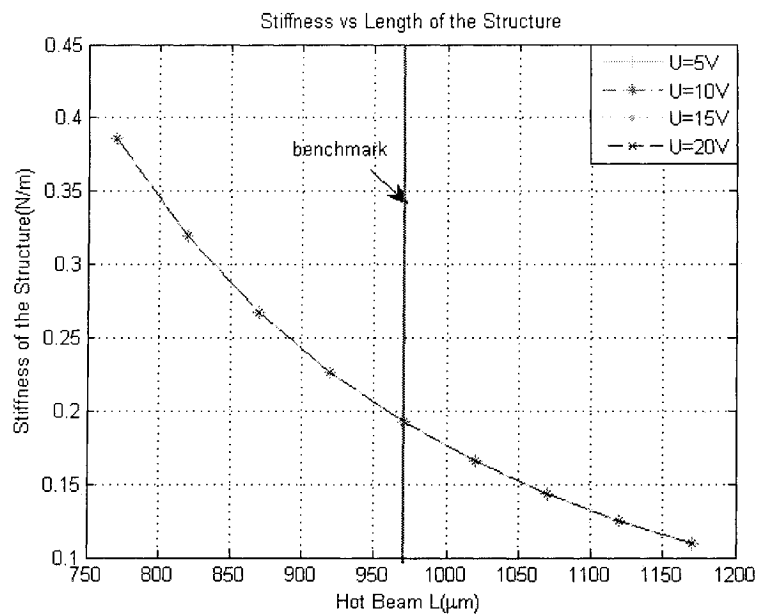

Figure 5.12: Deflection vs length of the structure
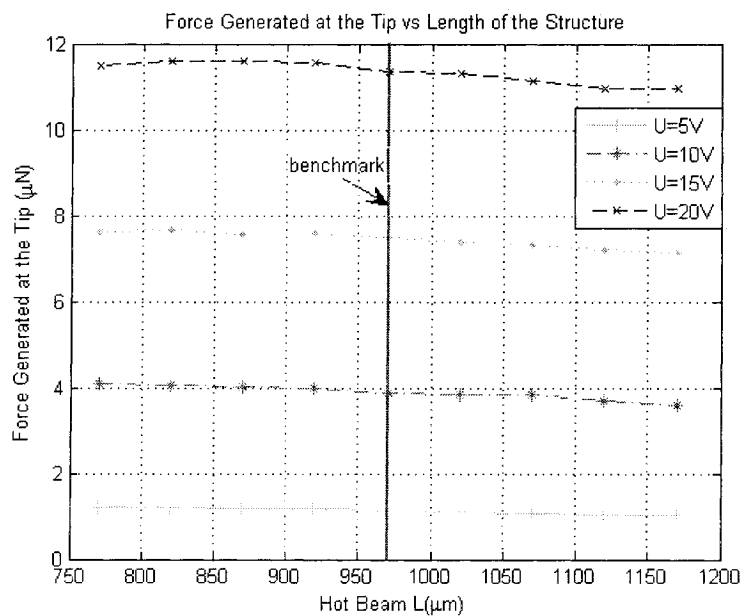
108

Figure 5.13: Stiffness vs length of the structure

Figure 5.14: Force generated at the tip vs length of the structure

109
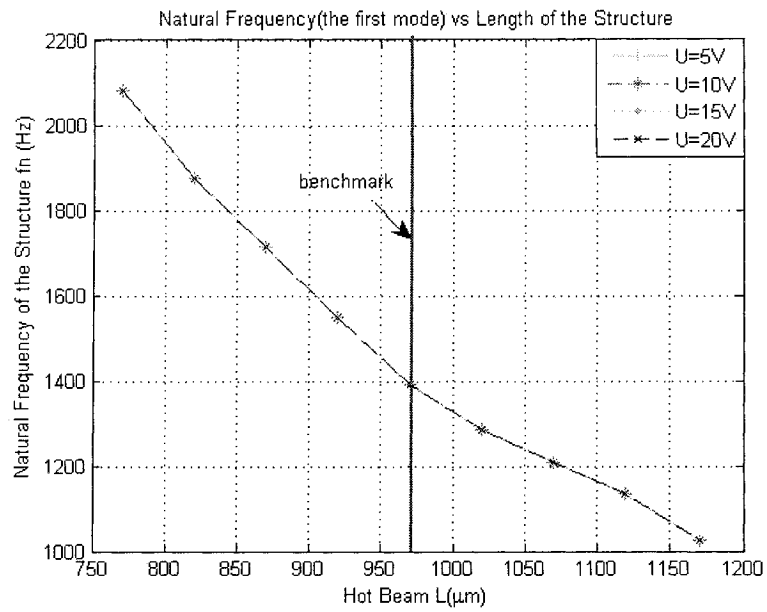
Figure 5.15: Natural frequency vs length of the structure
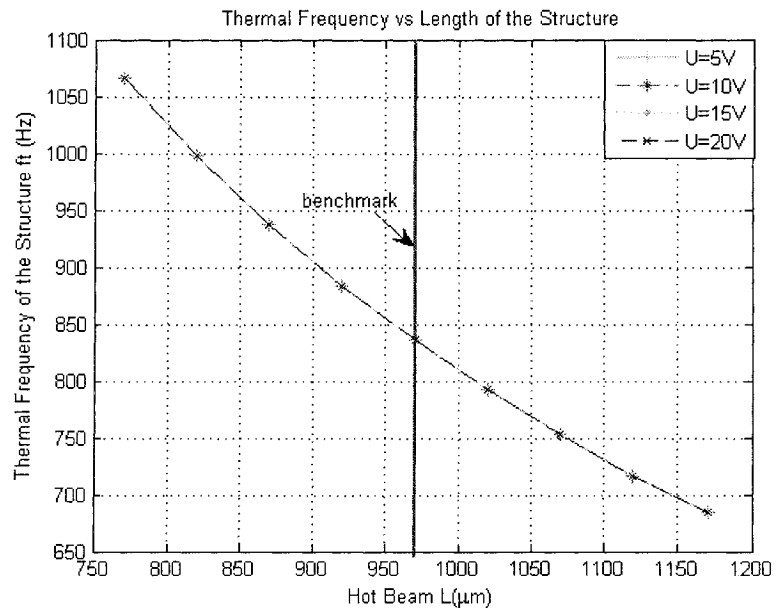
Figure 5.16: Thermal frequency vs length of the structure

110
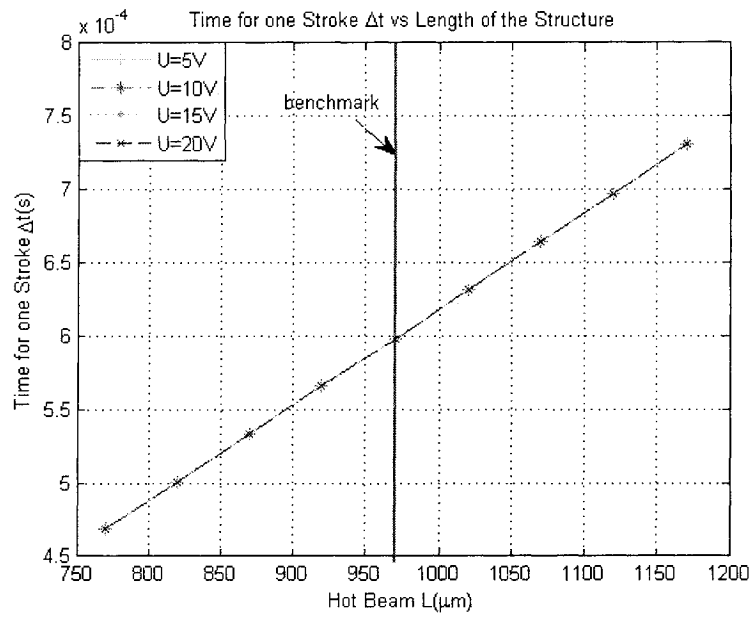
Figure 5.17: Time for one stroke Δt vs length of the structure
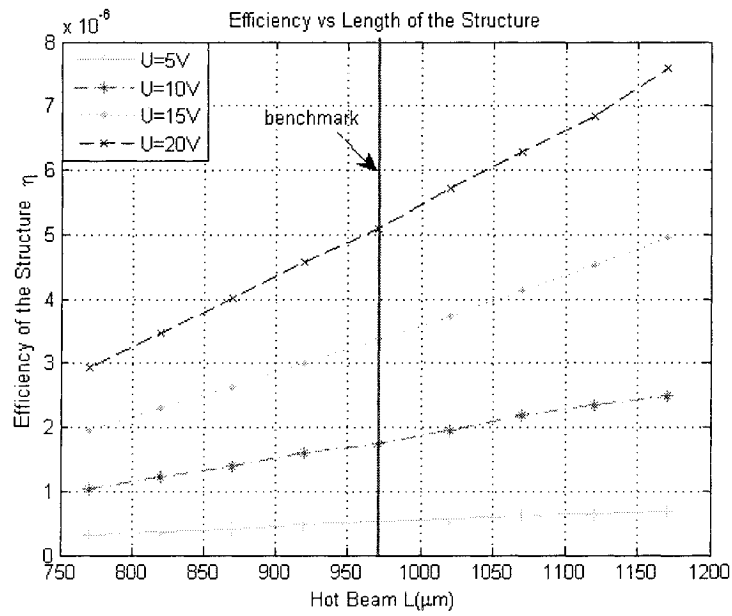
Figure 5.18: Efficiency vs length of the structure

111

Figure 5.7 to 5.18 show the variation of the physical quantities in Table 5.1 when the total length L varies by ± 20% of the benchmark value. This set of simulations assume that the length of the hot beam L changes. The objective of the parametric study is to understand the influence of the various geometric parameters on the performance of the generic thermal actuator. The change in geometric parameters is performed on the total length of the hot arm L, and the length of the cold arm L_c changes correspondingly, while the length of the flexure L_f, the width of each segment, and the thickness of the structure are assumed constant.

When L increases, L_c increases too and hence does the volume of the structure. Those two length changes cause the electrical resistance to increase (as from 2.2 and Figure 5.7). The input energy rate E_g, determined through Joule heating, decreases (as from 2.3 and Figure 5.8). The coefficient λ, which is influenced by the input energy rate and the volume or thermal mass of the whole structure (as from 2.10 and Figure 5.9), causes decrease in temperature distribution, average temperature in each segment, and the maximum temperature (as from Figure 5.10, 5.11 and relations from 2.13 to 2.18). Though the temperature decrease will reduce thermal expansion, the longer length of the structure will get more thermal expansion (as from Figure 3.2). The result of these two opposite influence is that the deflection significantly increases with the rise of L and correspondingly L_c (as from Figure 5.12). The stiffness which is a function of geometry and material, reduces with increase in L (as from 3.34 and Figure 5.13). The force generated at the tip is determined by deflection and the stiffness (as from 3.37). The action in two different directions causes the force generated change very little with the increase of L (as from Figure 5.14). This is because the natural frequency and thermal frequency are both functions of geometry. Figure 5.15 and 5.16 illustrate that they both reduce with the rise in L. The decreased thermal frequency signifies that the time for each stroke increases linearly (as from Figure 5.17). Finally, the efficiency of the structure significantly increases with increase in L because of the

deflection increase and the input energy rate decrease, though the time of stroke increases (as from 3.47 and Figure 5.18).

5.5.2 The Length of the Flexure L_f is Variable while the Length of the Hot Arm L is Constant – Table 5.2 Line 2
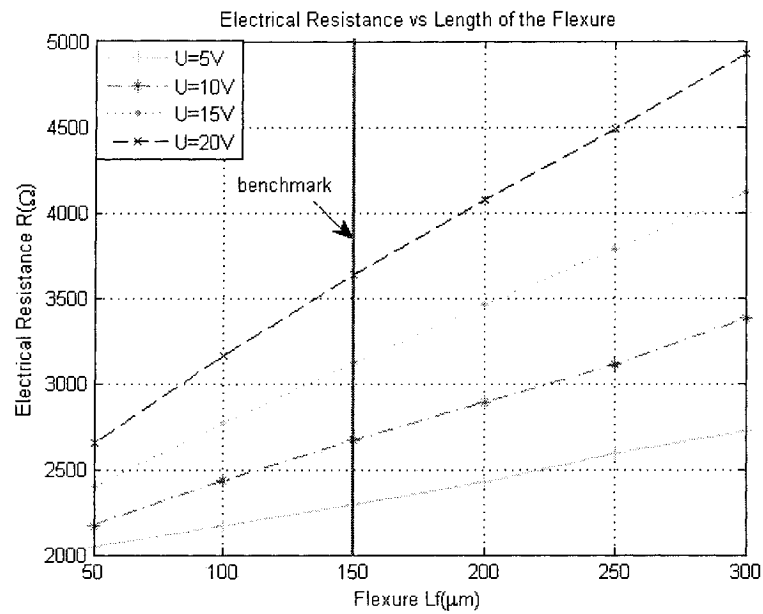

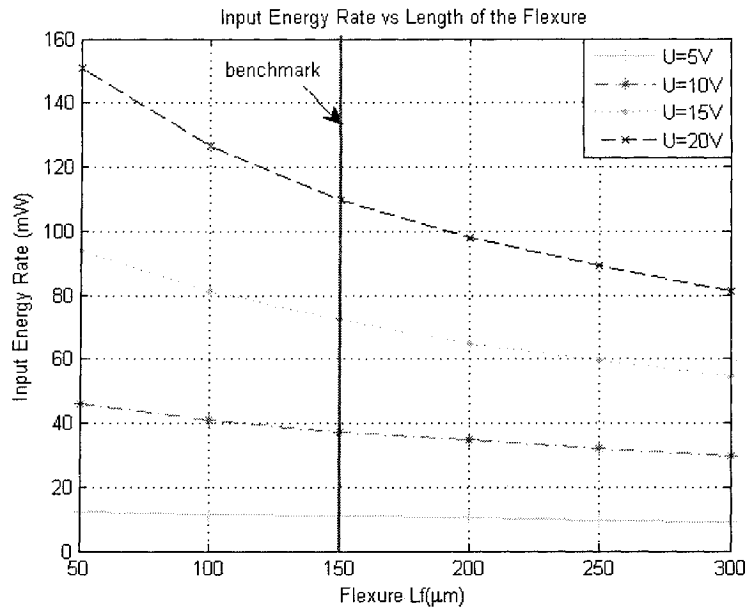Figure 5.19: Electrical resistance vs length of the flexure
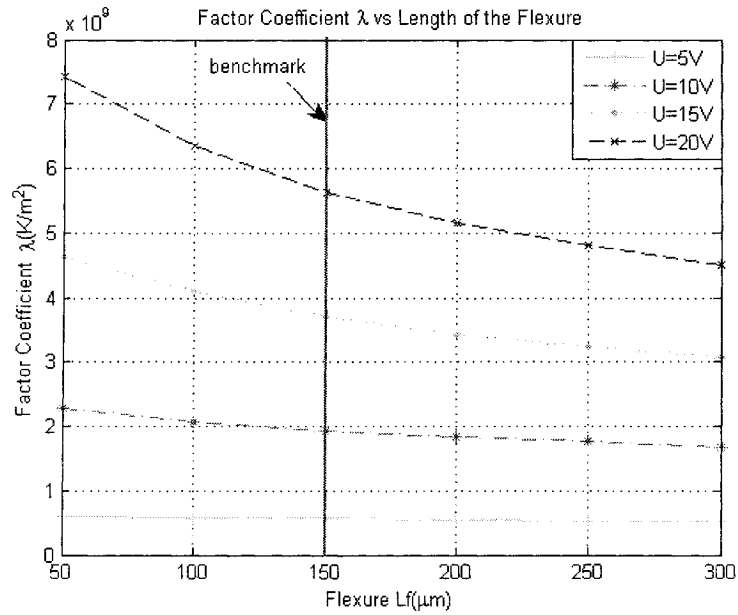
Figure 5.20: Input energy rate vs length of the flexure

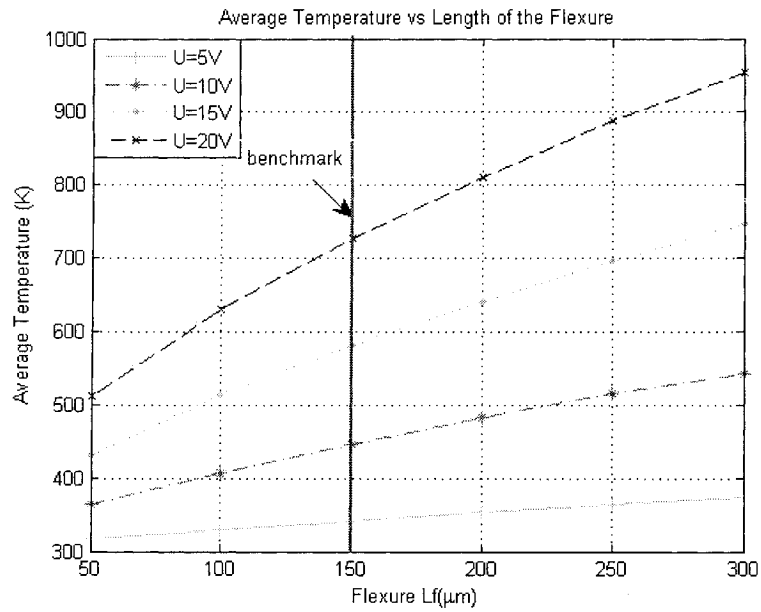Figure 5.21: Factor coefficient λ vs length of the flexure
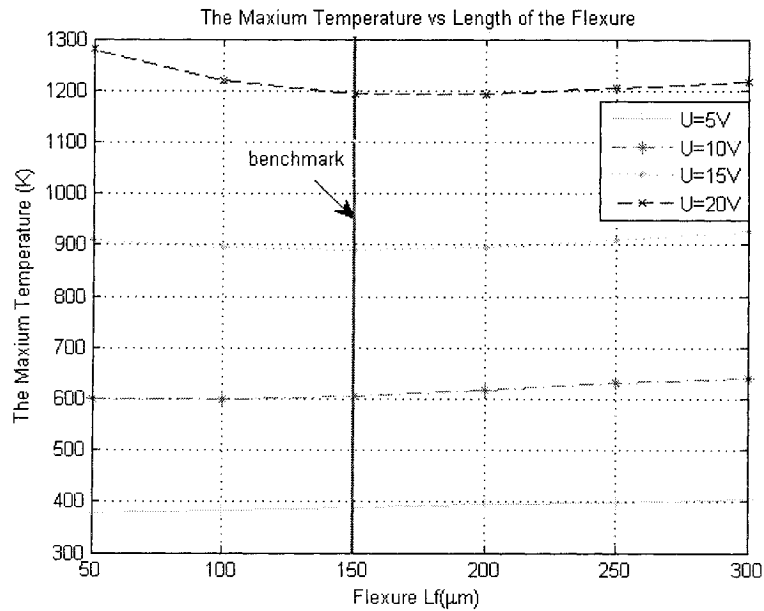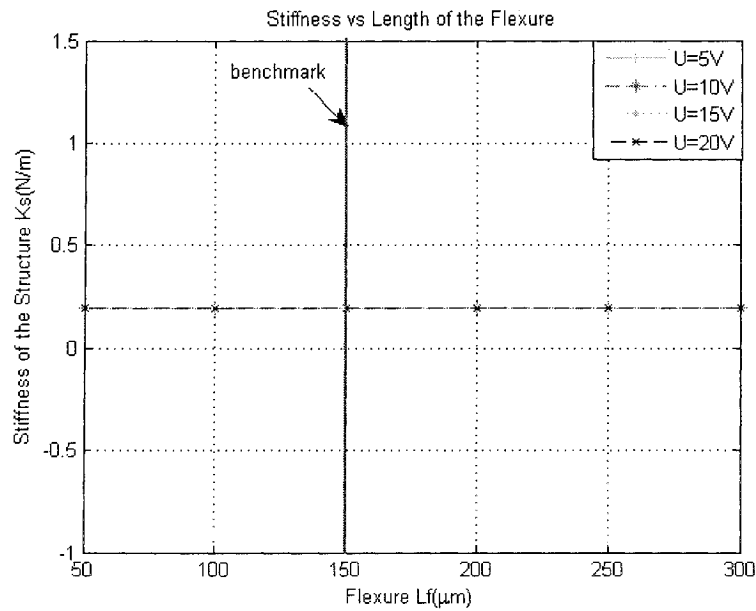
Figure 5.22: Average temperature vs length of the flexure

Figure 5.23: The maximum temperature vs length of the flexure
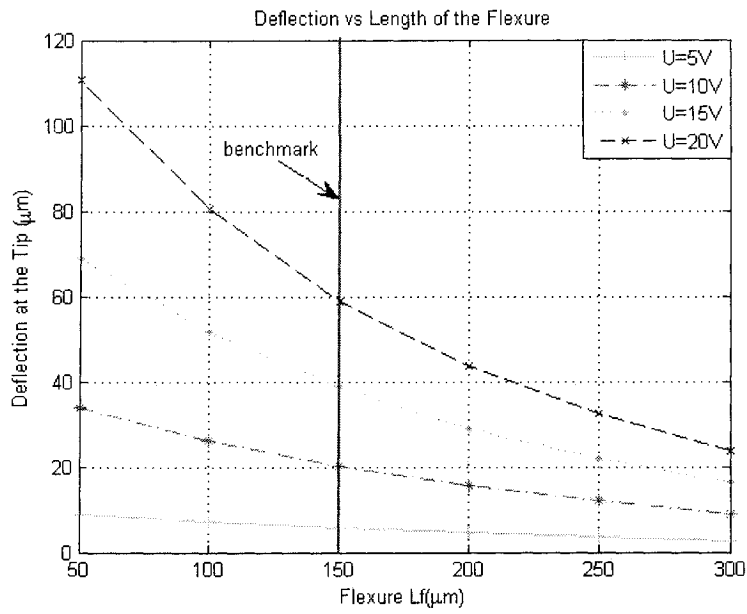
Figure 5.24: Deflection vs length of the flexure

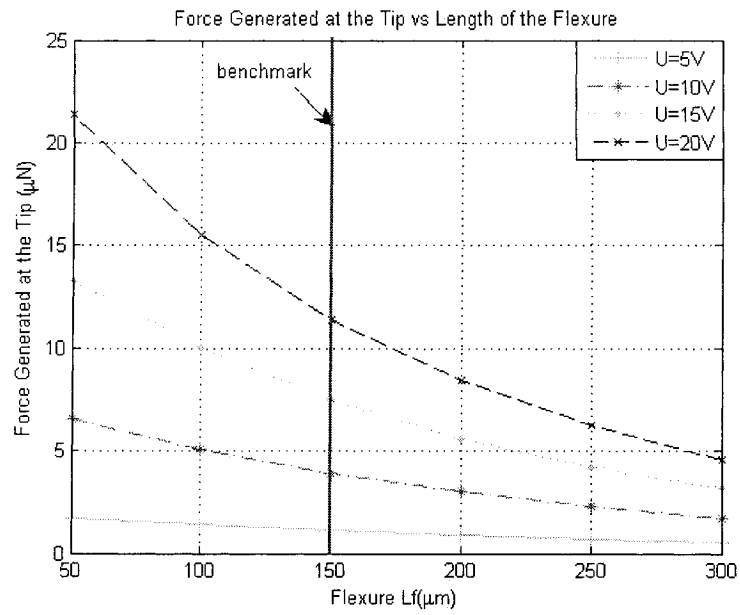Figure 5.25: Stiffness vs length of the flexure

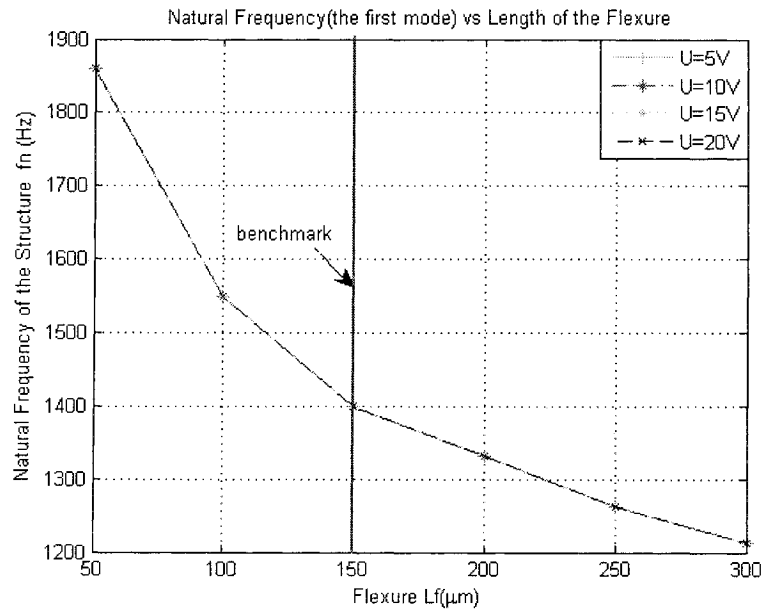Figure 5.26: Force generated at the tip vs length of the flexure

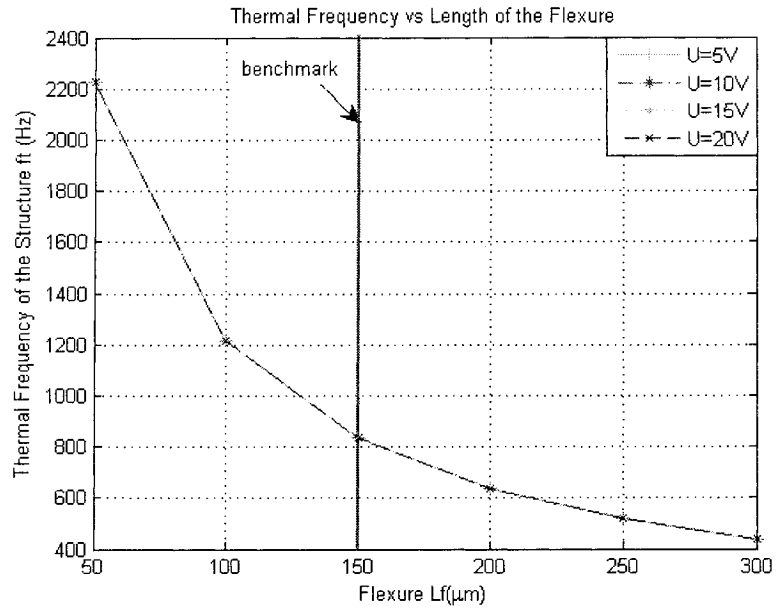Figure 5.27: Natural frequency (the first mode) vs length of the flexure
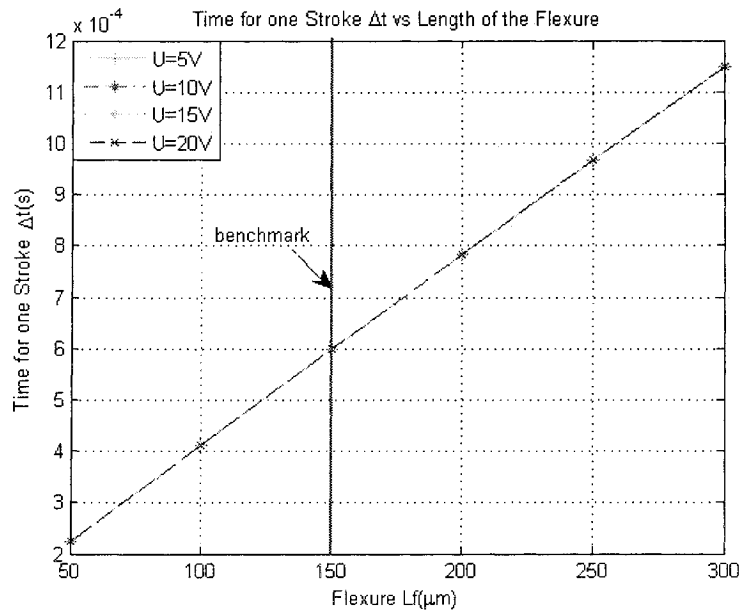
117

Figure 5.28: Thermal frequency vs length of the flexure

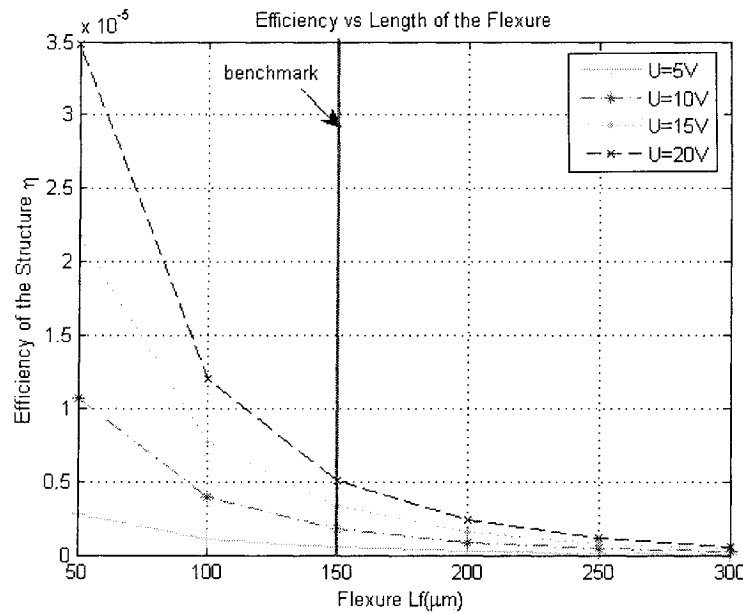Figure 5.29: Time for one stroke Δt vs length of the flexure

118

Figure 5.30: Efficiency vs length of the flexure

The group of the above simulations Figure 5.19 to 5.30 are carried out to study the mechanical and thermal performance when the length of the flexure L_f changes. The study assumes that L_f is variable, and the length of the cold arm L_c changes with the L_f, however, other geometric parameters are constant and are the same as those in Table 2.1.

Since L_f increases, L_c decreases correspondingly because L remains constant. As a result, the thermal volume of the thermal actuator decreases. It is seen from Figure 5.19 and relation 2.2, electrical resistance increases with L_f increase. Input energy rates at a constant applied potential reduces when L_f increases (as from 2.3 and Figure 5.20). The coefficient λ, which determines the temperature distribution, is a function of thermal volume and input energy (as from 2.10). The result of the two effects on λ is a small decrease but more significant at higher potential (as from Figure 5.21). The

119

temperature distribution on the structure is a function of λ (as from 2.13). Figure 5.22 and 5.23 illustrate that both the average and the peak temperatures increase with L_f increase. Figure 5.24 shows that when L_f increases, the deflection at the tip decreases. The reason may be that when L_f increases, the force, which is caused by the asymmetric thermal expansion reduces. The stiffness, on the basis of the assumptions in Chapter 3.3, does not change with L_f change (as from 3.34, 3.35 and Figure 5.25). Force generated at the tip decreases with L_f increase because the deflection at the tip decreases (as from 3.37 and Figure 5.26). The natural frequency and the thermal frequency both function of geometry, decrease when L_f increases (as from 3.45 and Figure 5.27, 5.28). The duration of a cycle increases linearly with L_f increase (as from 3.42, 3.44, and Figure 5.29). From relation 3.47, one can see that the efficiency drops greatly when stiffness is constant, the deflection increases, the input energy rate decreases, and stroke time increases.

5.5.3 The Gap g is Variable while others are Constant – Table 5.2 Line 3
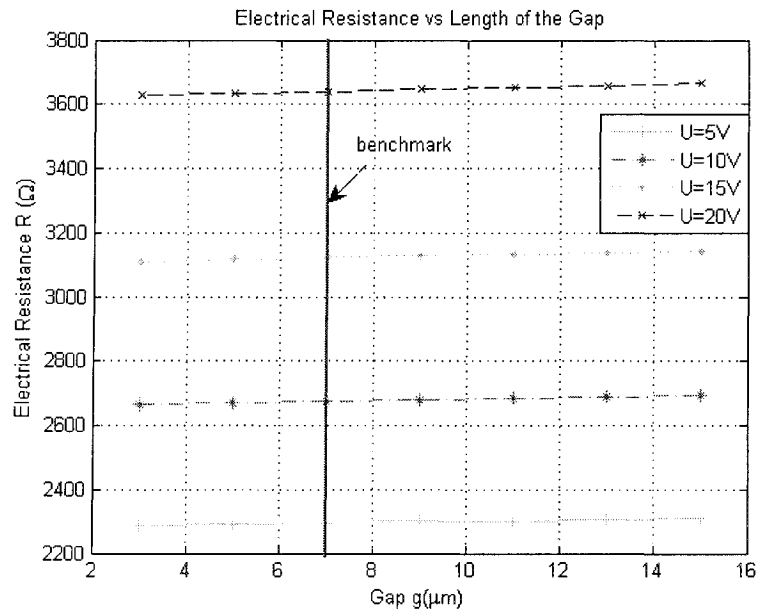

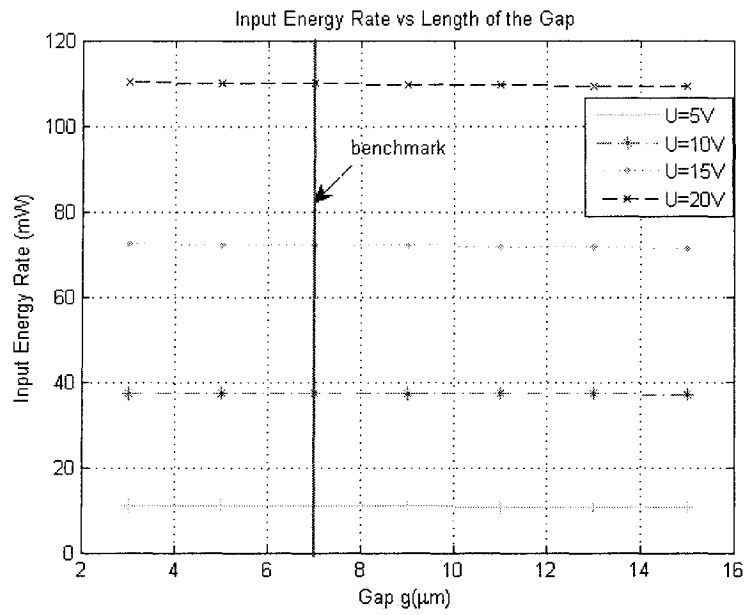Figure 5.31: Electrical resistance vs length of the gap

120

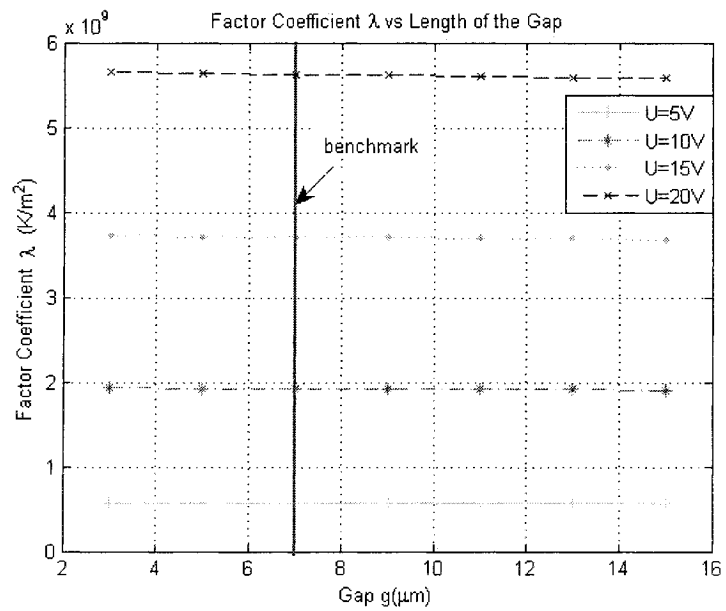Figure 5.32: Input energy rate vs length of the gap

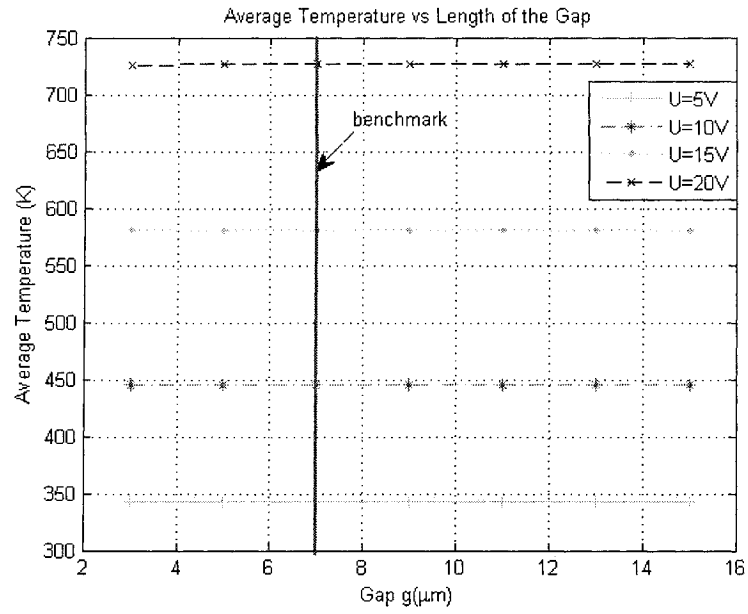Figure 5.33: Factor coefficient λ vs length of the gap

121

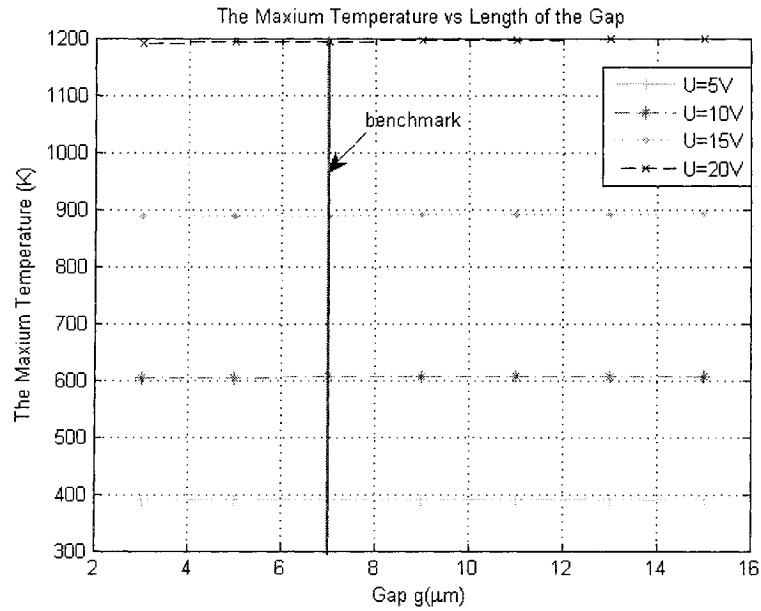Figure 5.34: Average temperature vs length of the gap

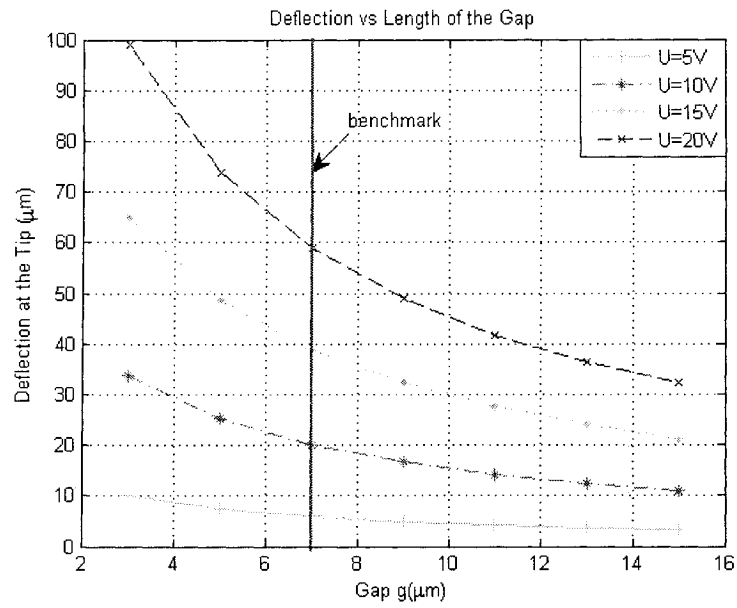Figure 5.35: The maximum temperature vs length of the gap

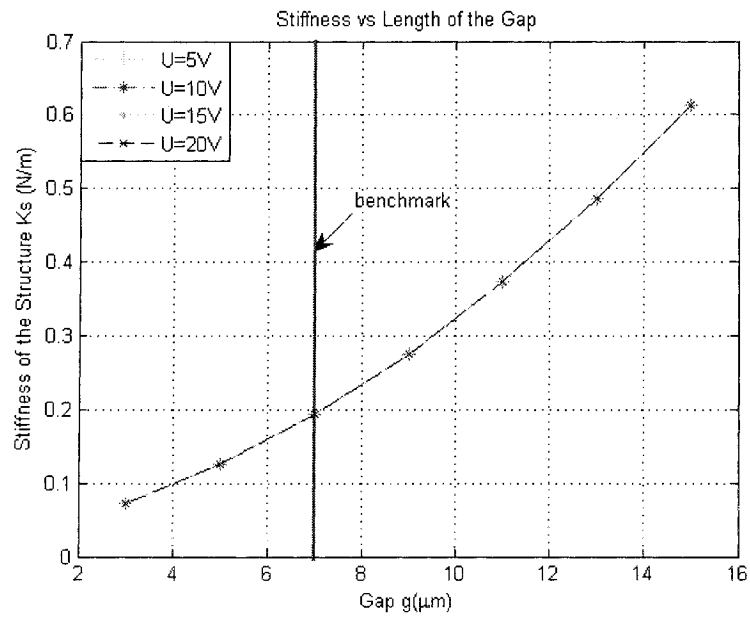Figure 5.36: Deflection vs length of the gap

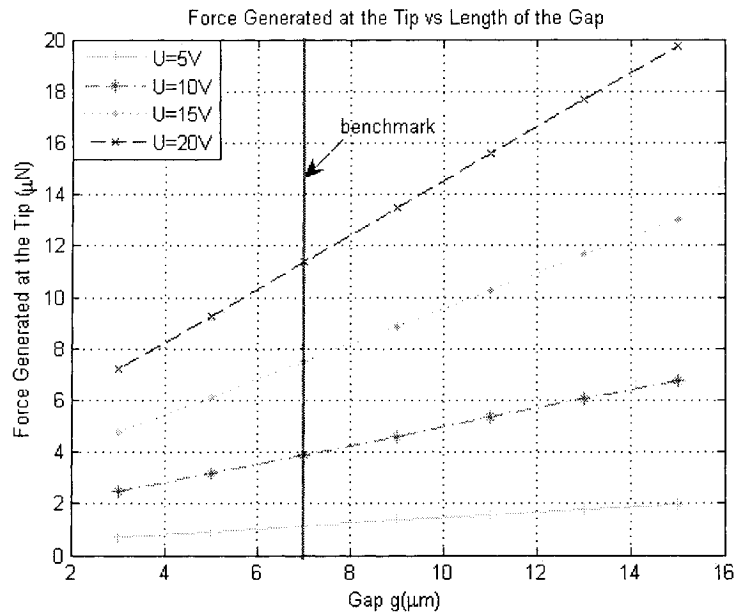Figure 5.37: Stiffness vs length of the gap

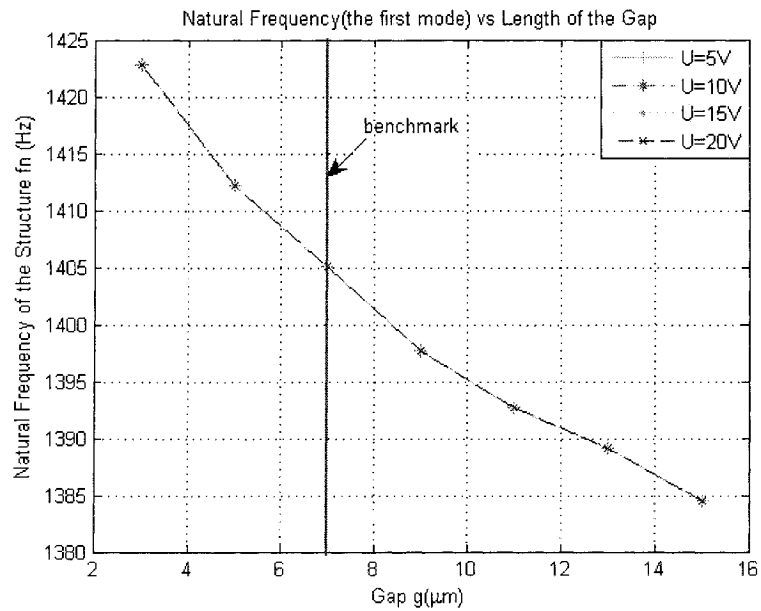Figure 5.38: Force generated at the tip vs length of the gap

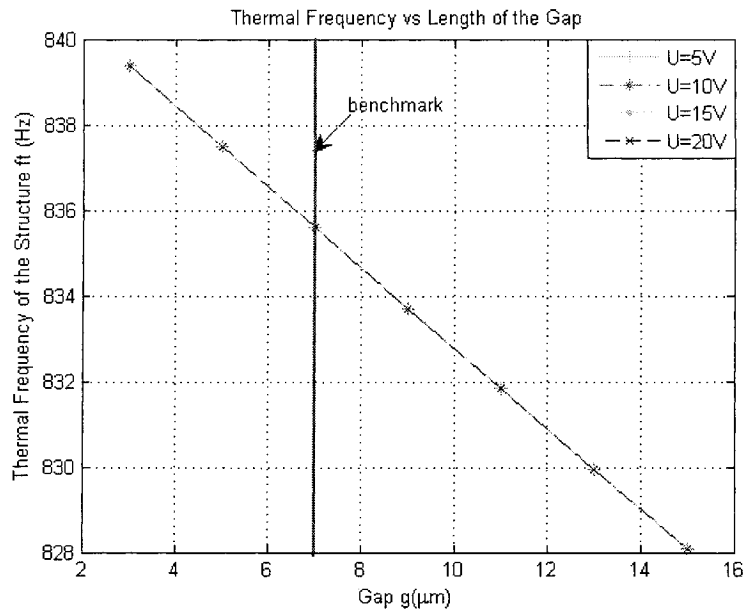Figure 5.39: Natural frequency (the first mode) vs length of the gap

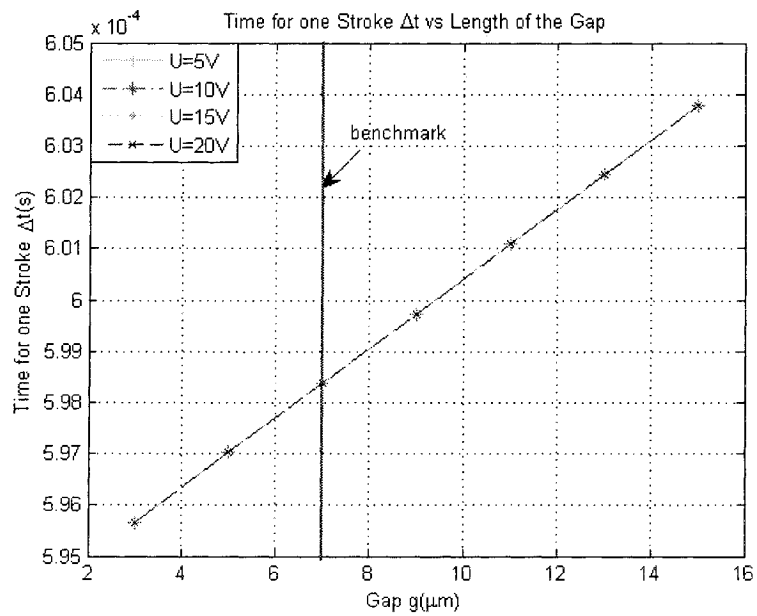Figure 5.40: Thermal frequency vs length of the gap

Figure 5.41: Time for one stroke Δt vs length of the gap
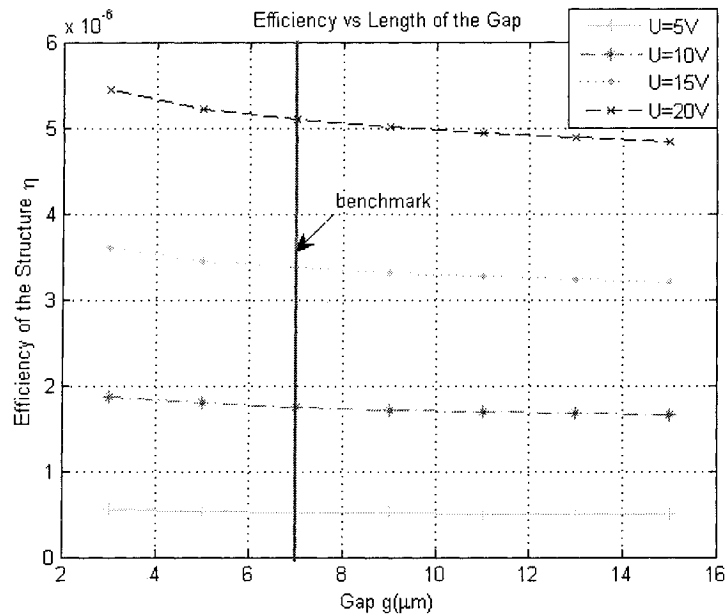
Figure 5.42: Efficiency vs length of the gap

The third group simulation studies the gap's influence on the performance of the thermal actuators. The study here is based on the situation that just considers the width of the gap g as variable, with other geometric parameters constant at the values specified in Table 2.1.

A change in gap g does not cause significant influence on the thermal volume, electrical resistance, as well as the input energy rate, and hence the coefficient λ. Those performance quantities remain almost constant (as from 2.2, 2.3, 2.10, and Figure 5.31, 5.32, 5.33). As all those factors affect temperature distributions, the average temperature and the maximum temperature are seen to be almost constant too (as from 2.13 and Figure 5.34, 5.35).

Though gap g change does not cause much influence on thermal performance, it influences significantly the mechanical performance. From Figure 5.36, one can see

that the structure with wider gap causes reduced deflection at the tip. Wider gap causes larger moment of inertia (as from 3.36) and hence larger stiffness (as from 3.34 and Figure 5.37). Larger stiffness vs. lower deflection result in increased force generated at the tip (as from 3.37 and Figure 5.38). For natural frequency and thermal frequency, Figure 5.39 and 5.40 show that they are both in a declining trend with gap g increase, but from the number, one can see, they both insignificantly change. Duration of one cycle increases just a little with the gap g increase. Finally, the efficiency, with the influence of stiffness' increase and deflection decreases a little with the gap increase.

5.5.4 The Width of Hot Arm W_h is Variable as well as the Width of the Flexure W_f ($W_h=W_f$) while others are Constant – Table 5.2 Line 4
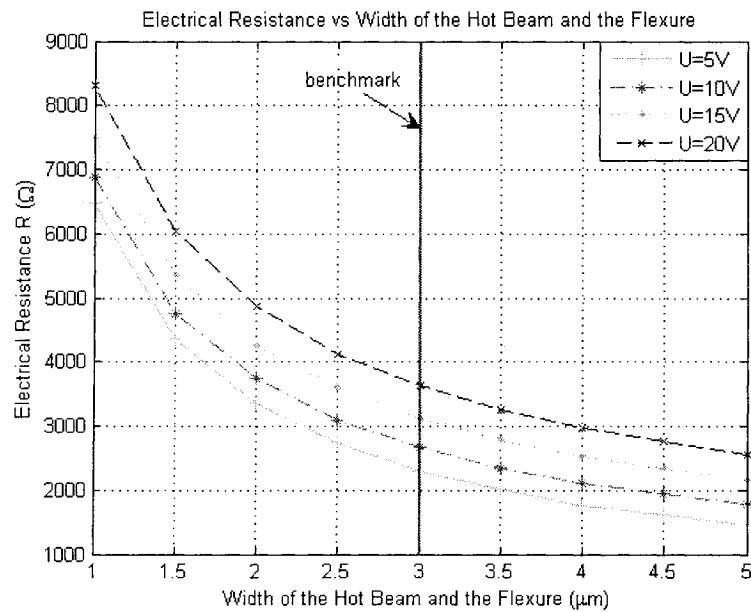
Figure 5.43: Electrical resistance vs width of the hot beam and the flexure

127
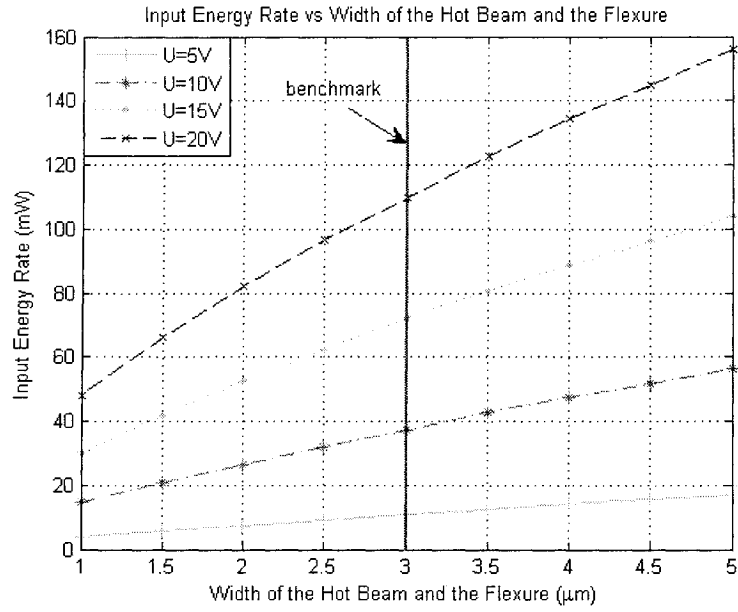
Figure 5.44: Input energy vs width of the hot beam and the flexure
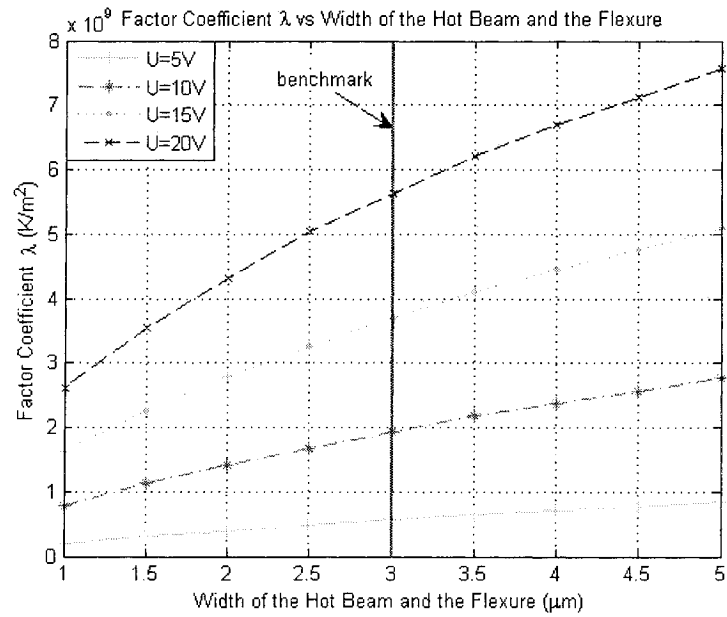
Figure 5.45: Factor coefficient λ vs width of the hot beam and the flexure

128
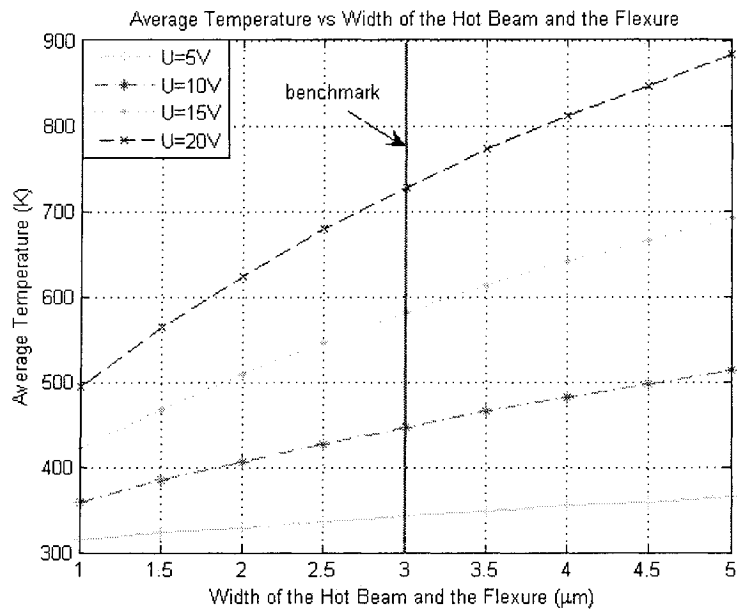
Figure 5.46: Average temperature vs width of the hot beam and the flexure
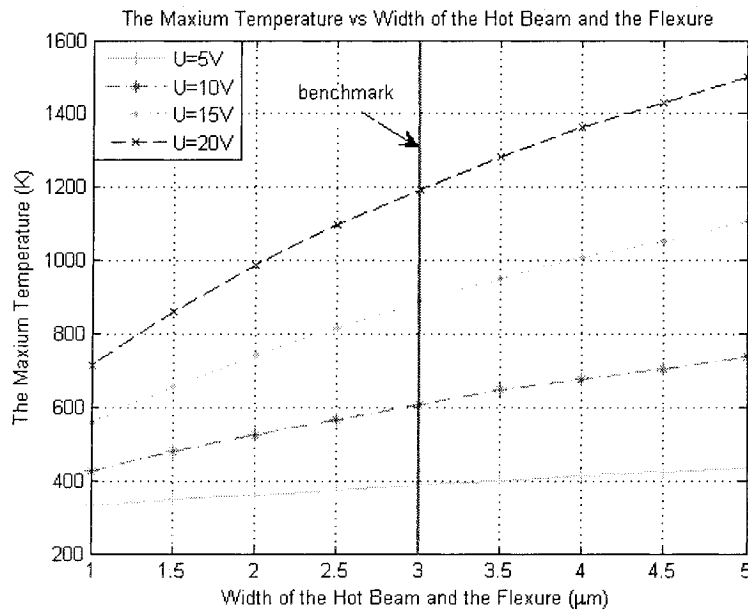
Figure 5.47: The maximum temperature vs width of the hot beam and the flexure
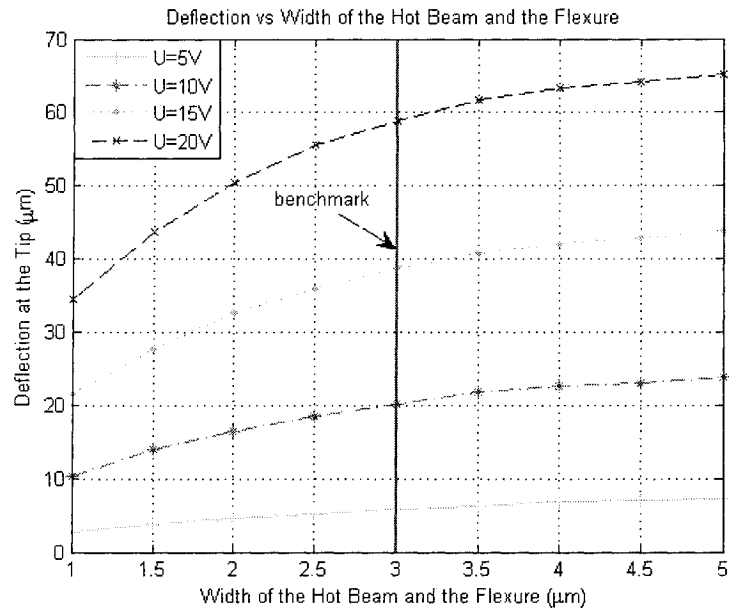
Figure 5.48: Deflection vs width of the hot beam and the flexure

Figure 5.49: Stiffness vs width of the hot beam and the flexure

130
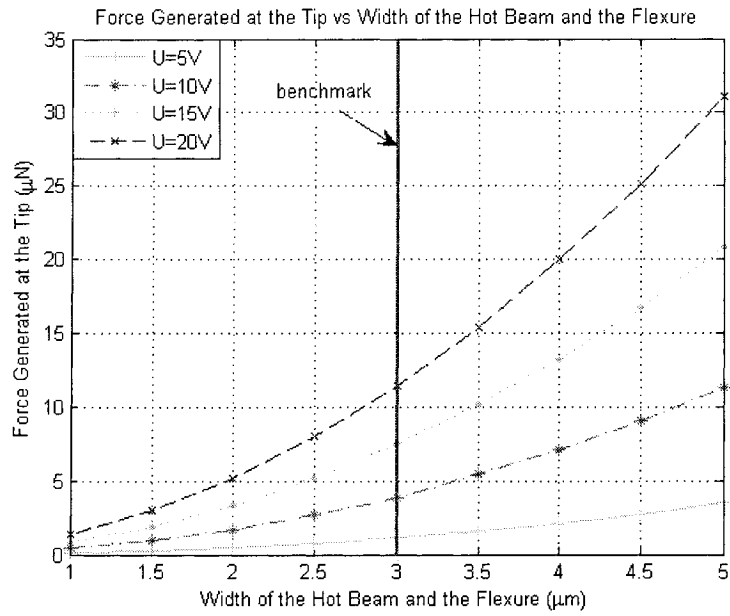
Figure 5.50: Force generated at the tip vs width of the hot beam and the flexure
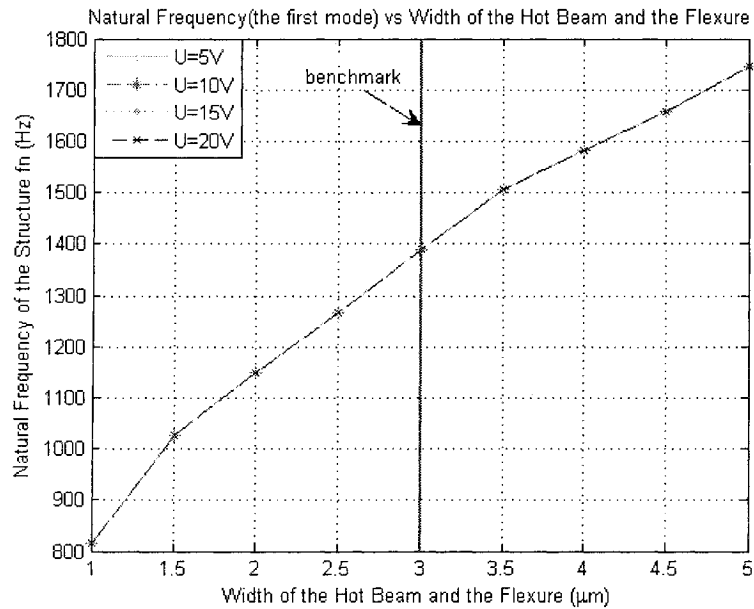
Figure 5.51: Natural frequency (the first mode) vs width of the hot beam and the flexure

131
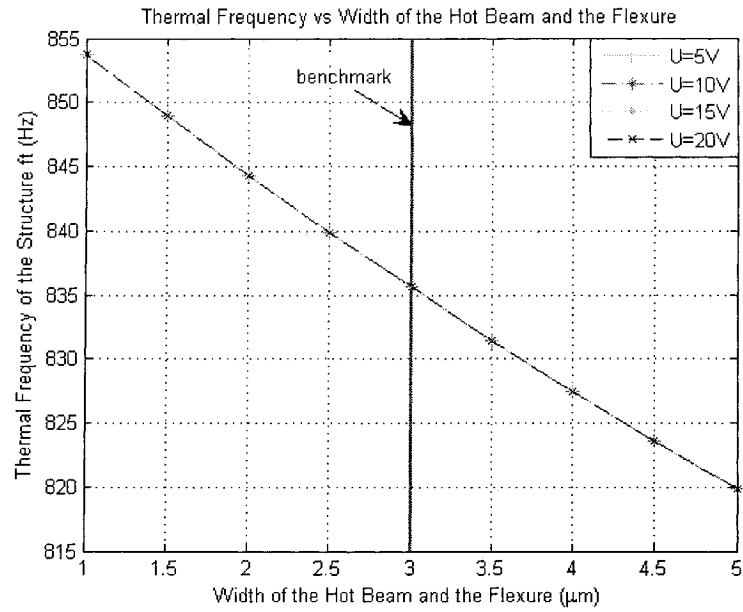
Figure 5.52: Thermal frequency vs width of the hot beam and the flexure
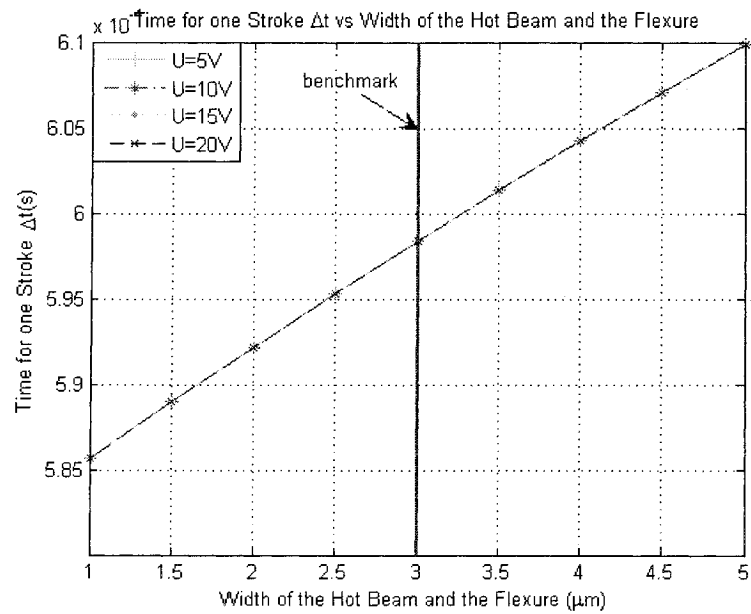
Figure 5.53: Time for one stroke Δt vs width of the hot beam and the flexure

132
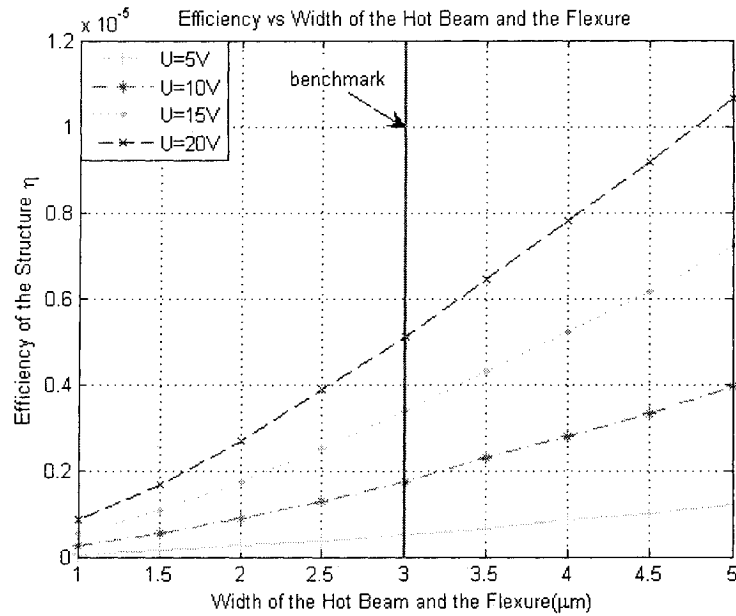
Figure 5.54: Efficiency vs width of the hot beam and the flexure

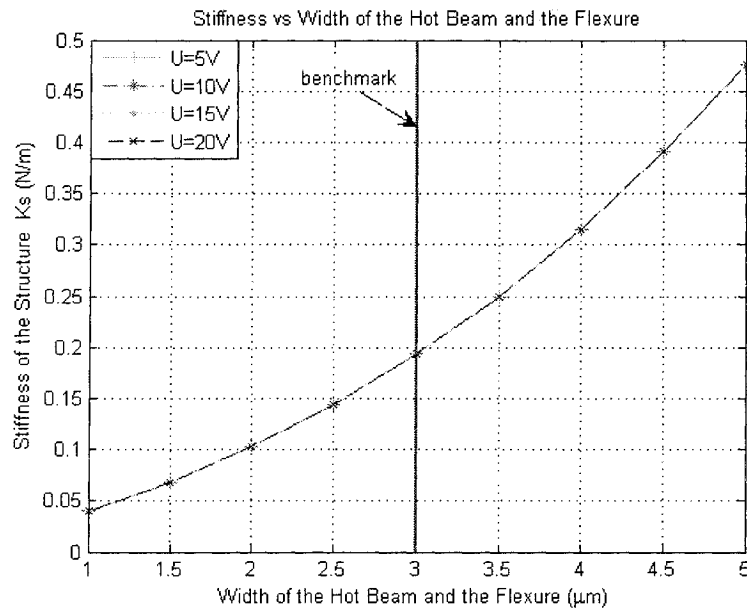The fourth group simulations in carried out to study the influence of the width of the hot beam W_h on thermal and mechanical performances of the thermal actuators. The variation in geometric parameters in this group are limited to the width of hot arm W_h, and the width of the flexure W_f. In this thesis $W_h=W_f$. Other geometric parameters are the same as those in Table 2.1.

When W_h is increasing the thermal volume of the thermal actuator V increases and the electrical resistance decreases (as from 2.2 and Figure 5.43). Under the same electrical potential, the input energy rate E_g, the function of electrical resistance, increases with the W_h increase (as from 2.3 and Figure 5.44). The factor coefficient λ increases with W_h increase (as from 2.10 and Figure 5.45). As temperature distribution on the structure is determined by λ (as from 2.13), Figure 5.46 and 5.47 show that both average temperature and the maximum temperature increase with W_h

133

increase. The increasing temperature causes more thermal expansion and hence an increase in the deflection at the tip (as from Figure 5.48). The moment of inertia I increases with W_h rise (as from 3.35) and then the increase in stiffness of the structure (as from 3.34 and Figure 5.49). With the increase in deflection and stiffness for W_h increase, force generated at the tip increases (as from 3.37 and Figure 5.50). Natural frequency increases significantly, while thermal frequency drops just a little, and so the duration of a cycle increases a little with W_h increase. The efficiency of the structure increases after balance the increase of the stiffness, the deflection, the input energy rate, and the duration of a cycle.

5.5.5 The Width of Cold Arm W_c is Variable while others are Constant – Table 5.2 Line 5
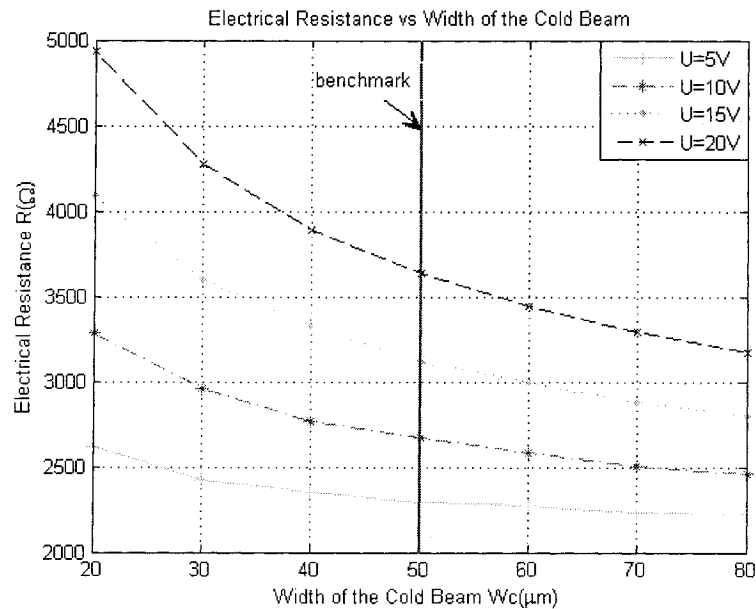
Figure 5.55: Electrical resistance vs width of the cold beam

134
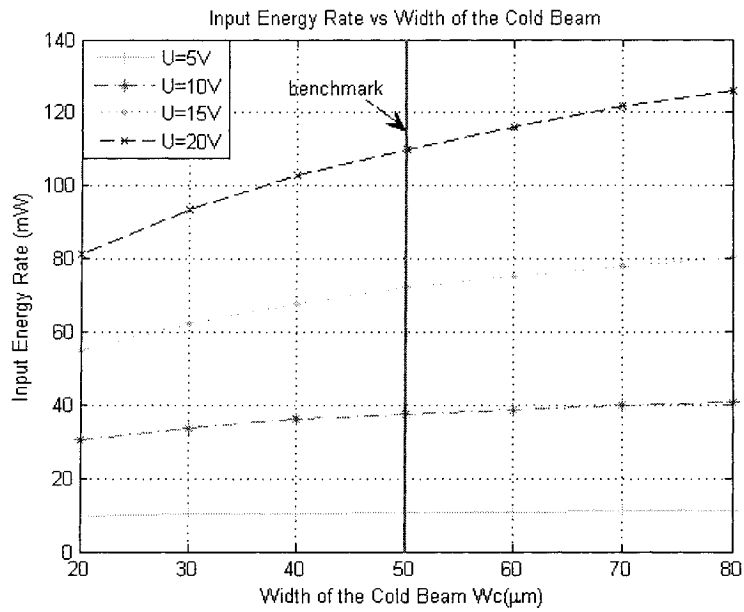
Figure 5.56: Input energy rate vs width of the cold beam
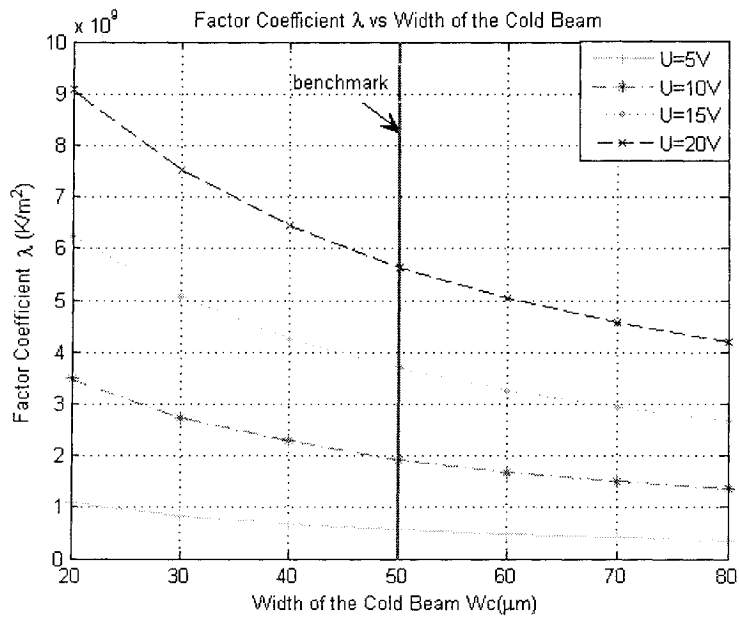
Figure 5.57: Factor coefficient λ vs width of the cold beam
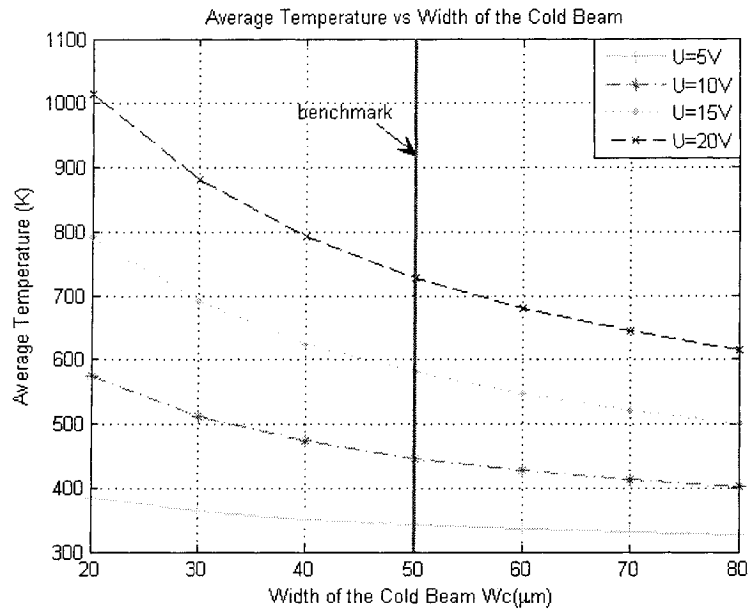
Figure 5.58: Average temperature vs width of the cold beam
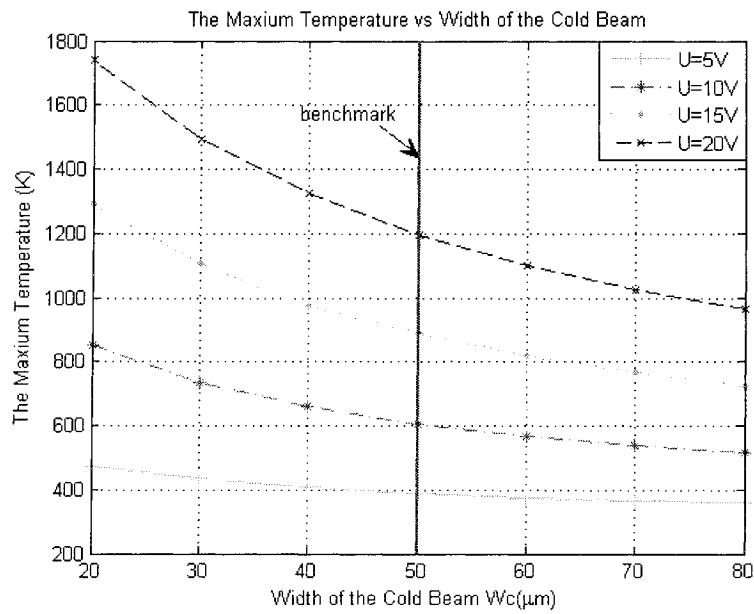
Figure 5.59: The maximum temperature vs width of the cold beam
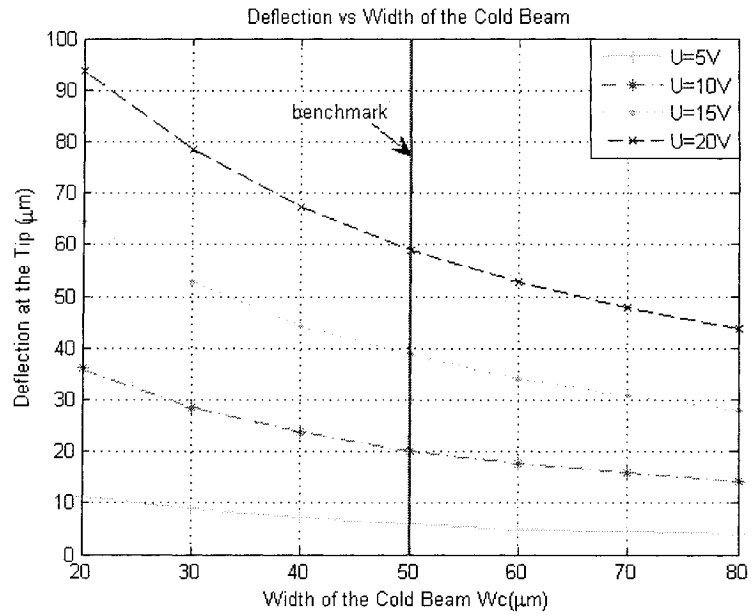
Figure 5.60: Deflection vs width of the cold beam
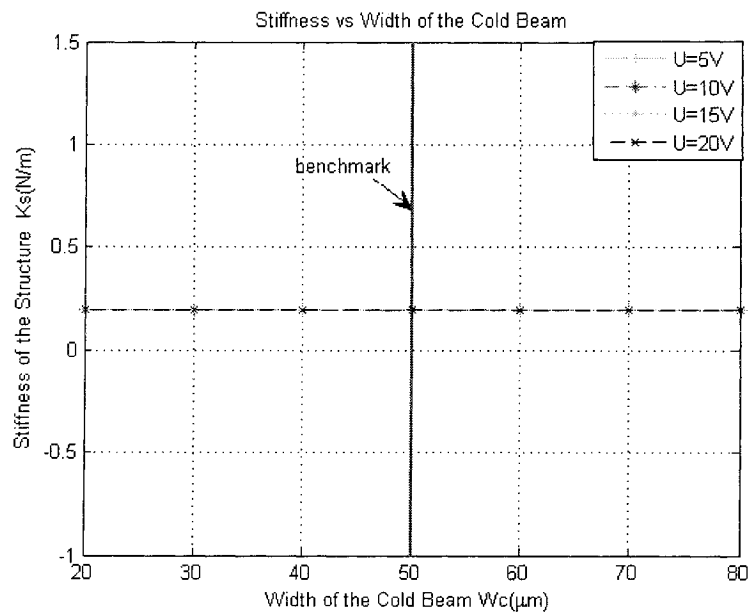
Figure 5.61: Stiffness vs width of the cold beam

137
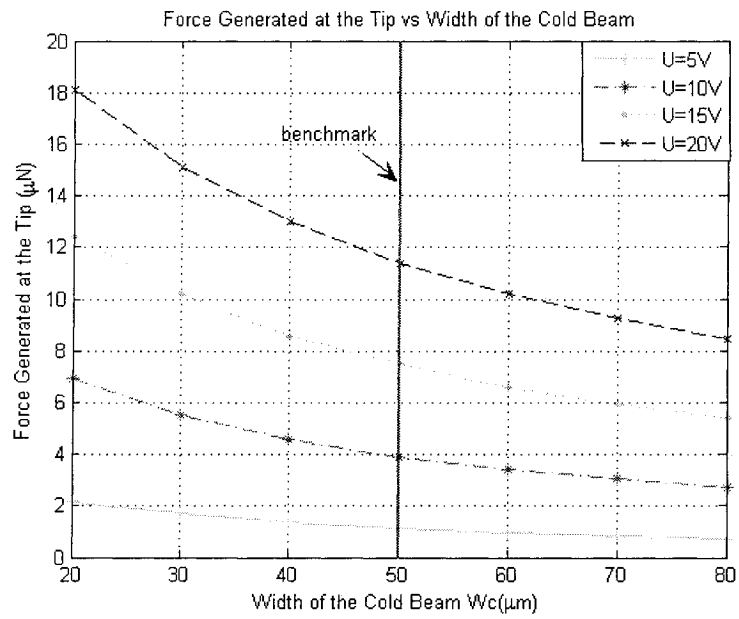
Figure 5.62: Force generated at the tip vs width of the cold beam
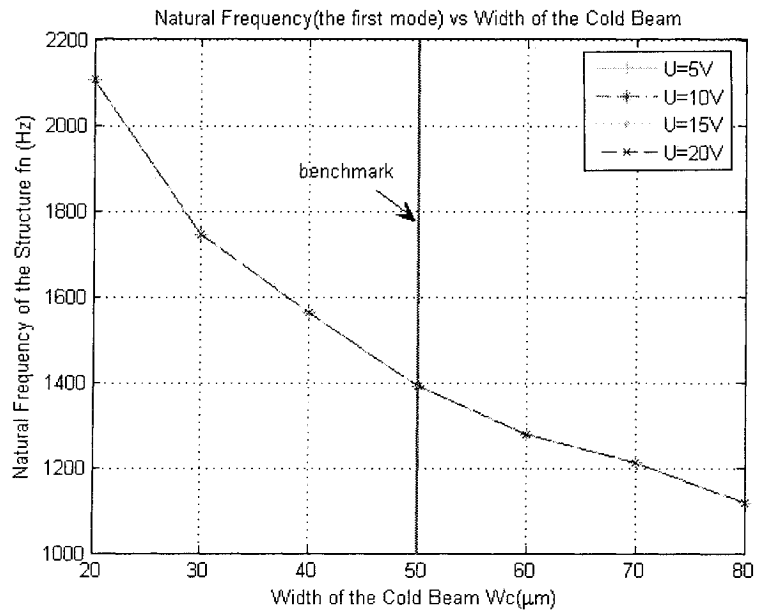
Figure 5.63: Natural frequency (the first mode) vs width of the cold beam
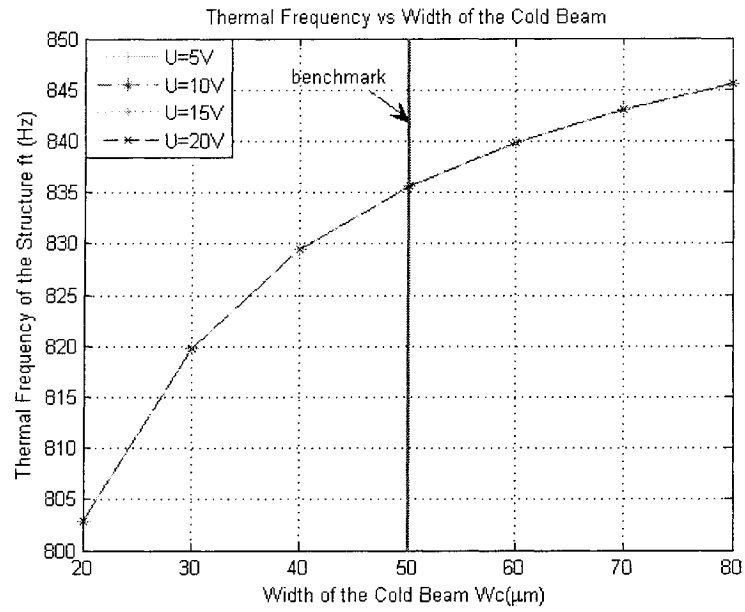
Figure 5.64: Thermal frequency vs width of the cold beam
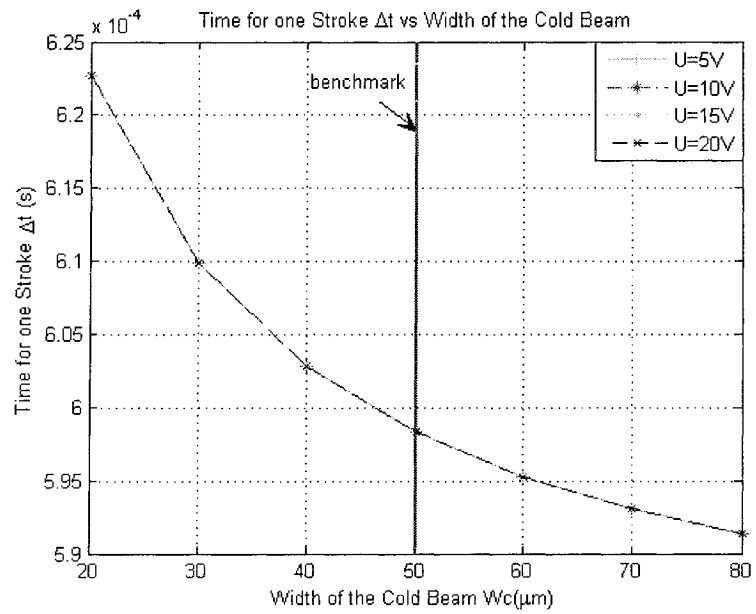
Figure 5.65: Time for one stroke Δt vs width of the cold beam

139
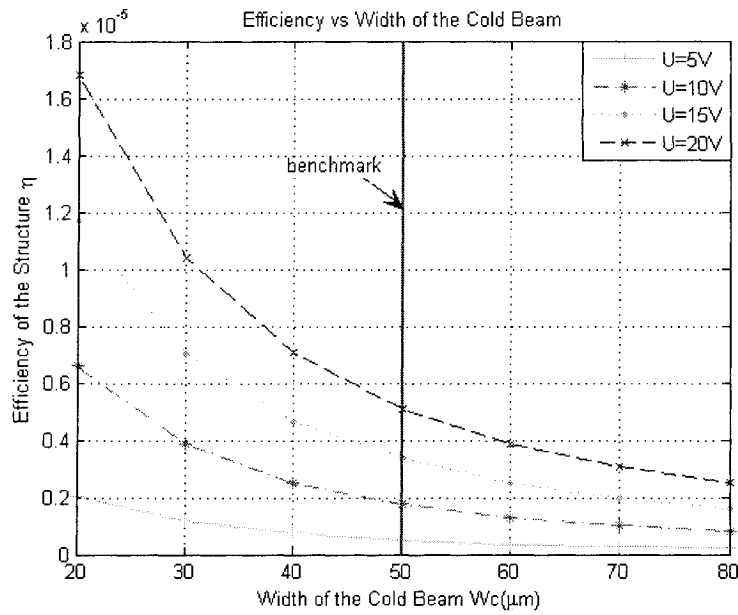
Figure 5.66: Efficiency vs width of the cold beam

The fifth group of simulations are carried out assuming the width of the cold arm W_c as variable while other geometric parameters are the same as those in Table 2.1.

From the geometric study, it appears that the increase of W_c will increase the thermal volume. Electrical resistance decreases with W_c increase (as from 2.2 and Figure 5.55). Hence, the input energy rate E_g increases with W_c increase, because it is the function of electrical resistance when a constant electrical potential applied on (as from 2.3 and Figure 5.56). The coefficient λ, which is in the direct ratio to the input energy and in an inverse ratio to the thermal volume at the same time, decreases when W_c increases (as from 2.10 and Figure 5.57). Temperature distribution, which is influenced by λ, decreases when W_c increases (as from 2.13). Meanwhile, the average temperature and the maximum temperature both decrease when W_c increases (as from Figure 5.58, 5.59). With W_c's increase, the moment of inertia for cold arm increases,

140

so the deflection at the tip decrease (as from Figure 5.60). The stiffness of the structure, on the basis of the assumptions made in Chapter 3.3 does not change with W_c. The force generated at the tip decreases with the increase of W_c a function of the deflection at the tip (as from 3.37 and Figure 5.62). Since the reduction in width is associated with enhanced force and since it is known that when $W_c = W_h$, no displacement and therefore, no force occurs. An optimum ratio, however, will require a remodeling of the thermal actuator in which the thermal management issue be addressed of a more accurate fashion. Due to the larger mass of the structure, natural frequency drops significantly for the wider cold arm (as from Figure 5.63). Thermal frequency increases not significantly with W_c increase (as from Figure 5.64). As the input energy increases and the deflection decreases, the efficiency of this structure decreases.

5.5.6 The Thickness of Structure h is Variable while others are Constant
– Table 5.2 Line 6
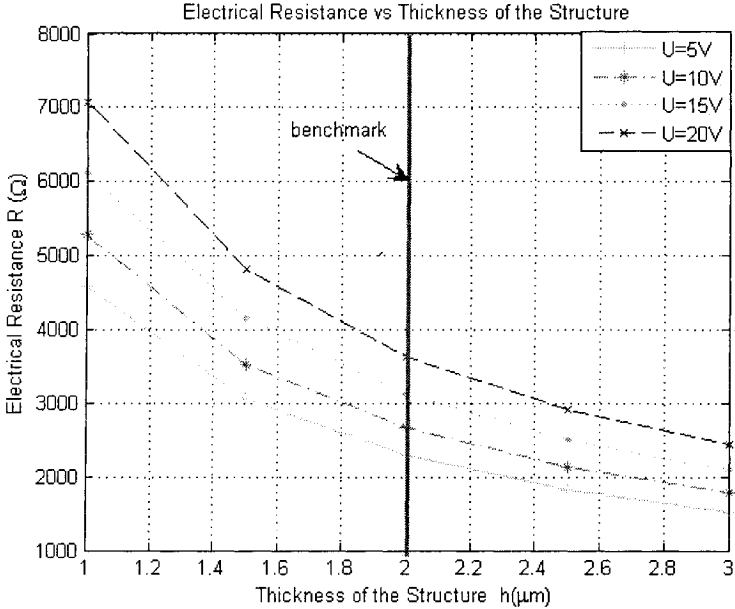
Figure 5.67: Electrical resistance vs thickness of the structure
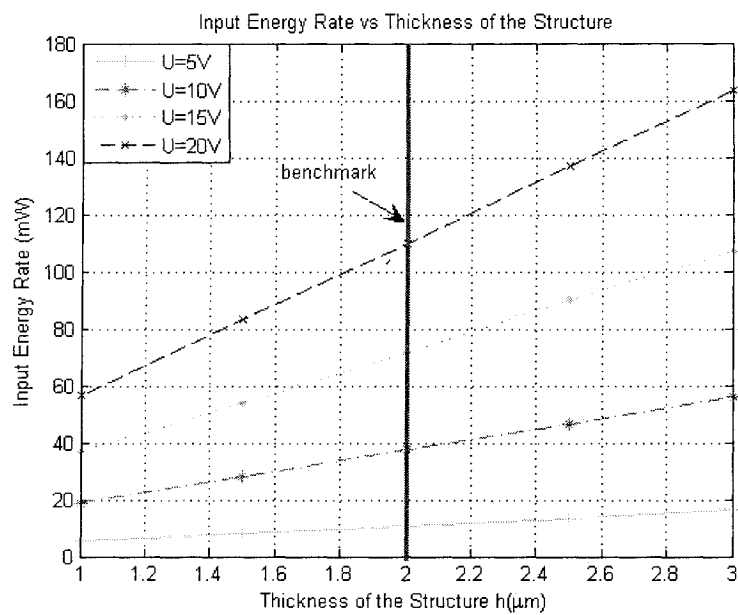
Figure 5.68: Input energy rate vs thickness of the structure
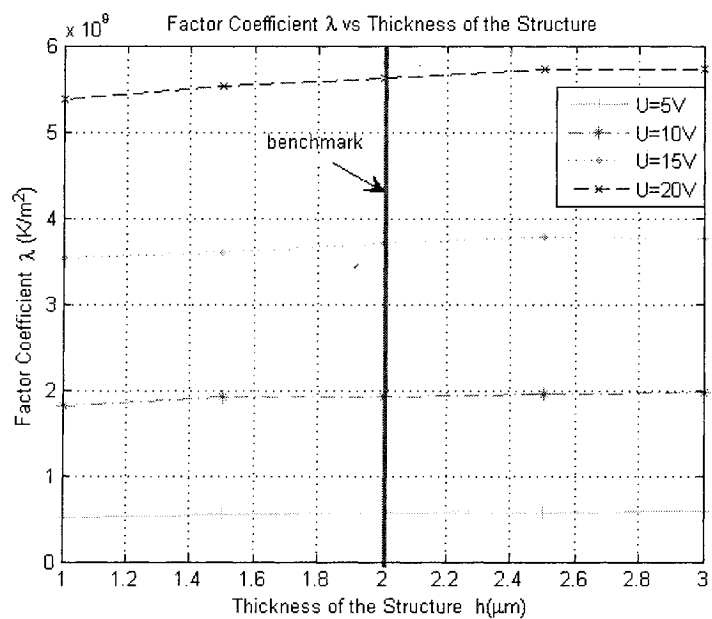
Figure 5.69: Factor coefficient λ vs thickness of the structure

142
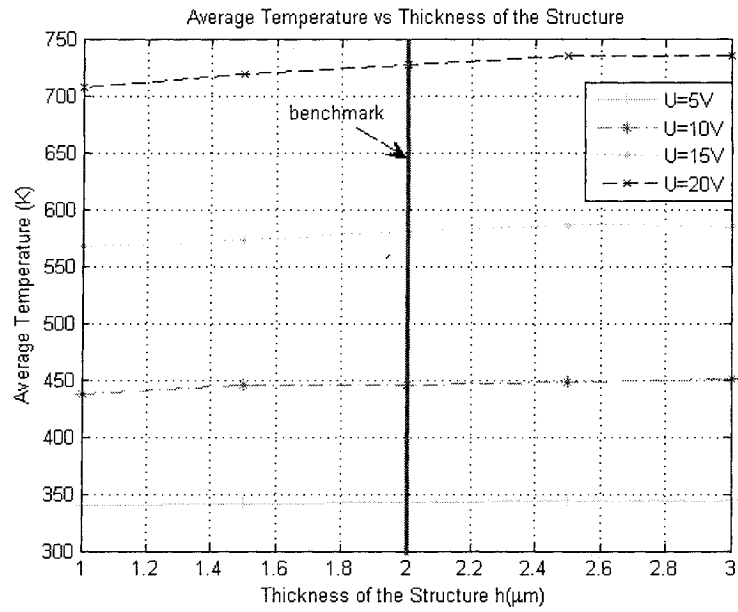
Figure 5.70: Average temperature vs thickness of the structure
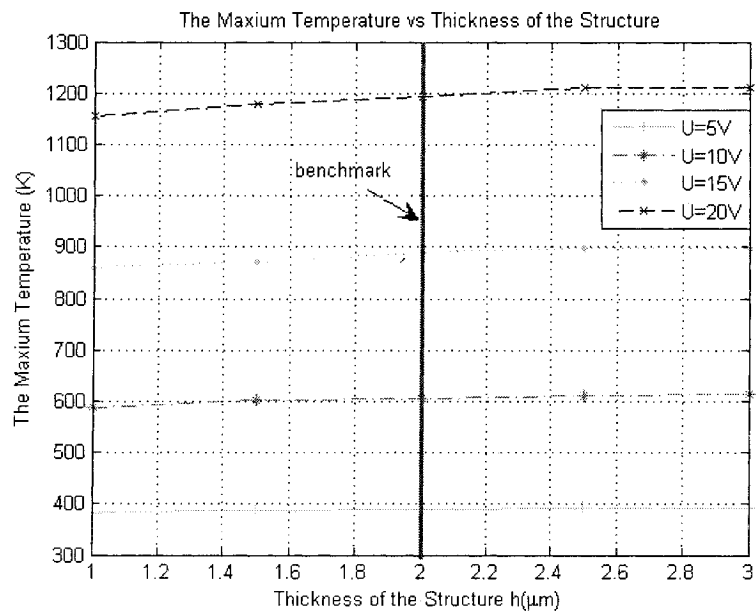
Figure 5.71: The maximum temperature vs thickness of the structure

143
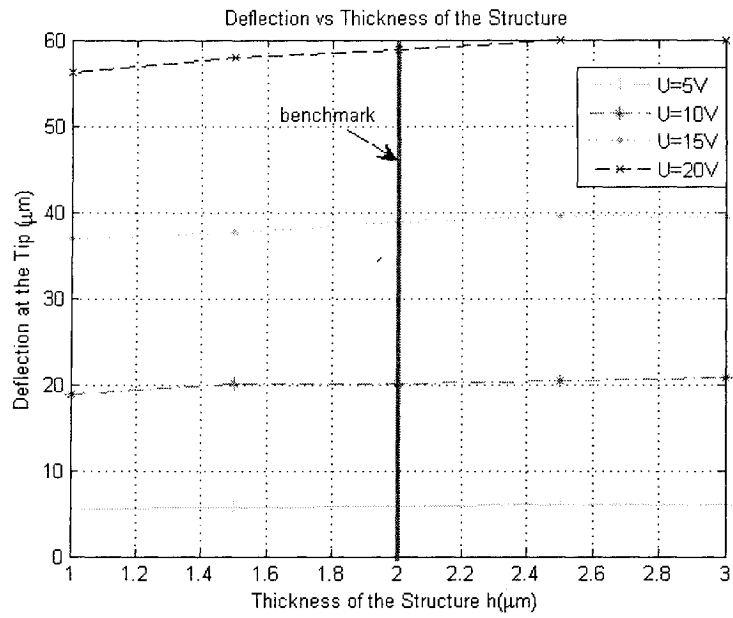
Figure 5.72: Deflection vs thickness of the structure
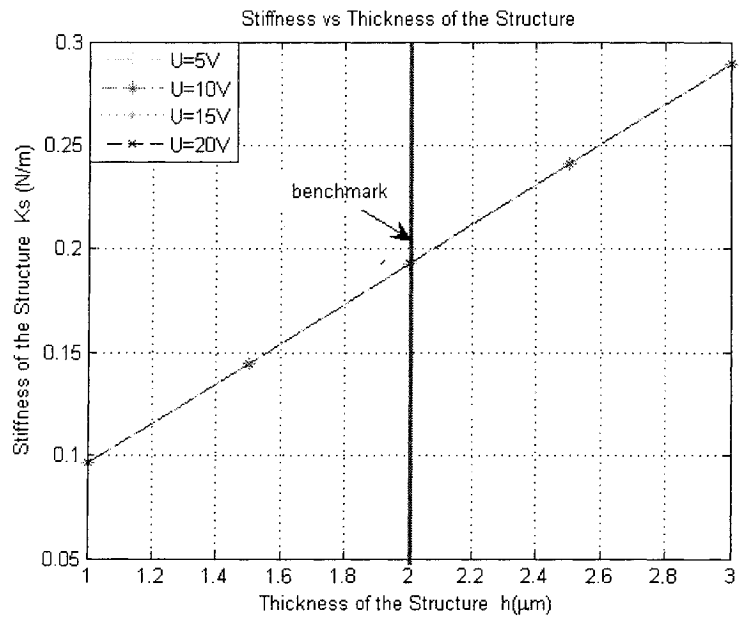
Figure 5.73: Stiffness vs thickness of the structure
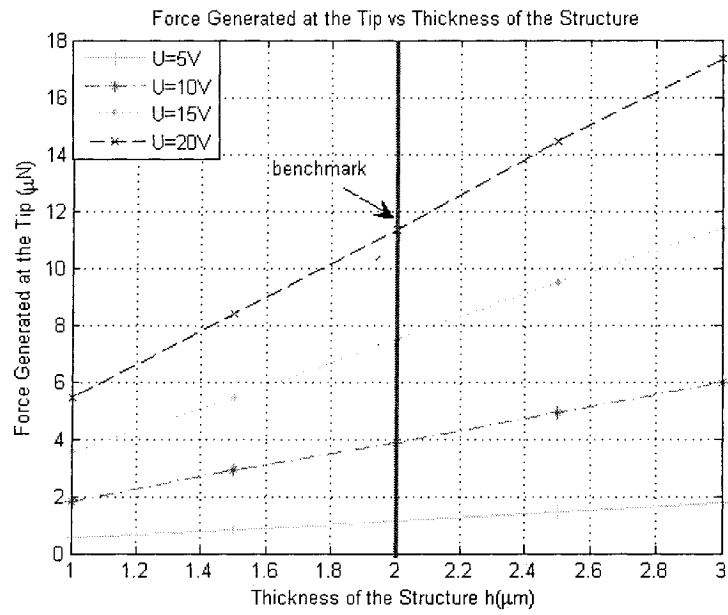
Figure 5.74: Force generated at the tip vs thickness of the structure
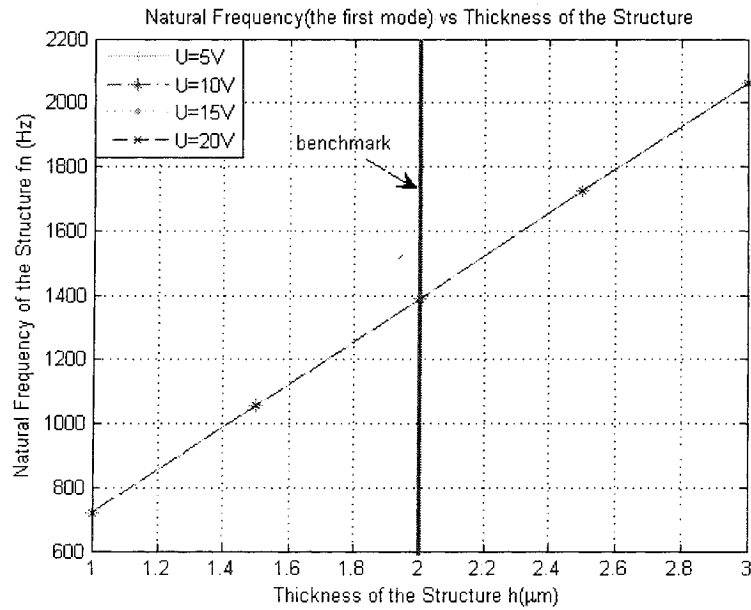
Figure 5.75: Natural frequency (the first mode) vs thickness of the structure

145
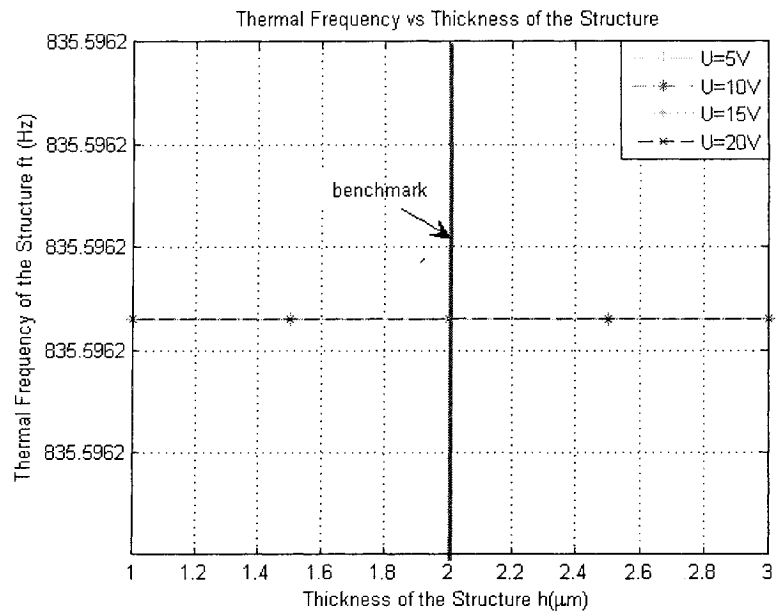
Figure 5.76: Thermal frequency vs thickness of the structure
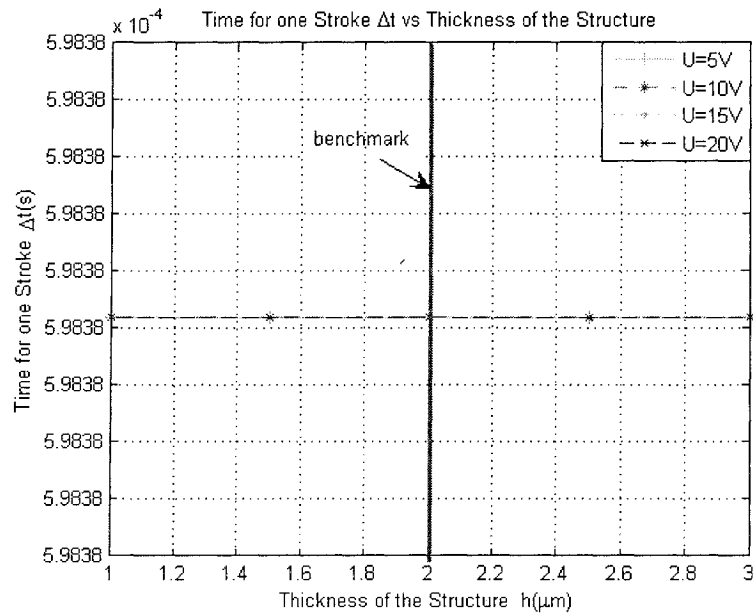
Figure 5.77: Time for one stroke Δt vs thickness of the structure

146
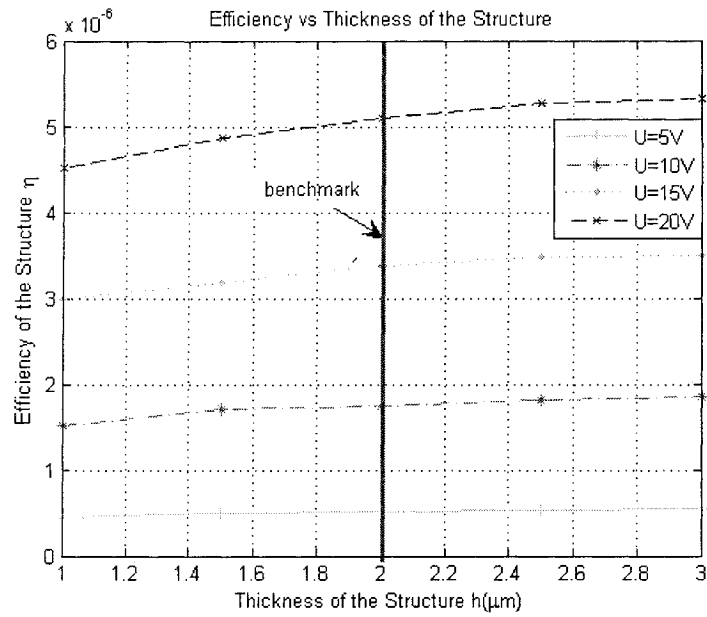
Figure 5.78: Efficiency vs thickness of the structure

This set of simulations has been carried out to study the influence on physical quantities due to the thickness variation h of the structure, as in the process of manufacture, over etching or less etching might happen. This group of simulation is based on considering h as variable; other geometric parameters are the same as those in Table 2.1.

The increasing of h will yield an increase of the thermal volume of the thermal actuator. Electrical resistance decreases with h increase (as from 2.2 and Figure 5.67), and it influences the input energy rate to increase (as from 2.3 and Figure 5.68). The coefficient λ changes, under effect of input energy rate and thermal volume slightly increases with h increase. Therefore, the temperature changes are not significant with the h change (as from Figure 5.70, 5.71).

147

Because there is not much change in temperature, the deflection at the tip, which is caused by asymmetric thermal expansion, does not increase significantly with the influence of h. (as from Figure 5.72). The moment of inertia is influenced directly by h (as from 3.35), and so does the stiffness (as from 3.34 and Figure 5.73). The force generated at the tip increases with the increase of the thickness because of the stiffness change (as from 3.37 and Figure 5.74). Figure 5.75 illustrates that the natural frequency increases linearly with h increase. The thermal frequency does not change for different h (as from Figure 5.76). The efficiency increases with the increase of h, under the influence of input energy increase and stiffness increase (as from 3.47 and Figure 5.78).

Table 5.3 Design general recommendations: the trend of the main physical quantities with the increase of the geometric features

Physical quantity	L	L_f	g	$W_h{=}W_f$	W_c	h
Electrical resistance R	↑	↑	↔	↓	↓	↓
Input energy rate E_g	↓	↓	↔	↑	↑	↑
Factor coefficient λ	↓	↓	↔	↑	↓	↗
Average temperature $\overline{T}_{av}$	↓	↑	↔	↑	↓	↗
Maximum temperature T_{max}	↘	↗	↔	↑	↓	↗
Deflection at the tip d	↑	↓	↓	↑	↓	↗
Stiffness K_s	↓	↔	↑	↑	↔	↑
Force generated at the tip F	↘	↓	↑	↑	↓	↑
Resonant natural frequency f_n	↓	↓	↓	↑	↓	↑
Thermal frequency f_t	↓	↓	↓	↓	↑	↔
Duration for one stroke Δt	↑	↑	↑	↑	↓	↔
Efficiency η	↑	↓	↘	↑	↓	↗

↗: slightly increase   ↘: slightly decrease   ↑: increase   ↓: decrease   ↔: constant

5.6 Summary

From simulation results, the trend of properties changes with geometry variables, and using temperature limitations of polysilicon $T_{melting} \approx 1685K$, and $T_{brittle-to-ductile} \approx 933K$, which is the temperature above which plastic deformation occurs in polysilicon, the safety range can be obtained. Users could select different trade-off designs according to their specific requirements.

CHAPTER 6   CONCLUSIONS

6.1 Summary

An electro-thermal model for polysilicon micro thermal actuators has been developed based on Joule thermal effect and heat dissipation mechanisms. The MUMPs technology has been used and specific benchmark device was proposed. Further, a mechanical model designed to solve problems of force generation, deflection, stress, natural frequency, stiffness, thermal frequency, and efficiency has been built according to the temperature distribution obtained from the electro-thermal model. The results of both models are in good agreement with the results of FEM simulations as well as the experiments.

In Chapter1-introduction and literature review, the micro U-shaped thermal actuator is introduced after compared with other kinds of microactuators and two other types of micro thermal actuators.

Chapter2-electrical and thermal analyses document the principles of functioning of the electro thermal actuator. Further a model is built. In this model, conduction, convection and radiation heat mechanism are considered as the ways in heat dissipation. Results show that the convective heat transfer dissipates about 10% supplied energy, and the radiative heat transfer dissipates about 1% supplied energy, thus most input energy is used to build and then support temperature distribution. Although the results for radiative heat transfer dissipations are small, it is still important and can not be ignored compared with the mechanical efficiency which is less than 0.01%. In this thesis the temperature dependency of the electrical resistivity of polysilicon is taken into account (as from 2.1). The experimental result

validates its accuracy (as from Figure 5.4). Next, the factor coefficient λ, the fundamental coefficient that describes the temperature distribution, is in an inverse proportionally to the volume of structure, which represents one of the main reasons for the thermal and mechanical behavior changes with the geometry. The results of temperature distribution on the thermal actuator from the FEM analysis confirm the assumptions made in the model and the result from the theoretical analysis (as shown in Figure 5.1).

Chapter 3-dynamic characterization analysis addressees the mechanical model for the micro thermal actuator. The virtual work method is used to calculate the deflection. Further, the micro thermal actuator is assumed as a rigid frame subjected to harmonic vibrations. The natural frequency and higher models are found by Rayleigh-Ritz energy method throughout the orthogonal polynomial. Six modes of natural frequency are obtained through this analysis, and the results are in good agreement with the results from the FEM (Table 3.4 and 3.5). The force generated at the tip is calculated as an equivalent force, and expressed via stiffness of the structure. To verify this result, the equivalent forces are applied on the FEM model. The deflections from this FEM analysis are in good agreement with the deflections from the theoretical analysis and experiments (Table 3.6). The conclusions of the stress analysis are that the maximum stress occurs at the point where the cold arm connected with the gap arm, and this result is in good agreement with the FEM analysis (Table 3.7 and 3.8). After comparing the stress under thermo-electrical effect (applied voltage), with that under force effect (applied equivalent force), an interesting result is found, which is that the stress under thermal electrical effect is significantly less than the stress under force effect. This phenomenon could be explained through the increased compliance of the structure under high temperature condition. The thermal frequency and stiffness of the structure are all inherent properties of the structure; therefore they can only be described as functions of

geometries. Finally, efficiency studies show that this kind of micro thermal actuator is extremely inefficient from energy conversion point of view.

Chapter 4-fabrication process and experiment validation is the experimental confirmation of the analytical models built in this thesis. In this chapter, the experimental setup, the test procedure and the results are documented. With the help of the pictures, taken under the microscope, the following phenomena are described: the initial movement of the structure, the maximum deflection, which part of the structure expands most, the position of burn point. The experimental results agree with the assumptions of the analytical model, and with the results from it as well.

On the basis of the analytical model developed in this thesis, in Chapter 5-simulations and the parametric studies focusing on the comparisons among the theoretical, FEM and experimental results; and the mechanical and thermal behaviors of U-shaped micro thermal actuators are made under different geometries assumptions. From these figures, the relations between geometries of the micro thermal actuators with their characterizations are clearly shown. These figures make it possible for designers or users to make different effective trade-offs according to specific requirements, or to evaluate the safety of their designs.

6.2 Conclusions

1. An analytical model that includes the thermal and the mechanical performance of a U-shaped micro thermal actuator is proposed. The joule effect heat is assumed being dissipated through conduction, convection, and radiation. The overall efficiency of each dissipative mechanism was theoretically established.

2. The energy balance principle was used to relate the deflection of the U-shaped micro thermal actuator to the thermal dissipated energy. The virtual work method

has been employed to calculate the deflection. Validations through experimental and FEM were carried out. All the results are in good agreement.

3. The dynamic performance natural frequency of the U-shaped micro thermal actuator was analytically evaluated using Rayleigh-Ritz method into orthogonal polynomials. FEM model was used to validate the natural frequency of the benchmark thermal actuator.

4. Some dynamic properties are the first analyzed and reported in this thesis according to the best knowledge of the author, such as the stiffness, the equivalent force generated at the tip, stress analysis of this kind of thermal actuator, duration of the motion, and the efficiency. The stress analysis and the equivalent force were validated by FEM through multi-physics model and mechanical model respectively. Results show that they are both verified.

5. The micro thermal actuators have been fabricated using MUMPs process. The structures well tested under variable input voltage to measure the current and the deflection, and so as the resistance, the input power, and the efficiency. The results of the test are in good agreement with the analytical results.

6. A parametric study was carried out to evaluate the performances of the U-shaped thermal actuators with respect to the geometric features of a benchmark device. The trend of the performances of the thermal microactuator is indicated with respect to the variation of a single geometric feature only. This work is providing the designer with the quantitative influence of a specific geometric feature to the specific performance criteria.

7. Since all the comprehensive models available in the operated literature are limited to either thermal or mechanical model. The proposed analytical model links the

153

electrical, thermal and mechanical properties of the U-shaped thermal microactuator in a unique formulation.

8. In order to design the thermal actuators for some specific applications, the proposed model is instrumental to the designers. The analytical model could be also used to evaluate the performance of a specific imposed configuration. The model could also be used to fine-tune to design to optimally perform with respect to the specific related performance.

6.3 Future work

1. In the future work, in addition to testing the designs of different geometries, the resonant frequency of the structures needs to be measured, for validation purpose and the long-term reliability of U-shaped micro thermal actuators needs to be determined by using periodic drive voltages (square ware drive signal), since failure and displacement decrease might happen after certain number of cycles.

2. A more accurate analytical model to include the friction of the dimples on the substrate and the non-linear mechanical deflection of the structure would improve the accuracy of prediction mainly under very low and very high voltage.

3. The structure could be used to evaluate the creep properties of polysilicon, as the evaluation that is not available anywhere in the literature.

4. The more accurate analytical model in conjunction with the experimental results could yield good estimate of the *Si* softening creep, a reported problem that occurs in polysilicon for temperature exceeding 300°C. This type of evaluation would be extremely useful to evaluate the limits at which *Si* structure could junction.

5. Extension of the test to the temperature gradient measurement using Infra Red Camera.

REFERENCES

[1] H. Fujita, "Microactuators and Micromachines", Proceedings of the IEEE, VOL.86, NO. 8, August 1998.

[2] K. E. Petersen, "Silicon as a Mechanical Material", 0018-9219/82/0500-0420 ©1982 IEEE.

[3] R. T. Howe and R. S. Muller, "Polycrystalline Silicon Micromechanical Beams", in spring meeting of the electrochemical society, Montreal, Canada, Extended abstracts 82-1, May 9-14, 1982.

[4] R. T. Howe and R. S. Muller, "Resonant Microbridge Vapor sensor", IEEE Trans. Electr. Devices, ED-33, pp. 499-507, 1986.

[5] J. H. Comtois and V. M. Bright, "Applications for Surface-micromachined Polysilicon Thermal Actuators and Arrays", Sensor and Actuators: A 58 pp.19-25,1997.

[6] T. R. Hsu, "MEMS & Microsystems Design and Manufacture", Boston: McGraw-Hill, 2002.

[7] H. Toshiyoshi, M. Mita, and H. Fujita, "A MEMS Piggyback Actuator for Hard-Disk Drives", J.MEMS, Vol. 11, NO.6, 1057-7157, 2002.

[8] M. Mita, H. Toshiyoshi, K. Kakushima, G. Hashiguchi, D. Kobayashi, J. Endo, Y. Wada, and H. Fujita, "Characterization of Bulk Micromachined Tunneling Tip Integrated with Positioning Actuator", IEEE 0-7803-7185-2, 2002.

[9] P. E. Kladitis, V. M. Bright, K. F. Harsh, and Y. C. Lee, "Prototype Microrobots For Micro Positioning in a Manufacturing Process and Micro Unmanned Vehicles". Proceedings of the 1999 IEEE International Conference on Microelectromechnical Systems (MEMS1999), Orlando FL, pp.570-575, January 17-21, 1990.

[10] W. Riethmuller, W. Benecke, "Thermally Excited Silicon Microactuators", IEEE Trans. Electron Devices 35(6) pp.758-763, 1988.

[11] H. Baltes, D. Moser, R. Lenggenhanger, O. Brand, G. Waschutka, "Thermomecanical Microtransducers by CMOS Technology Combined with Micromachining", Micro System Technologies '91, 2nd Imt. Conf. Micro, Electro, Opto, Mechanic Systems and Components, Berlinm, Oct.29-Nov. 1, pp.98-103, 1991.

[12] G. Greitmann, R. A. Buser, "Tactile Microgripper for Automated Handling of Microparts", Sensors and Actuators: A Physical, Vol. 2: pp.372-375, June 1995.

[13] R. A. Buser, N. F. de Rooij, "Biaxial Scanning Mirrors Activated by Bimorph Structures for Medical Applications", Sensors and Actuators: A 31 pp. 29-34, 1992.

[14] S. Schweizer, S. Calmes, M. Laudon, Ph. Renaud, "Thermally Actuated Optical Microscanner with Large Angle and Low Consumption", Sensors and Actuators: 76 pp. 470-477, 1999.

[15] A. Tuantranont and V. M. Bright, "Micromachined Thermal Multimorph Actuators Fabricated by Multi-Users MEMS Process", IEEE 0-7803-7657-9, 2002.

[16] L. Que, J. –S. Park, and Y. B. Gianchandani, "Bent-beam Electro-Thermal Actuators for High Force Applications", IEEE 0-7803-5194, 1999.

[17] L. L. Chu, J. A. Hetrick, Y. B. Gianchandani, "High Amplification Compliant Microtransmissions for Rectilinear Electrothermal Actuators", Sensors and Actuators: A 97-98 pp. 776-783, 2002.

[18] J. H. Comtois, M. A. Michalicek and C. C. Barron, "Characterization of Electrothermal Actuators and Arrays Fabricated in a Four-level, Planarized Surface-Micromachined Polycrystalline Silicon Process", Sensors and Actuators: A 70 pp.23-31, 1998.

[19] P. Lerch, C. K. Slimane, B. Romanowicz and P. Renaud, "Modelization and Characterization of Asymmetrical Thermal Microacuators", J. Micromech. Microeng. 6 134-7, 1996.

[20] L. Lin, M. Chiao, "Electrothermal Responses of Lineshape Microstructures", Sensor and Actuators: A 55 pp.35-41, 1996.

[21] J. Jonsmann, O. Sigmund, S. Bouwstra, "Compliant Electro-Thermal Microactuators", IEEE 0-7803-5194-0, 1999.

[22] T. Moulton, G. K. Ananthasuresh, "Micromechanical Devices with Embedded Electro-Thermal-Compliant Actuation", Sensor and Actuators: A 90 pp. 38-48, 2001.

[23] Q. Huang and N. Ka Shek Lee, "Analysis and Design of polysilicon Thermal Flexure Actuator", J. Micromech. Microeng.9 pp.64-70, 1999.

[24] N. D. Mankame and G. K. Ananthasuresh, "Comprehensive Thermal Modeling and Characterization of an Electro-thermal-compliant Microactuator", J. Micromech. Microeng.11 pp. 452-462, 2001.

[25] L. Liew, V. M. Bright, M. L. Dunn, J. W. Daily and R. Raj, "Development of SiCN Ceramic Actuators", IEEE 0-7803-7185-2, 2002.

[26] A. Shishko, D. Koester, R. Mahedevan and K. Marcus, "Mnlti-User MEMS Process (MUMPs) Introduction and Design Rules", Cronos Integrated Microsystems A JDS Uniphase Company, 3026 Cornwallis Rd. Research Triangle Park, NC 27709, 6th edition, 2001.

[27] S. M. Sze(Ed), "Semiconductor Sensor". ISBN 0-471-54609-7 John Wiley & Sons, Inc, 1994.

[28] R. B. Bhat, "Natural frequencies of rectangular plates using characteristic orthogonal polynomials in Rayleigh-Ritz Method", J. Sound and Vibration, 102(4), pp.493-499, 1985.

[29] R. B. Bhat, "Flexural vibration of polygonal plates using characteristic orthogonal polynomials in two variables", J. Sound and Vibration, 114(1), pp.65-71, 1987.

[30] G. Rinaldi, "An improved method for predicting microfabrication influence in atomic force microscopy performances", J. of Nanotechnology, Vol. 1, No.3, 2003.

[31] W. T. Thomson, and M. D. Dahleh, "Theory of Vibration with Application", 5th edition, Prentice Hall, 1997.

[32] J. R. Welty, C. E. Wicks, R. E. Mlson, "Fundamentals of Momentum, Heat& Mass Transfer", 2nd edition, John Wiley & Sons, ISBN 0-471-93354-6, 1976.

[33] J. B. Kennedy and M. K. S. Madugula, "Elastic analysis of Structures", New York: Harper and Row, 1990.

[34] J. Mark Noworolski, E. H. Klaassen, J. R. Logan, K. E. Petersen, and N. I. Maluf, "Process for In-plane and Out-of–plane Single-crystal-silicon Thermal Microactuators", Sensor and Actuators: A 55 pp. 65-69, 1996.

[35] L. Lin and S.-H. Lin, "Vertically Driven Microactuators by Electrothermal Bulking Effects", Sensor and Actuators: A 71 pp. 35-39, 1998.

[36] H. Guckel, J. Klein, T. Christenson, K. Skrobis, M. Laudon, and E. G. Lovell, "Thermo-magnetic Metal Flexure Actuators", IEEE 0-7803-0456-X, 1992.

[37] N. Mankame and G. K. Ananthasuresh, "The Effect of Thermal Boundary Conditions and Scaling on Electro-Thermal-Compliant Micro Devices", MEMS 2000 Technical Proceedings of the 2000 International Conference on Modeling and Simulations of Microsystems, ISBN: 0-9666135-7-0, CD.

[38] J. H. Comtois, M. A. Michalicek, and C. C. Barron, "Electrothermal Actuators Fabricated in Four-level Planarized Surface Micromachined Polycrystalline Silicon", Sensor and Actuators: A 70 pp. 23-31,1998.

[39] H. D. Wu, K. F. Harsh, R. S. Irwin, W. Zhang, A. R. Mickelson, and Y.C. Lee, "MEMS Designed for Tunable Capacitors", IEEE 0-7803-04471-5,1998.

[40] M. Last and K. Pister, "2-DOF Actuated Micromirror Designed for Large DC Deflection", MOEM'99, Mainz, Germany, August 1999.

[41] L. A. Field, D. L. Burriesci, P. R. Robrish, and R. C. Ruby, "Micromachined 1X2 Optical-fiber Switch", Sensor and Actuators: A 53 pp. 311-315, 1996.

[42] Z. Feng, W. Zhang, B. Su, K. F. Harsh, K. C. Gupta, V. Bright, and Y. C. Lee, "Design and Modeling of RF MEMS Tunable Capacitors Using Electro-thermal Actuators", IEEE 0-7803-5135-5,1999.

[43] C. H. Mastrangelo, J. His-Jen Yeh, and R. S. Muller, "Electrical and Optical Characteristics of Vacuum-Sealed Polysilicon Microlamps", IEEE 0018-9383, 1992.

[44] CMC-Accelerating Canadian Competitiveness through Microsystems: Strategic Plan 2005-2010, Executive Summary. -http://www.cmc.ca